Improving the Prediction of Soot Emissions and Contrail Formation from Modern Turbofans Using Alternative Fuels

Mafalda Machado Martins de Nunes Narciso

Thesis to obtain the Master of Science Degree in

Aerospace Engineering

Supervisor: Prof. João Manuel Melo de Sousa

Examination Committee

Chairperson: Prof. Filipe Szonolky Ramos Pinto Cunha
Supervisor: Prof. João Manuel Melo de Sousa
Member of the Committee: Prof. Fernando José Parracho Lau

July 2021

Abstract

Condensation trails and contrail cirrus are currently responsible for the largest contribution to radiative forcing in the aviation sector, yet they have lifetimes of only a few hours. Their much shorter lifetimes when compared to long-lived greenhouse gases makes them ideal for the implementation of short-term mitigation measures. The use of Sustainable Aviation Fuel (SAF) instead of regular jet fuel has been associated to a reduction in soot particle emissions, leading to a decrease in initial ice crystal numbers in contrails, but also to a possible increase in contrail frequency and contrail ice mass due to higher water vapor emissions. A computational model was used to explore the influence of the variations of soot and water vapor emissions when using SAF and SAF blends in the formation of contrails, their ensuing optical depth, and their lifespan. An increase in frequency of contrails was found in cases where regular jet fuel emissions were close to threshold conditions. Reductions in contrail lifetime of up to 76% were found for contrails with lifetimes of over 30 minutes, while decreases in optical depth of up to 37% were found for contrails formed in air with a relative humidity of 42% or more. This work provides a better understanding of the potential of SAF as a mitigation measure against the impact of contrails on global warming.

Keywords: contrail, contrail cirrus, sustainable aviation fuel, soot, particle emissions, radiative forcing

Resumo

Os rastos de condensação, ou *contrails*, e as nuvens cirrus criadas por *contrails* são responsáveis pela maior contribuição para o forçamento radiativo do sector da aviação na actualidade, apesar do seu tempo de vida ser de apenas algumas horas. Por causa da sua curta duração comparativamente à dos gases com efeito de estufa, são ideais para a implementação de estratégias de mitigação a curto prazo. O uso de combustíveis alternativos em vez de combustíveis convencionais tem sido associado a uma diminuição na emissão de partículas, o que leva a uma diminuição no número inicial de cristais de gelo de *contrails*. Está no entanto também associado a um possível aumento na frequência de formação de *contrails* tal como na massa de gelo inicial dos *contrails* devido às suas emissões de vapor de água mais elevadas. Um modelo computacional é usado para explorar a influência do uso de combustíveis renováveis na formação, profundidade óptica e tempo de vida de *contrails*. Um aumento na frequência de formação foi encontrado em locais onde o combustível convencional estava muito perto das condições fronteira de formação de rastos de condensação. Diminuições no tempo de vida de *contrails* até 76% foram encontradas para *contrails* com mais de 30 minutos de tempo de vida, enquanto diminuições em profundidade óptica até 37% foram encontradas para *contrails* formados em locais com uma humidade relativa de 42% ou mais. Este trabalho contribui para um maior entendimento do potencial de combustíveis alternativos para mitigar o impacto de *contrails* no aquecimento global.

Palavras-Chave: rastos de condensação, nuvens cirrus, combustíveis renováveis, fuligem, emissões de partículas, forçamento radiativo

Contents

List of Tables **xi**

List of Figures **xiii**

Acronyms **xvii**

1 Introduction **7**
- 1.1 Brief Introduction to Contrails and Contrail Cirrus Clouds . . . 7
  - 1.1.1 Climate Impact and Mitigation Measures . . . 10
- 1.2 Brief introduction to Soot . . . 13
  - 1.2.1 Soot formation . . . 14
- 1.3 Sustainable Aviation Fuels . . . 15
- 1.4 Thesis outline . . . 18

2 Contrail Model **19**
- 2.1 Contrail Formation - Schmidt-Appleman Criterion . . . 19
- 2.2 Young Contrails - Wake Vortex Downwash . . . 22
  - 2.2.1 Contrail Dimensions . . . 23
  - 2.2.2 Contrail Ice Properties . . . 25
- 2.3 Contrail Cirrus . . . 27
  - 2.3.1 Trajectory . . . 28
  - 2.3.2 Contrail Dimensions and Optical Depth . . . 28
  - 2.3.3 Ice Mass and Particle Number . . . 31

3 Soot Model **35**
  - 3.0.1 Leung *et al.* Model . . . 35
  - 3.0.2 Rizk and Mongia and GSP Models . . . 39

4 Aircraft and Environment **43**
- 4.1 Gas Model and Thermodynamic Relations . . . 43
  - 4.1.1 Evaporation Model . . . 44
- 4.2 Aircraft and Engine . . . 45
  - 4.2.1 Design Point Model . . . 46
  - 4.2.2 Off-Design Model . . . 48
  - 4.2.3 Combustion Chamber Dimensions . . . 50
- 4.3 Ambient Data . . . 51

5 Results **53**
5.1 Formation Frequency 55
5.2 Lifetime 57
5.3 Optical Depth and Radiative Forcing 60

6 Conclusions and Future Work **65**
6.1 Conclusions 65
6.2 Future Work 66

Bibliography **67**

A Fuel Properties **73**

B Coefficients for Specific Heat Equation **75**

C Routes **77**

D Properties of blends **79**

List of Tables

1.1 Certified SAF production pathways. 18

1.2 SAF used in this study and their respective production pathways, feedstock and maximum blend ratios. 18

2.1 Comparison of predicted and measured values for an aircraft with $M_a = 47000$ kg, $s_a = 34.1$ m, flying at $TAS = 224$ m/s at an altitude of 320 hft. 25

3.1 Reaction Rates for the Leung *et al.* model. 35

3.2 Measured relative differences in particle emissions from flight-tests and relative differences predicted with the Rizk and Mongia Model and the GSP Model. 42

3.3 Predicted relative differences in particle number emissions for different HEFA C. Hydrogen percentages. 42

4.1 Pressure ratios and polytropic efficiencies of the LPC, fan and HPC. 46

4.2 Iteration variables for the off-design engine model. 48

4.3 Feedback errors for the off-design model iteration. 50

4.4 Optimal pressure loss and ratio of line to case cross-sectional area for an annular combustion chamber. 50

5.1 Routes analysed in this work. 53

A.1 Fuel Properties. 73

B.1 Dry air component mass fractions. 75

B.2 Coefficients for the calculation of the specific heat of hot gas. 76

List of Figures

1.1 Saturation vapour pressure in relation to supercooled liquid water (dotted line) and ice (solid line). 9

1.2 Ice nucleation thresholds and states of water droplets and ice particles in an ice saturation ratio to temperature plot. In the grey area the environment is supersaturated with respect to ice, and in the red range pure water droplets nucleate ice spontaneously. 10

1.3 Global coverage by contrails up to five hours of age and by contrail cirrus. 10

1.4 Radiative forcing contribution by the aviator sector from different components. Error bars represent 90 % likelihood range for each estimate. 11

1.5 Ice particle concentrations at a plume age of 1 s for different ambient temperatures as a function of the soot emission index, EI_N. Ice particles formed from freezing of the liquid plume and ambient water are represented by dot-dashed lines, and mixed ice particles containing soot are represented by dashed lines. The total ice particle concentration is represented by solid lines. 14

1.6 Schematic diagram of the main stages involved in soot formation, and the species produced at each stage. The relative scale of the image changes between stages, with the structures presented ranging from $<$1 nm for the soot precursors to $\sim$100 nm for the mature soot. 14

1.7 5 year prediction of European air traffic growth compared to 2019 mean air trafic. Predictions are presented for the cases where the vaccine is made available to travellers (or the pandemic ends) by the summer of 2021, where the vaccine is made available to travellers (or the pandemic ends) by the summer of 2022, and where the vaccine is not effective resulting in lingering infection and low passenger confidence. 16

1.8 Predictions of CO_2 emissions until 2050 with the current trend compared to the needed reductions to achieve the 2050 carbon emissions goal and to the 1990 efficiency trend. . 16

2.1 Saturation curves over liquid water (full) and over ice (dashed), and mixing lines in a diagram of partial water pressure versus temperature. The mixing lines are plotted for environmental conditions, with T_E at point E being the ambient temperature, and with T_C at point C being the threshold temperature for liquid saturation. 21

2.2 Threshold temperatures computed for 0 %, 40 %, 60 % and 100 % relative humidity with engine and fuel parameters $\eta = 0.3$, $EI_{H_2O} = 1.223$ and $Q = 43$ MJ/kg. Comparison is done with adapted plot from reference. 22

2.3 Schematic of contrail dynamics with altitude and contrail age with plume depth D, plume width B, and normal shear velocity S. Stage 0 represents the contrail at the time of formation, stage 1 represents the contrail after sinking due to the wake vortex downwash, and stage 2 represents the cross-section of an aged contrail. 23

2.4 Depth and width at point 1 computed for BAe 146 ($M_a = 38.1$ Mg) and example large, medium and small aircrafts with parameters obtained from reference, juxtaposed over plot where each point represents an aircraft flying over the North Atlantic during 6-9 June 2006. 25
2.5 Plots of combustion induced temperature increase in relation to time and the typical contrail cirrus IWC in relation to ambient temperature. 26
2.6 Variation with temperature of the measured mean maximum dimension for each bullet component in a bullet rosette. 32

3.1 Schematic of the simplified chemical reacting systems used in conjunction with the Leung *et al.* model. 36
3.2 Analysis of soot samples from the exhaust of a J-85 turbojet burning Jet A fuel, a 30 % Camelina blend and a 70 % Camelina blend. 40
3.3 Comparison between predicted and measured soot numbers based on data for the Lycoming ALF 502 engine. 41

4.1 Schematics of a two-spool turbofan with station numbers. 45

5.1 Geographical plot of the contrails emitted for a route over Northern and Central Europe. Contrails are plotted for their entire lifetime. Colours represent the logarithm of the optical depth at the contrail trajectory points. 54
5.2 Box plot marker. 54
5.3 Relative differences in water vapour emissions and neat heat of combustion for pure SAF. 55
5.4 Relative differences in water vapour emissions and neat heat of combustion for SAF blends. 55
5.5 Relative differences in propulsive efficiency for SAF and SAF blends. 56
5.6 Absolute differences in threshold temperature for SAF and SAF blends. 57
5.7 Relative differences in particle number emissions. 57
5.8 Relative differences in lifetime for reference contrails aged 30 minutes or less. 58
5.9 Relative differences in lifetime for reference contrails with lifetimes ranging from 30 minutes to 2 hours. 59
5.10 Relative differences in lifetime for reference contrails with lifetimes of over 2 hours. 59
5.11 Relative differences in peak optical depths and initial ice mass ratios for ambient relative humidities at formation of 43 % or higher. 60
5.12 Relative differences in peak optical depths and initial ice mass ratios for ambient relative humidities at formation in the range of 41 % to 43 %. 61
5.13 Relative differences in peak optical depths and initial ice mass ratios for ambient relative humidities at formation in the range of 40 % to 41 %. 62
5.14 Relative differences in the product of contrail width by contrail optical depth for ambient relative humidities at formation of 43 % to 58 %. 63
5.15 Relative differences in the product of contrail width by contrail optical depth for ambient relative humidities at formation of 58 % or higher. 63
5.16 Relative differences in the product of contrail width by contrail optical depth for ambient relative humidities at formation of 40 % to 43 %. 64

C.1 Routes used in contrail simulations. 77

Acronyms

AIC Aviation-induced Cloudiness. 11

ATJ Alcohol-to-Jet. 17, 18

BPR Bypass Ratio. 46

CH Catalytic Hydrothermolysis. 17, 18

CHJ Catalytic Hydrothermolysis Jet fuel. 55–58, 61

CTL Coal-to-Liquid. 18, 56, 58

ECMWF European Centre for Medium-Range Weather Forecasts. 51

EDR Eddy Dissipation Rate. 3, 23

FT Fischer Tropsch. 17, 18

FT-SKA Fischer Tropsch Containing Aromatics. 17, 18

GSP Gas turbine Simulation Program. 39–41

GTL Gas-to-Liquid. 18, 53–61, 63, 65

HEFA Hydroprocessed Fatty Acid Esters and Fatty Acids. 17, 18

HH-SPK Hydroprocessed Hydrocarbons. 17, 18

HPC High Pressure Compressor. 46, 49

HPT High Pressure Turbine. 49

ICAO International Civil Aviation Organization. 41

IQR Interquartile Range. 57, 59, 61, 62

ISA International Standard Atmosphere. 22, 26, 49, 51, 52

IST Instituto Superior Técnico. 7

IWC Ice Water Content. 26, 58

LPC Low Pressure Compressor. 46, 49

LPT Low Pressure Turbine. 49

MRD Mean Relative Difference. 54, 57–63, 65

P2P Probabilistic Two-Phase Aircraft Wake-Vortex Model. 23

PAH Polycyclic Aromatic Hydrocarbons. 15

PFR Plug-Flow Reactor. 36–38

RD Relative Difference. 41, 42, 54–65

RF Radiative Forcing. 8, 10–13, 27, 62, 63, 65

RK4 Runge-Kutta fourth-order method. 38

RWFD Real World Flightplan Database. 51

SAC Schmidt-Appleman Criterion. 19

SAE Society of Automotive Engineers. 13

SAF Sustainable Aviation Fuel. 7, 12, 13, 17, 18, 40–42, 45, 53, 55–63, 65, 66, 79

SDRD Standard Deviation of Relative Differences. 54, 57

SIP Synthesized Iso-paraffins. 17, 18, 55–61

TAS True Air Speed. 20, 47, 48, 57

WSR Well-Stirred Reactor. 36, 37

List of Symbols

Greek Symbols

β	Extinction, m^{-1}
$\beta_{LPC}, \beta_{HPC}, \beta_{LPT}, \beta_{HPT}$	Auxiliary component map coordinate
$\mathit{\Gamma}$	Circulation, m^2/s
γ	Ratio of specific heats
δ	Non-dimensional total pressure
ϵ	Eddy Dissipation Rate (EDR), J/(kg s)
η	Efficiency
θ	Non-dimensional total temperature
κ	Blend ratio
λ	Wavelength, m
λ_v	Evaporation rate, m^2/s
μ	Dynamic viscosity, Pa/s
ρ	Density, kg/m^3
ρ_γ	Normalized size parameter
σ	Covariance matrix, m^2
$\sigma_{yy}, \sigma_{zz}, \sigma_{yz}$	Coefficients of covariance matrix, m^2
τ	Optical depth
υ	Kinematic viscosity, m^2/s
ω	Vertical pressure change rate, Pa/s
ω_{oxi}	Specific surface oxidation rate, m^2/s
$\dot{\omega}$	Net production rate of species, mol/s

Roman Symbols

A	Area, m^2
A_s	Area, m^2-soot/m^3-mixture
B	Width, m
b_0	Initial vortex separation, m
c	Concentration, kg/m^3
C_0	Mass of species per plume length, kg/m
C_a	Agglomeration rate constant
C_{ex}	Thermal expansion coefficient, K^{-1}
c_p	Specific heat capacity, J/(kg K)
D	Depth, m
D_H, D_V	Horizontal and vertical diffusivity, m^2/s
e	Vapour partial pressure, Pa
EI_{H_2O}	Water emission index, kg-water/kg-fuel
EI_{soot}	Soot mass emission index, kg-soot/kg-fuel

EI_N	Particle number emission index, kg-fuel^{-1}
F	Thrust, N
f	Fuel-to-air ratio, kg-fuel/kg-air
f_{surv}	Fraction of particles surviving the wake vortex phase
G	Mixing line gradient, Pa/K
g	Gravitational acceleration, m/s^2
h	Specific enthalpy, J/kg
$H\%$	Hydrogen mass ratio, kg-hydrogen/kg-fuel
h/c	Hydrogen to carbon ratio
I	Ice mass ratio
k	Real refractive index of ice
K_W	Watson factor
k_1	Nucleation rate constant, s^{-1}
k_2	Surface growth rate constant, m$^{3/2}$-mixture/(s m-soot)
k_3	Oxidation rate constant, m^3-mixture/(s m^2-soot)
L	Contrail segment length, m
L_v	Latent heat of fuel vaporization, J/kg
M	Molar mass, kg/mol
m_i	Mass fraction of component i, kg/kg
m_{ice}	Ice mass, kg
m	Carbon number
$\dot{m}$	mass flow, m/s
Ma	Mach number
M_a	Aircraft mass, kg
N	Particle number concentration, m^{-3}
n	Number of ice particles per volume, /s
n_i	Mol fraction of component i, mol/mol
N_{bv}	Brunt-Väisälä frequency, /s
N_{dil}	Dilution factor of the contrail
N_f	Dilution factor of the plume
N_i	Total ice number concentration per contrail length, m^{-1}
N_x	Relative pool speed at component x
P	Pressure, Pa
PF	Pattern factor
p_r	Reactor perimeter, m
Q	Fuel combustion heat, J/kg
q	Absolute humidity, kg/kg
$\dot{Q}$	Rate of heat flow, W
Q_{ext}	Extinction efficiency
Q_n	Transfer number
q_{ref}	Reference dynamic pressure, Pa
R	Individual Gas Constant, J/(K mol)
r	radius, m
$Rearth$	Earth radius at the equator, m
$\dot{R}$	Reaction rate, mol/s
S	Vertical wind shear, J/(K mol)

s	Specific entropy, J/(K kg)
s_a	Wing span of aircraft, m
SG	Specific gravity
SN	Smoke number
T	Temperature, K
t	time, s
T_s	Doplet surface temperature, K
U	Eastward wind, m/s
U_{amb}	Ambient relative humidity
U_c	Threshold relative humidity
V	Northward wind, m/s
V_c	Control volume, m^3
V_P	Particle volume, m^3
V_T	Particle terminal fall velocity, m/s
v	Velocity, m/s
w_0	Initial descent speed of wake vortex, m/s
$\mathbf{X}$	Trajectory vector
x	longitude, º
$\mathbf{x}$	Vector of local orthogonal coordinates relative to the plume axis
y	latitude, º
z	altitude, m

Subscript

ad	Adiabatic
agg	Aggregation
air	Dry air
b	Boiling point
c	Threshold or critical
$comb$	Combustion or combustion chamber
$comp$	Compressor and fan
$corr$	Corrected
d	Droplet
des	Design point
dz	Dillution zone
E	Ambient air
eff	Effective
F	Fuel
f	Final or outlet
g	Gas
H	Horizontal

i	Initial or inlet
L	Liner
m	Mechanical
mix	Mixture
opt	Optimal
n	Normal
P	Plume
p	Particle
pz	Primary zone
ref	Reference
S	Shear
s	Soot or isentropic
sat	Saturation
sz	Secondary zone
t	Total or stagnation
$turb$	Turbulence or turbine
V	Vertical
x	Axial
w	Wake vortex

Chapter 1

Introduction

In 2016, a computational study [1] was carried out by a student of Instituto Superior Técnico (IST) with the purpose of evaluating the technical performance and environmental impact of sustainable fuels in aviation. The results obtained in the study showed an overall reduction in the soot mass emissions when burning Sustainable Aviation Fuel (SAF) and SAF blends when compared to medium-sulfur Jet A-1 fuel; this reduction could go up to 60 % for pure biofuel and 35 % for 50:50 blends.

A reduction in soot emissions was indeed expected due to the typically lower aromatic content in SAF when compared to conventional aviation fuels.[1] Still, at the time there was no empiric data that could corroborate the results obtained; the reduction was supported, but the order of the reduction could not be validated.

In 2017, a report [3] was published presenting the data obtained in several test-flights which used a 50:50 blend of low-sulfur Jet A fuel and a Camelina-based HEFA biojet fuel (HEFA C.). These test-flights did indeed find a significant decrease in the soot emissions. During the test-flights it was found that soot particle emissions could be up to over 50 % lower for the HEFA C. blend when compared to a Jet A fuel with medium sulfur content.

This reduction in soot emissions was connected to a marked reduction in the formation of condensation trails, despite the higher water vapour emissions when burning the blend.

This work seeks to develop a computational model based on the previous work by Ricardo Gaspar [1], focusing on the further exploration of the soot emission predictions, and extending the study to cover the formation of contrails and their characteristics for different fuels and ambient conditions.

1.1 Brief Introduction to Contrails and Contrail Cirrus Clouds

> *"'Contrails' (...) are thin, linear ice particle clouds often visible behind cruising aircraft. They form because emitted water vapor mixed with cold ambient air leads to local liquid saturation, condensation of water on aerosols, and subsequent freezing."*
>
> — Schumann, 2012 [4]

Condensation trails, or contrails, were first observed around 1914-1915, when aircraft reached the altitudes required for their formation at midlatitudes. This phenomenon received very little attention until the 1940's, when the focus on air warfare and its fast growth made the detectability of aircraft a pressing concern; several publications postulating on the causes of this phenomenon were put forward in the following years [5].

---

[1] Experiments conducted as early as 1984 found that decreases in aromatic content lead to a substantially reduction in soot emissions [2].

In 1987, the ozone hole was detected and brought to public attention, which lead to a growing concern over the potential antrophogenic effects on the global climate. Contrails were not at the forefront of the climatic worries, seeing as the emphasis at this point was put on the chemical effect of different agents on ozone, but starting in the 1990's they began to be increasingly considered due to indications of the importance of aviation-induced cloudiness's[2] impact on the climate [4].

Contrails originate from the water vapour emitted by aircraft, which condensates on nuclei[3] and subsequently freezes. For contrails to form, the ambient air must reach water saturation, while for contrails to persist the ambient air should be supersaturated with respect to ice; to understand the mechanisms associated with contrail formation and persistence, these concepts must also be understood.

To explain the concept of saturation, an example from reference [7] is considered.

A large basin is filled with water. The water molecules in the basin are in permanent motion, colliding with each other, and sometimes one of these molecules will gain enough energy to leave the basin, entering the water vapour space above it. In much the same way, the molecules in the water vapour space are in permanent motion, and sometimes one of them will enter the liquid below. This creates a permanent exchange between the liquid in the basin and the vapour above it.

The concentration of water molecules in the basin suffers only a slight variation with temperature and pressure, but the concentration of water molecules in the vapour space can vary widely, with the water molecule flux from the vapour space to the liquid varying with it. The water vapour is said to be saturated when the fluxes from liquid to vapour and vapour to liquid are in dynamic equilibrium, that is, when they are equal to each other, leading to a constant water mass in the basin.

The same can be applied to ice instead of liquid water, but the bonds between molecules in ice are much stronger which leads to a lower flux out of the ice into the vapour space. This flux can thus be matched by a lower concentration of water molecules in the water vapour, being the saturation in respect to ice achieved with a lower concentration of water molecules than the saturation in respect to liquid water.

With this, there are two scales for relative humidity, one in respect to liquid water and another in respect to ice. At temperatures above the ice melting point, only the liquid water scale can be used, but at subzero temperatures, where supercooled liquid water can exist down to around -40 °C, both scales can be applied simultaneously.

Supersaturation refers to a state where the relative humidity with respect to water or ice is higher than 100 %, that is, when saturation is exceeded. This state is considered to be metastable[4].

On figure 1.1, which represents the variation of the saturation point with temperature, it can be seen that from 0 °C to −80 °C, the saturation vapour pressure decreases by a factor of more than 10000. It can also be seen that water saturation always implies ice supersaturation [7].

With these concepts established, the formation and lifecycle of cirrus clouds and contrail cirrus can be better understood.

Cirrus clouds are ice clouds found in the upper troposphere in areas where the temperature is below approximately −40 °C; above this temperature mixed-phase clouds, clouds with both liquid water droplets and ice crystals, are typically found. Cirrus clouds reflect shortwave solar radiation and trap long-wave thermal radiation, having a large effect on the global Radiative Forcing (RF), that is, strongly impacting the energy flux in the atmosphere, due to their persistence at high altitudes if the temperature is low enough. On average, their effect is to heat the Earth's atmosphere.

---

[2] "Aviation-induced cloudiness consist of contrails cirrus (...) and of changes in the occurrence or properties of natural cirrus arising from both the presence of contrail cirrus and increased ice-nuclei concentrations in the the upper-troposphere due to aircraft soot emissions." - (Burkhard, 2011) [6]

[3] The condensation nuclei may be preexisting in the atmosphere or may be formed in the exhaust of the engine.

[4] For an unstable state, processes start to immediately drive it towards equilibrium. A metastable state differs from it in that it can last for a long time.

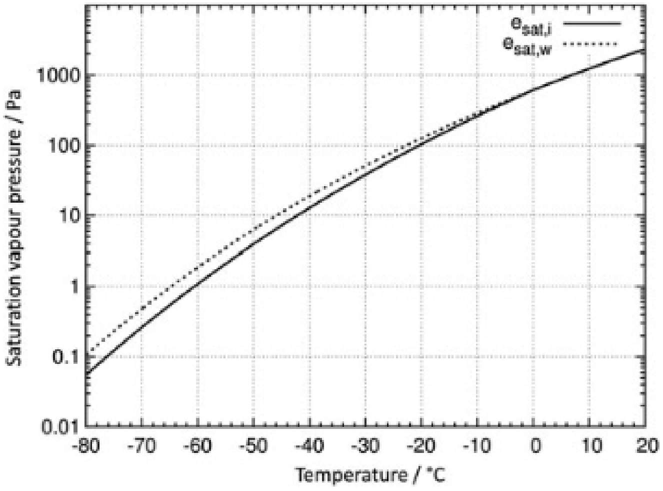

Figure 1.1: Saturation vapour pressure in relation to supercooled liquid water (dotted line) and ice (solid line) [7].

Cirrus clouds require a relative humidity over ice of over 145 %, classified as high ice supersaturation, to form, and ice saturation to persist. The reason behind this disparity is that newly formed ice crystals are not in equilibrium with the ice supersaturated air around them. Cirrus clouds are set apart from other clouds in both formation and persistence requirements, seeing as other clouds form and evaporate at temperatures slightly above and below liquid water saturation [7][8].

Figure 1.2 represents the relevant thresholds and state information for the formation and persistence of contrails. The red range represents the temperature at which supercooled liquid water droplets spontaneously nucleate to ice; below this temperature pure ice cirrus clouds begin to form. The homogeneous freezing threshold is the temperature and ice saturation ratio at which ice nucleates in liquid aerosol particles, and below this threshold is the range at which cirrus clouds can be maintained, but not formed *in situ*.[5]

Contrary to cirrus clouds, contrail cirrus only require the environment to be at ice saturation. During a flight, the aircraft engine releases both water vapour and heat; the former promotes water saturation while the latter hinders it. The heat release leads to an increase in temperature which in turn leads to an increase in the vapour concentration required for saturation, as seen in figure 1.1. For contrails to form, the water vapour concentration increase due the emitted water vapour has to be greater than the increase in local plume liquid water saturation point due to the emitted heat. These plume conditions can be achieved without the high ice supersaturation environment required for cirrus cloud formation, requiring only an environment at ice saturation.

When mixed with sufficiently dry ambient air, contrails evaporate soon after their formation and are classified as short-lived contrails. Yet, their conditions for evaporation are the same as those for cirrus clouds, meaning that in an ice supersaturated environment, well below the homogeneous freezing threshold in figure 1.2, they can be formed and persist until either the relative humidity drops below ice saturation or they sediment into drier air [5].

This means that in a substantial fraction of the upper troposphere, contrail cirrus can form and persist in air that is cloud free, increasing the high cloud coverage in environments where cirrus clouds would not be able to form. Contrails which did not disappear during early mixing are labelled persistent contrails. These can maintain their characteristic linear shape for a few hours before evaporating or sedimenting.

---

[5] Anvil cirrus can still be formed through high reaching convention rapidly transporting water into the upper trophosphere. Within the convective system water droplets form and can then freeze either spontaneously or at higher temperatures if they come in contact with ice crystals or heterogeneous ice nuclei [8].

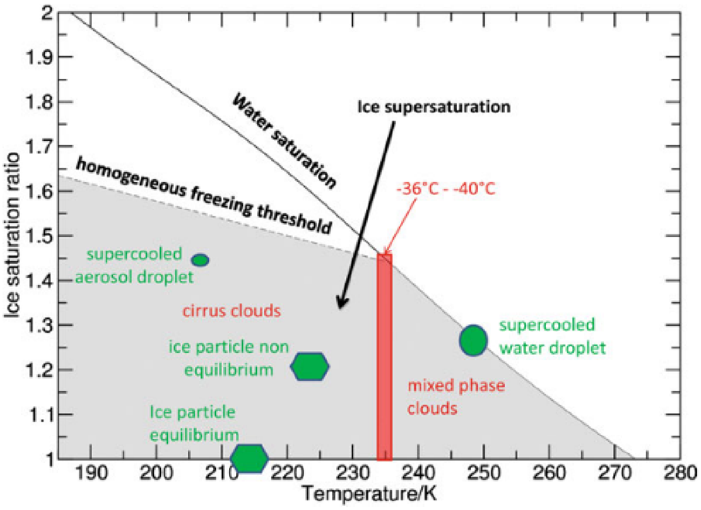

Figure 1.2: Ice nucleation thresholds and states of water droplets and ice particles in an ice saturation ratio to temperature plot. In the grey area the environment is supersaturated with respect to ice, and in the red range pure water droplets nucleate ice spontaneously [8].

If this does not happen they instead form into long-lasting contrail cirrus, losing their linear shape and becoming indistinguishable from cirrus clouds. Simulations of the contrail coverage for the year 2020 showed a coverage by contrail cirrus approximately nine times larger than the coverage by persistent contrails with than five hours of age; over central Europe the contrail cirrus coverage was the largest, reaching up to 10 %, while over Portugal it reached up to 4 %, as seen in figure 1.3 [6].

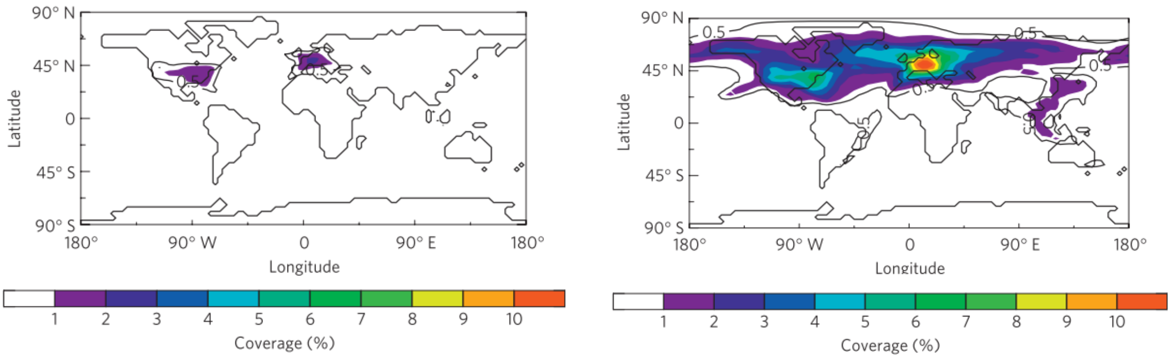

(a) Persistent contrails up to five hours of age.

(b) Contrail cirrus.

Figure 1.3: Global coverage by contrails up to five hours of age and by contrail cirrus [6].

1.1.1 Climate Impact and Mitigation Measures

In 2017, the aviaton sector contributed approximately 5 % of the global anthropogenic RF, with the RF attributed to contrails and contrail cirrus being estimated as 50 mWm^{-2}, making it the largest contribution in the sector [3]. Yet, contrail cirrus have a much shorter lifetime than long-lived greenhouse gases; this influences their relative importance when it comes to estimating the long-term climatic impact of the aviation sector [6], and also makes them very suitable for mitigation efforts since the effects would become very quickly apparent [9].

Figure 1.4 shows the estimated contributions to RF from different components; in this figure it can be seen that large uncertainties (the largest in the aviation sector) are associated with the effects of

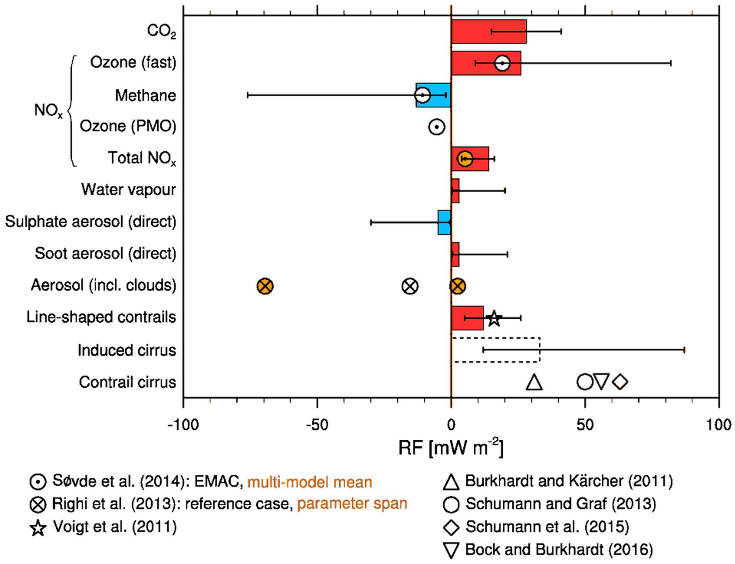

Figure 1.4: RF contribution by the aviator sector from different components. Error bars represent 90 % likelihood range for each estimate [10].

Aviation-induced Cloudiness (AIC). AIC refers to the increase of cloudiness due to the effects of aviation, be it directly through the formation of contrails and contrail cirrus, or indirectly through the emission of black carbon, organic and sulfate aerosols that could act as cloud condensation nuclei. In figure 1.4, which shows the estimated contributions to the aviation sector RF from different components, it can be seen that the largest uncertainties are associated with AIC [3][10].

The uncertainties relating to the current effects of AIC on the climate carry on to the predictions of their future effect. It is nevertheless generally agreed that the RF of contrail cirrus will increase in the coming years. This increase was estimated to be by a factor of 3 from 2006 to 2050, reaching 160 or even 180 mWm^{-2} by that year. This estimate attributed this in part to both a large increase in air traffic, and a slight shift in the air traffic towards high altitudes [9][11].[6] There was indeed a continuous increase in commercial air traffic up to the year 2019, but a steep decrease in 2020 ended this trend [12]. It has yet to be seen how much it will impact past predictions, but, as of now, central traffic forecasts used for 2050 predictions have decreased 16 % compared to 2019 forecasts [13].

The propulsion efficiency of an aircraft is a measure of how well the energy available in the fuel is converted into useful forward motion of the aircraft; it can be expressed as the product of the individual efficiencies in the process. The two main efficiencies used to describe the engine are its thermal efficiency, a measure of the effectiveness with which the available chemical energy is turned into mechanical energy, and the propulsive efficiency, a measure of how well that mechanical energy is turned into thrust.

Higher values of these efficiencies result in a reduced fuel consumption and lower CO$_2$ emissions. Their relation to NO$_x$ emissions is more complex - lower fuel consumption implies lower NO$_x$ emissions, while a higher thermal efficiency may lead to higher NO$_x$ emissions per unit mass of fuel, which requires a more careful balance [14]. Contrasting these, the influence of a higher propulsion efficiency on the formation of contrails is not as complex or beneficial - a higher propulsion efficiency directly correlates with increased contrail formation [15].

The overall propulsion efficiency can also be said to represent how much of the energy generated by the engine goes towards propulsion and how much escapes as heat. The higher it is, the lower the heat released to the air is; seeing as this heat goes against contrail formation, the higher the overall propulsion efficiency, the easier it is to have contrails form at higher temperatures, that is, at lower altitudes in the troposphere and higher altitudes in the stratosphere. The evolution of engines over the years and their increasing efficiency has thus facilitated the formation of contrails and is expected to continue doing so [5][15].

---

[6] This shift towards higher altitudes has an attenuating effect in the contrail cirrus RF in midlatitudes, but a reinforcing effect in tropical areas [9].

An increase of 30 % to 50 % in the overall propulsion efficiency would lead to an increase in the contrail formation threshold temperature of contrails of 4.2 to 4.9 K in the troposphere, and of 14 K in the stratosphere - which would cause a decrease in the threshold altitude of 650 m to 760 m in the troposphere, and an increase of as much as 2139 m in the stratosphere, - broadening in a significant way the altitude range at which contrails form [15]. For contextualization, as of 2019 the overall propulsion efficiency of aircraft is expected to grow by 2 % per year until the year 2050, due to weight reductions, more fuel efficient engines, aerodynamic changes and an increased operational efficiency [9].

A reduction in the soot emissions is also expected, with a predicted reduction by 50 % leading to a decrease in RF by contrail cirrus of approximately 15 %, thanks both to reduction in their coverage and optical depth.[7] This projected decrease would still not be able to overcome the strong increase in contrail cirrus RF due to the projected increase in air traffic [9].

Since the predicted technological evolution of aircraft is expected to increase the future formation of contrails instead of reducing it, mitigation measures should be explored.

Research has demonstrated that one possible measure is changing flight paths, either laterally or vertically, to avoid contrail the ice-saturated and low temperature regions where contrails typically form [16][17].

This strategy could potentially go one step further. Contrails have far greater regional effects than those expected from global mean values, which could potentially aid mitigation efforts by avoiding flights in regions where contrails warm the Earth and increasing them in regions where contrails cool it [8].

Aircraft routes are typically designed to reduce flight time and cost, and a major drawback from this strategy would be the penalties suffered in this [16]. Additionally, while some estimates place the contribution of contrail cirrus to the aviation sector RF far above all other contributions, other estimates place it only slightly above CO_2 emissions. In this case, the increased CO_2 emissions could overtake any benefits gained through the decrease in contrail emissions [6].

The potential impact of changes in flight scheduling on contrail cirrus RF has also been investigated. During the day, cooling due to the short wave cloud albedo effect tends to somewhat compensate the long wave warming effect of contrails. The warming effect of contrail cirrus is thus significantly larger during the night; by shifting flights to daytime only, the RF of contrail cirrus could potentially be reduced. Yet, simulations showed no significant changes caused by this shift [18].

There have been a number of engine and aircraft designs theorized to affect the formation of contrail cirrus. These typically have the goal of either reducing the overall efficiency of the aircraft or altering wake vortex properties. An example of the former is the use of distributed propulsion in the form of minigas turbines or remotely driven fans, while an example of the latter is the increase of the distance between wing tip vortices and the aircraft exhaust, which could be achieved with fuselage mounted engines [19].

The design strategies are numerous, but they mostly have one thing in common: the need to overhaul current aircraft in lieu of the more climate-friendly designs. While further research could reveal these to be good long-term solutions, interim solutions would still be needed.

Finally, a reduction in soot particle emissions has been considered as a possible contrail cirrus mitigation measure. As was previously stated, flight-tests that burnt a SAF blend with lower aromatics content than conventional aviation fuel saw an effect on contrails which was attributed to a reduction in particle emissions [3].

---

[7] Maximum values for RF are found in areas where the contrail cirrus coverage is maximum, and it is higher in areas where the contrail cirrus optical depth is large [6].

This work seeks to further investigate the influence of SAF on contrail formation and contrail cirrus properties, taking into account the effect of the differences in soot emissions, water vapour emissions, and other combustion and exhaust properties.

1.2 Brief introduction to Soot

Particle emissions by aircraft were noticed very early in the history of aviation, first associated with the eye-catching black exhaust that came out of their engines. As early as 1970, the smoke number measurement was created and documented in the Society of Automotive Engineers (SAE) International Aerospace Recommended Practice guidelines, and its original goal was to ensure compliance with an exhaust visibility criterion. This was quite successful in greatly reducing the emission of the larger particles which constituted the black smoke, but it did not address the smaller particles that would only later became a subject of concern [20]. New standards have since been adopted to regulate the ultrafine soot particles that were previously not addressed [21].

Soot is a solid substance consisting mostly of carbon with up to 10 % in hydrogen molar content and a density of around 1.85 g/cm^3. The basic units of soot are spherical or nearly spherical particles with diameters in the range of 20 - 30 nm, corresponding to around one million carbon atoms per particle, which are typically found in the form of necklace-like agglomerates [22][23].

On a local level, these non-volatile particle emissions have been shown to negatively impact air quality near airports and to cause significant health problems associated with the respiratory system [24]. On a global level, they are responsible for both directly and indirectly affecting the net RF of the planet.

The small black particles trap infrared radiation when emitted, causing positive RF. This direct RF is rather small when compared to the effect of other aircraft emissions. To the contrary, their indirect effect, associated to the formation of contrail cirrus, while not yet fully quantified is thought to be rather large [25].

This study focuses on the indirect impact of soot through their contribution to contrail cirrus RF. Figure 1.5 shows, for different ambient temperatures, simulated data of the contribution of soot particles to the early contrail ice particle formation. In the figures, the formation of ice particles by the freezing of pure liquid plume or ambient water is represented by a dot-dashed line, while the formation of ice particles by the homogeneous freezing of water around soot nuclei is represented by a dashed line [26].

Figure 1.5a corresponds to threshold conditions, while the other remaining figures correspond to colder temperatures. From the figures, it is clear that a drop in temperature corresponds to a significant increase in ice particle concentration as well as a greater contribution from the frozen pure liquid water.

Still, in a soot rich regime, with a soot emission index of $EI_N \geq 10^{14}$ (kg-fuel)$^{-1}$, the contribution of the frozen liquid particles becomes negligible when compared to that of the mixed soot-nuclei ice particles, with the total ice particle concentration closely following the mixed ice particle concentration line. Aircraft have a typical soot emission index in the order of $10^{14} - 10^{15}$ (kg-fuel)$^{-1}$, meaning that reductions of up to one order of magnitude in soot emissions lead to approximately the same reduction in the number of ice particles; hence, the influence of soot emissions in the formation of contrails can not be neglected [26][27].

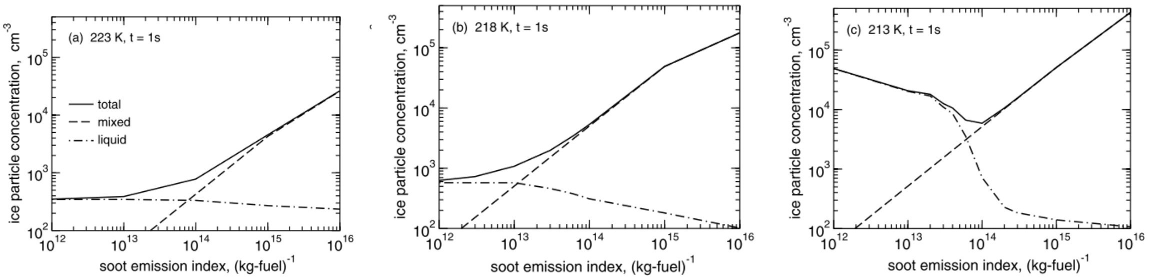

(a) T_{amb} = 223K.

(b) T_{amb} = 218K.

(c) T_{amb} = 213K.

Figure 1.5: Ice particle concentrations at a plume age of 1 s for different ambient temperatures as a function of the soot emission index, EI_N. Ice particles formed from freezing of the liquid plume and ambient water are represented by dot-dashed lines, and mixed ice particles containing soot are represented by dashed lines. The total ice particle concentration is represented by solid lines [26].

1.2.1 Soot formation

The complex chemistry and physics of soot formation has made it a heavily studied phenomenon, giving rise to a variety of models to both explain it and predict it. The computational models created with this goal have had a wide complexity range, from semi empirical correlations, to semi-empirical models, to attempts to fully describe the detailed elementary chemical reactions and physics of soot formation [28].

In this section, the currently known chemical and physical processes involved in the formation of soot are described.

Soot is the result of the incomplete combustion of hydrocarbon-based fuels. Their formation involves the transformation, through both chemical and physical phenomenons, of gas-phase hydrocarbon molecules into carbonized aggregates of quasi-spherical particles, as seen in figure 1.6. Due to the complexity involved in this process, it is customarily described as a set of simplified stages. Except for the initial transition from gas-phase to condensed-phase, there is not a sharp transition between these stages and they tend to be somewhat arbitrarily defined [22][29].

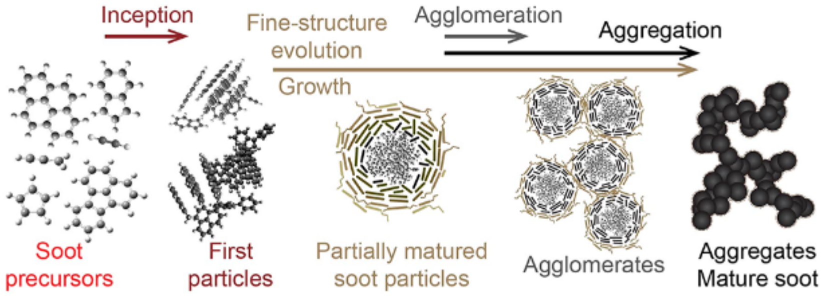

Figure 1.6: Schematic diagram of the main stages involved in soot formation, and the species produced at each stage. The relative scale of the image changes between stages, with the structures presented ranging from <1 nm for the soot precursors to ∼100 nm for the mature soot [29].

The first step in the formation of soot particles involves the formation of the soot precursor species. Soot precursor species are gas-phase hydrocarbon molecules that serve as molecular building blocks for soot particles; these species have not been definitely identified, and it is likely that that are many different soot precursors with roles that depend on local combustion conditions. Prediction models tend to use surrogates due to the lack of knowledge of the real species involved, their kinetics, and variations brought on by the use of different fuels or combustion conditions. While early models assumed the soot precursors to be small hydrocarbons such as acetylene or benzene, nowadays there are several groups considered to be potential soot precursors, such as unsubstituted Polycyclic Aromatic Hydrocarbons (PAH), aliphatically bridged or substituted PAH, ions, radicals and oxygenated hydrocarbons; the connection to PAH in particular is well established, and connected to the reductions in soot found when using fuels with low aromatics content [29][30].

The gas-phase molecules, that is, the soot precursors, transition to condensed-phase species in a process termed 'particle inception'. The incipient particles are liquid-like and possess limited absorption in the visible spectrum, vastly different from the mature, solidified soot particles. The details of the inception process are rather poorly understood, but it is known that during this process the particles experience rapid growth due to coagulation and gas-to-particle conversion. These particles also lose hydrogen through a high temperature carbonization process, progressing from a C/H ratio as low as 1 for a newly formed particle to a C/H in the range of $\sim$8 to $\sim$20 for mature soot particles. Throughout the carbonization process, the density of the particles increases and their optical properties evolve, making them able to absorb and emit light in the visible and near-infrared regions of the light spectrum [22][29].

The primary soot particles, that is, the quasi-spherical particles that function as the building blocks of the soot aggregates, grow through the deposition, condensation, chemical adsorption and physical adsorption of gas-phase molecular species to or on their surface. The processes that result in the addition of mass to the particle through surface interactions are usually referred to as 'surface growth'. Experimental results suggest that acetylene is likely to drive these processes for atmospheric and lower pressures, but hydrogen atoms, as well as aromatics, radicals and acetylenic species may also contribute to the process.

As the particles continue to evolve, they collide with each other while retaining their original shape, and form loosely bound agglomerates, held together by electrostatic forces. The growth of layers of graphene on the surface of particle agglomerates strengthens their bonds and creates difficult to separate particle aggregates; these aggregates are the mature form of soot particles.

As the processes described occur, soot mass is partially reduced due to the process of oxidation. In this process molecules of O_3, O_2, O and HO interact with the surface of the solid-phase particle to form gas-phase CO, CO_2 and H_2O.

There are other processes thought to intervene in the formation of soot, and this description is in no way exhaustive, but it encompasses the most agreed upon path and the mechanics typically used to model the process with good accuracy.

It is important to note that despite the division by stages, these processes occur simultaneously throughout the gas turbine. Due to this, engine emissions do not contain solely fully matured soot particles, but instead contain different quantities of particles in all stages of this evolution.

Mature soot particles, when released into the atmosphere, fall into the black carbon category. Black carbon particles are a subset of atmospheric carbon emissions with a strong absorption in the visible spectrum, a sublimation temperature of around 4000K, and a lack of solubility in polar and non-polar solvents. They have a graphitic fine structure and consist of aggregated quasi-spherical particles.

Young soot particles, on the other hand, are typically classified as brown carbon emissions. Brown particles display a weaker and less broad light absorption, with an enhanced absorption at short visible wavelengths which makes them appear brown instead of black. These particles tend to be soluble in some organic solvents [29].

1.3 Sustainable Aviation Fuels

At the tail end of 2019, predictions for global air traffic growth were overall positive. With a 45 % growth total growth in the decade before, and a 6.8 % growth just between 2017 and 2019, many expected the aviation industry to experience a prolonged 'golden age' with sustained growth. Yet, 2020 brought about an abrupt shift in this trend; global air traffic suffered an abrupt decline, and the recovery to 2019 levels is expected to take years [31][32].

Figure 1.7 illustrates the current predictions on the evolution of European air traffic growth based on different developments of the pandemic, with the fastest predicted recovery taking four years.

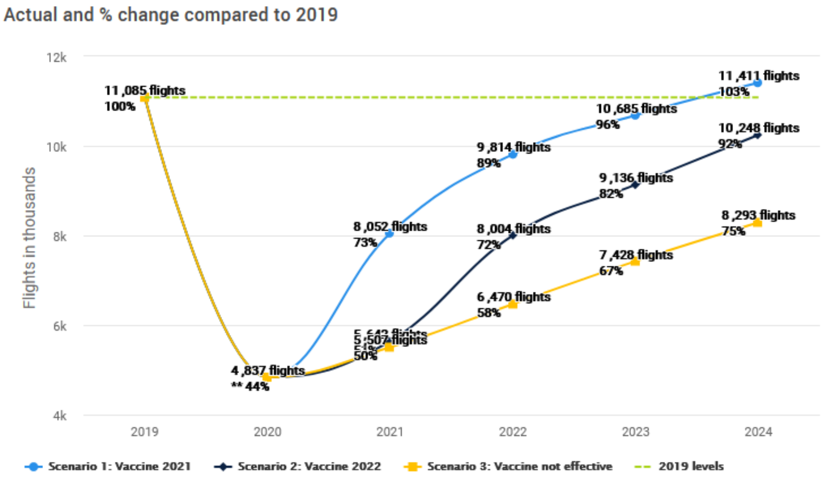

Figure 1.7: 5 year prediction of European air traffic growth compared to 2019 mean air trafic. Predictions are presented for the cases where the vaccine is made available to travellers (or the pandemic ends) by the summer of 2021, where the vaccine is made available to travellers (or the pandemic ends) by the summer of 2022, and where the vaccine is not effective resulting in lingering infection and low passenger confidence [33].

Despite the uncertainty pertaining to when the aviation sector will recover, this decline in air traffic is not considered to be everlasting or to mark an end to the aviation industry. As the sector recovers, the aircraft emissions seen in previous years will also return and continue to grow if steps to prevent it are not taken.

Predictions for the increase in contrail and contrail cirrus radiative forcing in the coming years have yet to be revised to account for the pandemic and its recovery period. In its stead, predictions for the evolution of CO_2 emissions are presented; these serve to contextualize the predicted impact of the decline in air traffic in aircraft emissions.

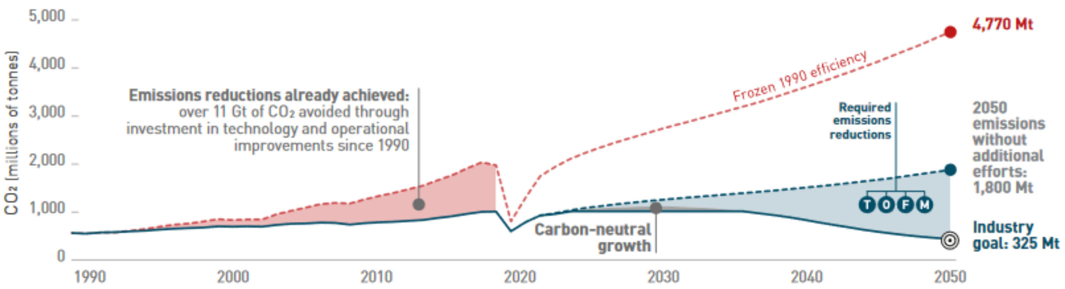

Figure 1.8: Predictions of CO_2 emissions until 2050 with the current trend compared to the needed reductions to achieve the 2050 carbon emissions goal and to the 1990 efficiency trend [13].

As can be seen in figure 1.8, while the pandemic did hinder the growth of CO_2 emissions, this is not expected to be enough to reach the current carbon-neutrality industry goal by itself. The trendline of CO_2 emissions, and not the order of magnitude, is the essential part of this figure; the influence of the air traffic decline is evident, but after the marked recovery period, the previous growth is expected to continue at the same rate as before. In the absence of other influences for this time period, it is expected that the trendline for the growth of other aircraft emissions will also follow this.

The high and seemingly ever-growing oil prices were one of the main incentives to invest in SAF and most efficient aircraft. The steep drop in oil prices in the global market in 2020 seemed to come nullify this incentive, yet oil prices seem to be recovering quickly, having already reached 2019 average levels before mid-2021, and while the future of the market remains uncertain, estimates of its near-future growth have vastly improved [34].

At this junction it is difficult to predict how the economical incentives to adopt SAF will evolve, but the often touched-upon political incentives remain. Currently petroleum fuel supplies hail largely from geopolitically sensitive areas, which makes them vulnerable to blockages and terrorist sabotage. SAF presents itself as an attractive solution to this problem since its production is not limited to locations where fossil-fuels can be drilled; due to the wide range of feedstock that can be used in its production, SAF can be produced in different environments and quantities all around the globe. Production on a national level could further lead to financial energy independence and new economic opportunities for countries with no previous stronghold in the energy market [30][35][36].

From an environmental standpoint, SAF are still an attractive compromise for the reduction of air travel emissions in the interim before carbon neutral electric or hydrogen powered flight becomes viable and able to replace current aircraft.

While carbon neutral technologies could emerge in the aircraft market as early as the next decade, regulatory and production cost concerns may still cause a significant delay. A larger hurdle to overcome is the need to adapt the aircraft design around these technologies; aircraft are high-value assets which take a long time to be built and to pay off, usually remaining in operation for 25 years or more. The typical slow fleet turnover may prove itself to be the most time-consuming obstacle to overcome, and it is one that does not affect SAF to nearly the same degree [37][38].

SAF have chemical and physical characteristics which are almost identical to those of conventional jet fuel. This allows them to use the same supply infrastructure and, when mixed with conventional jet fuel to ensure minimum aromatic content requirements, to be used in preexisting aircraft and engines.

When SAF are burnt alone, their lack of aromatic content hinders the swelling of the nitrile O-rings which are typically used by the sector; this can lead to fuel leakage, and is thus of great concern. Current regulations require a minimum of 8 % aromatic content in a fuel blend to prevent this. However, newer O-rings fabricated from fluorocarbons do not require the swelling effect of aromatics. This could eventually lift the minimum aromatic content regulations if it was proven to no longer be necessary, making the adoption of pure SAF less challenging [35][39].

Seven pathways for the production of SAF have been certified since 2009; these are the Fischer Tropsch (FT) pathway, the Fischer Tropsch Containing Aromatics (FT-SKA) pathway, the Hydroprocessed Fatty Acid Esters and Fatty Acids (HEFA) pathway, the Synthesized Iso-paraffins (SIP) pathway, the Alcohol-to-Jet (ATJ) pathway, the Catalytic Hydrothermolysis (CH) pathway and the Hydroprocessed Hydrocarbons (HH-SPK) pathway. The CH pathway and the HH-SPK pathway were the most recently approved, having been certified in 2020.

The feedstock used for each blend as well as the maximum blend ratios certified for flight are listed in table 1.1.

The fuels listed in table 1.2 will be studied in this work both as pure SAF and as a blend with the maximum certified ratio for their respective pathways. The properties of these fuels can be found in Appendix A. The blends are a mixture of the SAF with the reference fuel, Jet A-1, and their properties are computed as seen in Appendix D.

Pathway	Maximum blend (% vol)	Feedstock
FT and FT-SKA	50 %	Wastes, coal, gas, sawdust
HH-SPK	10 %	Algae
CH	50 %	Waste and energy oils
ATJ	50 %	Sugarcane, sugar beet, sawdust, lignocellulosic
SIP	10 %	Sugarcane, sugar beet
HEFA	50 %	Palm, camelina, jatropha and used cooking oil

Table 1.1: Certified SAF production pathways [35].

Fuel	Pathway	Feedstock
Gas-to-Liquid (GTL)	FT	Natural Gas
Coal-to-Liquid (CTL)	FT	Coal
HEFA R-8	HEFA	Mixed Fats
HEFA C.	HEFA	Camelina Oil
Green Diesel	HEFA	Vegetable Oil
CH	CH	Carinata Oil
ATJ	ATJ	Corn
SIP	SIP	Sugars

Table 1.2: SAF used in this study and their respective production pathways, feedstock and maximum blend ratios.

1.4 Thesis outline

Chapter 2 presents an in-depth description of the model implemented to describe the formation and lifetime simulation of contrails and contrail cirrus. Since each part of the contrail life requires vastly different approaches in its modelling, the chapter is divided between sections which contain the description of the model used and its validation.

The soot particle number is one of the main contrail model inputs which account for fuel distinction. Due to the complexity in its prediction when compared to other inputs, chapter 3 is fully dedicated to models which were investigated for this application. It includes the model chosen for this work, its validation and considerations regarding its use, as well as additional considerations.

Chapter 4 contains additional models used in the development of this work. Its first section collects important thermodynamic relations and common equations used in the treatment of gases to avoid unneeded redundancy and confusion. The following section includes a description of the engine model and considerations regarding the modelling of the aircraft. The last section discusses the model of the atmosphere used in simulations.

Chapters 5 is dedicated to the presentation of the results of this study as well as their discussion.

Chapter 6 summarises the conclusions of this work and proposes possible paths for future work.

Additional details, such as the computation of blend properties, can be found in the Appendix.

Chapter 2

Contrail Model

2.1 Contrail Formation - Schmidt-Appleman Criterion

The thermodynamic formation of contrails is explained using the Schmidt-Appleman Criterion (SAC). The theory behind this criterion was first put forward by Ernst Schmidt in 1941; he understood that the formation of contrails did not depend on engine, jet or contrail particle details. In his theory, Schmidt assumed that the ice particles in contrails formed under equilibrium conditions which, for low temperatures, would imply ice saturation in the plume. Yet, *in situ* measurements of contrails carried out shortly after he put forth this theory showed that contrail formation actually required local liquid saturation in the exhaust plume. In 1953, Appleman published a thermodynamic explanation similiar to Schmidt's identifying local liquid saturation as necessary for contrail formation.

Test flights conducted in 1994-1998 supported these two theories and also showed that contrail formation had a significant dependence on the overall propulsion efficiency of the aircraft. The Schmidt-Appleman Criterion has since been used to decide whether an atmosphere is cool and humid enough to allow for the formation of contrails.

As already stated, for contrail formation to occur, liquid saturation has to occur locally in the plume[1] of exhaust gases during mixing with the cold ambient air. This condition is satisfied when the ambient temperature is below a certain threshold temperature, T_C, or the ambient relative humidity is above a certain threshold relative humidity, U_C. This section demonstrates how to compute these [8].

The amount of water vapour in the exhaust is one of the key factors in the formation of contrails. For every unit mass of fuel, there will be EI_{H_2O} mass units of water vapour emitted. The water vapour emission index, EI_{H_2O}, can be obtained with equation 2.1, which is dependent on the molar masses of hydrogen and water, M_{H_2O} and M_H, and on the hydrogen mass ratio in the fuel, m_H [5].

$$EI_{H_2O} = \frac{m_H M_{H_2O}}{2M_H} \tag{2.1}$$

Aircraft fuels contain carbon and hydrogen, but also some sulfur and other minor constituents [5]. Still, they can generally be expressed in the form $C_m H_{2m}$ [40], which neglects these minor constituents. The hydrogen mass content for a fuel with a certain m value can be obtained using equation 2.2.

$$m_H = \frac{2mM_H}{2mM_H + mM_C} \tag{2.2}$$

The water vapour in the exhaust, EI_{H_2O}, will add to the water content in the ambient air, m_E, when the exhaust gases mix with their surrounding environment. This will result in a mass fraction of water vapour in the plume of m_P, given by,

---

[1] "The exhaust heat and the mass of exhaust gases leaving the engine are contained in the plume. The plume is a region which grows in cross-section by mixing with the ambient air, but initially coincides with the jet of high speed exhaust gases leaving the engine." - (Schumann, 2000) [15]

$$m_P = \frac{EI_{H_2O} + (N_f + 1)m_E}{N_f} \tag{2.3}$$

where N_f represents the dilution factor. N_f mass units of exhaust gases will be emitted by burning 1 mass unit of fuel with $(N_f - 1)$ mass units of air.

The heat in the exhaust gases is another key factor for the formation of contrails. When burning the fuel with air, the engine will release a combustion heat Q per unit mass of fuel. A fraction η of the combustion heat will be converted into work to propel the aircraft, while the rest, $(1 - \eta)Q$ per unit mass of fuel, will be released with the exhaust gases. This fraction η is the overall propulsion efficiency of the aircraft and can be calculated with equation 2.4, where F is the thrust, True Air Speed (TAS) is the true airspeed of the aircraft, Q is the fuel combustion heat and $\dot{m}_F$ is the fuel flow rate [5].

$$\eta = \frac{F \times TAS}{Q\dot{m}_F} \tag{2.4}$$

Much like the water vapour, the heat of the exhaust gases, $(1 - \eta)Q$, will also add to the heat in the environment air, h_E. The specific entalphy of the exhaust gases in the plume can thus be obtained from equation 2.5.

$$h_P = \frac{Q(1-\eta) + (N_f - 1)h_E}{N_f} \tag{2.5}$$

As the exhaust gases in the plume further mix with the ambient air, the N factor increases without limit; if the system containing the exhaust gases and the air mixed in the plume is under isobaric and adiabatic conditions, equations 2.3 and 2.5 will be valid for any N.

The mixing will occur between the conditions right after the engine, m_P and h_P, and the ambient air conditions, m_E and h_E.

$$\mathit{\Delta} m = m_P - m_E = \frac{EI_{H_2O} - m_E}{N_f} \tag{2.6a}$$

$$\mathit{\Delta} h = h_P - h_E = \frac{Q(1-\eta) - h_E}{N_f} \tag{2.6b}$$

Since the ambient water content and heat is small compared to the emitted water vapour and the combustion heat, equations 2.6a and 2.6b can be simplified equations by cutting these out.

$$\mathit{\Delta} m = m_P - m_E = \frac{EI_{H_2O}}{N_f} \tag{2.7a}$$

$$\mathit{\Delta} h = h_P - h_E = \frac{Q(1-\eta)}{N_f} \tag{2.7b}$$

There is interest in the representation of the mixing lines using the water vapour partial pressure of the plume, e_P, and not the water vapour mass fraction; this is due to the fact that in an $e - T$ plot the saturation pressures over liquid water, e_L, and ice, e_I, remain invariant under changes in air pressure, and therefore altitude. In this case, only the steepness of the mixing line, G, varies.

$$G = \frac{\mathit{\Delta} e}{\mathit{\Delta} T} = \frac{e_P - e_E}{T_P - T_E} \tag{2.8}$$

The partial water pressure can be related to the water vapour mass fraction through equation 2.9, where P_E is the ambient pressure, and R_{H_2O} and R_{air} are the individual gas constants of water and air.

$$e_P = \frac{R_{H_2O}}{R_{air}} P_E m_P \tag{2.9}$$

Equation 2.9 can be used along with the enthalpy relation for constant ${c_p}^2$, $\Delta h = c_p \Delta T$, to yield a new formulation for equation 2.8:

$$G = \frac{R_{H_2O}}{R_{air}} \frac{c_p EI_{H_2O} P}{Q(1-\eta)} \tag{2.10}$$

For sufficient low temperatures, and without phase change occurring, mixing follows a line with gradient G in the $e - T$ diagram, where each point corresponds to a specific value of N.

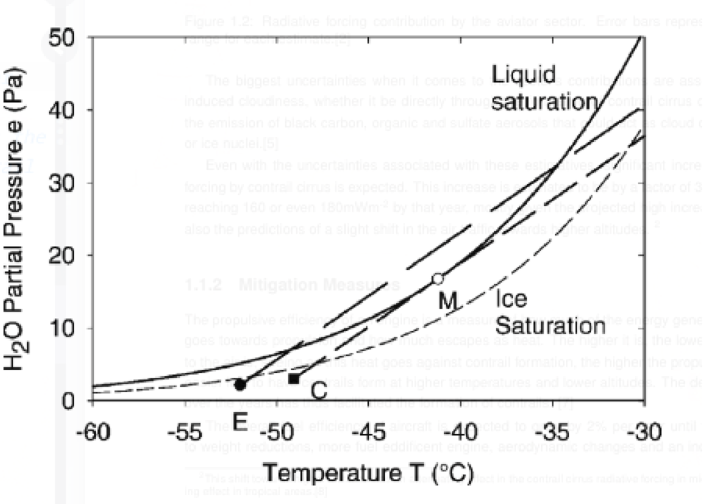

Figure 2.1: Saturation curves over liquid water (full) and over ice (dashed), and mixing lines in a diagram of partial water pressure versus temperature. The mixing lines are plotted for environmental conditions, with T_E at point E being the ambient temperature, and with T_C at point C being the threshold temperature for liquid saturation [15].

Figure 2.1 represents the saturation curves over liquid water and over ice, which, as previously stated, remain invariant in an $e - T$ diagram for different air pressures. The two mixing lines represented have the same gradient, G, with one starting at environmental conditions and the other at threshold conditions. The engine conditions are on the far right, outside of the range plotted. The threshold conditions are the conditions beyond which contrails may form; in the diagram the mixing line for the environmental conditions is beyond the threshold conditions line, therefore contrails may form.

If the ambient air is at threshold conditions, $T_E = T_C$, the two lines coincide and the mixing line merely touches the saturation curve, T_M. The value of T_M can be obtained from equation 2.11, which equates the gradient of the saturation curve to the gradient of the mixing line at the point M, where they touch.

$$\frac{de_{sat}(T_M)}{dT} = G \tag{2.11}$$

It can seen that T_M is dependant on the gradient G, hence on the fuel parameters, the propulsion efficiency and the ambient pressure.

Since the gradient G of the mixing line is constant, the threshold temperature, T_C, follows from equation 2.12, where $e_{sat}(T_C)$ is the vapour pressure in the environment under threshold conditions and U_{amb} is the ambient relative humidity over water [5].

---

[2] For dry air $c_p(T)$ varies between 1001.5J/(kgK) for $T = 200K$ and 1050 J/(kgK) for $T = 600$ K. Only for large dilution, when the plume temperature has dropped below 323 K, can a constant value, 1004 J/(kgK), be used.

$$T_C = T_M - \frac{e_{sat}(T_M) - U_{amb} e_{sat}(T_C)}{G} \tag{2.12}$$

For $U_{amb} = 1$ and for $U_{amb} = 0$ an explicit solution for equation 2.12 can be obtained:

$$T_C = T_M - \frac{(1 - U_{amb}) e_{sat}(T_M)}{G} \tag{2.13}$$

On the other hand, for $0 < U_{amb} < 1$, equation 2.12 is solved iteratively for a given value of U_{amb} and G.

Alternatively, a different threshold criterion for the formation of contrails could be used; instead of having $T < T_{\mathrm{C}}$, the requirement would be for the ambient relative humidity, U_{amb}, to stay above a critical relative humidity value, U_C, calculated according to equation 2.14 [4][41].

$$U_C = \frac{G(T - T_M) + e_{sat}(T_M)}{e_{sat}(T_E)} \tag{2.14}$$

The criterion selected to determine the formation of contrails was the threshold temperature. No validation data was found for equation 2.14 that could be used to compare to the results and reliably validate them, and since the iterative method used to obtain the threshold temperature did not lead to a significant increase in the computation time of the model, this was a decisive factor.

Figure 2.2 shows a comparison between the values obtained in this study with those expected. In this figure, the continuous thick line is the temperature profile of the International Standard Atmosphere (ISA).

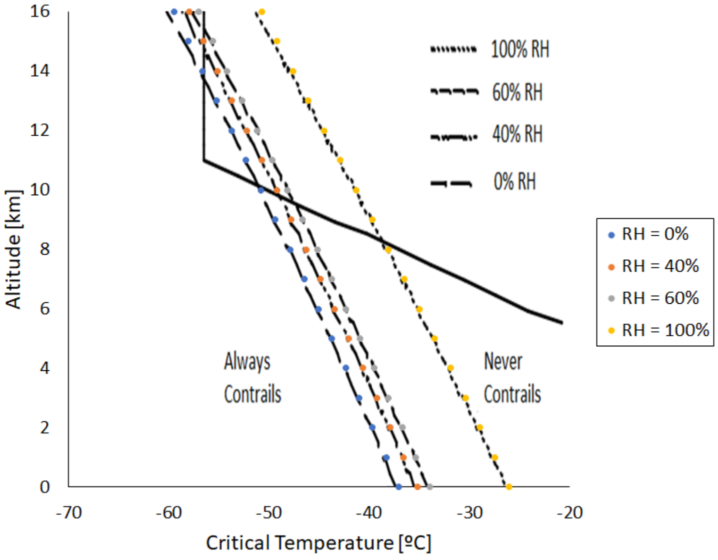

Figure 2.2: Threshold temperatures computed for 0 %, 40 %, 60 % and 100 % relative humidity with engine and fuel parameters $\eta = 0.3$, $EI_{H_2O} = 1.223$ and $Q = 43$ MJ/kg. Comparison is done with adapted plot from reference [42].

2.2 Young Contrails - Wake Vortex Downwash

Young contrails interact with the engine jet, the aircraft wake vortex, and with ambient turbulence, stratification and wind shear. The details of this interaction are aircraft dependent; a larger aircraft has a higher fuel consumption, tends to emit more water and soot particles, and causes deeper wake vortex sinking which leads to a thicker contrail. The lifetime of the potential contrail cirrus depends heavily on the number of ice crystals formed by soot and volatile aerosols in the jet phase, and on the number of ice particles which survive the adiabatic heating in the initially sinking wake vortex [8].

This section focuses on this initial phase of the contrail life-cycle with the aim of obtaining the surviving ice particle number, the ice mass in the contrail and the contrail dimensions after this phase. The details of the complex jet and wake dynamics in the first few minutes are not resolved, instead the properties of the contrail at the end of the wake vortex phase are estimated as a function of aircraft and atmospheric parameters; since the global climate impact from contrails comes mainly from them surviving far longer than this phase, this choice is admissible [4].

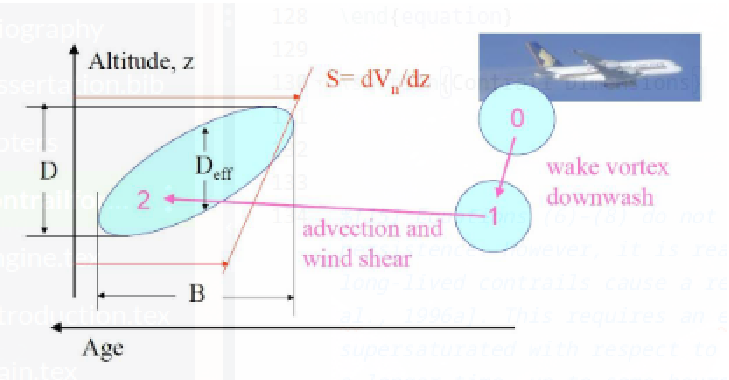

Figure 2.3: Schematic of contrail dynamics with altitude and contrail age with plume depth D, plume width B, and normal shear velocity S. Stage 0 represents the contrail at the time of formation, stage 1 represents the contrail after sinking due to the wake vortex downwash, and stage 2 represents the cross-section of an aged contrail [4].

2.2.1 Contrail Dimensions

The wake vortex model implemented is the Probabilistic Two-Phase Aircraft Wake-Vortex Model (P2P) [43][44]. It is formulated in normalized form, with the characteristic scales being based on initial vortex separation, b_0, and circulation, $\mathit{\Gamma}_0$; this leads to the timescale, t_0, represented in equation 2.15c.

$$b_0 = \pi \frac{s_a}{4} \tag{2.15a}$$

$$\mathit{\Gamma}_0 = \frac{4 M_a g}{\pi s_a \rho TAS} \tag{2.15b}$$

$$t_0 = \frac{2\pi b_0^2}{\mathit{\Gamma}_0} \tag{2.15c}$$

$$w_0 = \frac{\mathit{\Gamma}_0}{2\pi b_0} \tag{2.15d}$$

As previously stated, the aircraft dimensions have a strong influence on the wake vortex, which is reflected in the characteristic scales. The initial vortex separation is proportional to the aircraft wingspan, s_a, and the circulation is a function of both the aircraft wingspan and aircraft mass, s_a and M_a.

The EDR, ϵ, an aircraft-independent measure of environmental turbulence[3], is normalized in this model according to equation 2.16a, using the initial vortex separation, b_0, and the initial descent speed,

---

[3] The EDR is the ”rate at which the turbulence energy is absorbed by breaking the eddy down into smaller and smaller eddies until it is ultimately converted into heat by viscous forces” - (Huang, 2019) [45]

w_0.

$$\epsilon^* = \frac{(\epsilon b_0)^{\frac{1}{3}}}{w_0} \tag{2.16a}$$

$$N_{bv}^* = N_{bv} t_0 \tag{2.16b}$$

The model distinguishes between weak and strong stable stratification of the environment through the use of the Brunt-Väisälä frequency, which is normalized as in equation 2.16b.

The Brunt-Väisälä frequency is the natural frequency at which a displaced air parcel would oscillate around its origin in stably stratified conditions. It is computed as in equation 2.17a, where g is the gravitational acceleration and θ is the potential temperature a parcel of dry air at temperature T_E and pressure P_E would have if brought adiabatically and reversibly to the reference pressure $P_{ref} = 1000$ mbar [8].

$$N_{BV} = \sqrt{\frac{g}{\theta}\frac{d\theta}{dz}} \tag{2.17a}$$

$$\theta = T_E \left(\frac{P_{ref}}{P_E}\right)^{\frac{R_{air}}{c_p}} \tag{2.17b}$$

The maximum descent value, $\mathit{\Delta} z_w$, will be larger than the fracion $\frac{w_0}{N_{BV}}$ for a pure Brunt-Väisälä oscillation due to the additional rotational momentum in the sinking and rotating vortices. Depending on the normalized Brunt-Väisälä factor, this value can be calculated using one of the equations 2.18.

$$\begin{cases} \mathit{\Delta} z_w = 1.49\frac{w_0}{N_{bv}} & \text{for } N_{bv}^* \geq 0.8 \\ \mathit{\Delta} z_w = (7.68(1 - 4.07\epsilon^* + 5.67\epsilon^{*2})(0.79 - N_{bv}^*) + 1.88)b_0 & \text{for } N_{bv}^* < 0.8 \wedge \epsilon^* \leq 0.36 \end{cases} \tag{2.18}$$

The wake vortex reaches the maximum descent value at times 5 to 12 times larger than t_0; these times vary with stratification, and make it so the value is only achieved at distances up to 50 km behind the aircraft. Due to this, the maximum descent value ends up being rarely ever observed in the atmosphere. Taking this into account, the initial sinking from point 0 to point 1, as represented in figure 2.3, is taken not as the maximum value, $\mathit{\Delta} z_w$, but as a fraction C_{z1} of it [4].

$$\mathit{\Delta} z_1 = C_{z1} \mathit{\Delta} z_w \tag{2.19a}$$

$$D_1 = C_{D0} \mathit{\Delta} z_w \tag{2.19b}$$

$$B_1 = \frac{N_{dil}(t_0) m_F}{\frac{\pi}{4}\rho D_1} \tag{2.19c}$$

The parameters used in equations 2.19a and 2.19b are set, as in reference [4], to $C_{z1} = 0.25$ and $C_{D0} = 0.5$. The value for C_{z1} comes from the assumption that, mostly due to buoyancy, the center of the contrail will start higher than the halfway point between the initial and the maximum sinking distance. The value for C_{D0} is in reference [4] picked due to tests showing that larger values for the initial depth, D_1, led to too large a dilution when compared to observations.

The initial width, B_1, was parametrized so that at time t_0 the dilution fit an empirical equation that is often used, which also works towards making the computed dilution of the model closer to observations. This empirical equation, equation 2.20, calculates the dilution ratio, N_{dil}, which represents the ratio between contrail mass and fuel per length. In this equation, t_s is set to 1.

$$N_{dil}(t) = 7000 \left(\frac{t}{t_s}\right)^{0.8} \tag{2.20}$$

Table 2.1 shows the comparison between the measured values and those computed in this work for an aircraft with dimensions equivalent to an A319-111, flying at $TAS = 224$ m/s on flight level $FL = 320$ hft. This was one of the aircraft for which measurements were made in reference [46], and it was chosen since its dimensions were the closest to what an aircraft with the modeled engine would have.

	Measured [46]	Predicted	Error [%]
T [K]	217	216.62	0.18 %
N_{BV} [/s]	0.017	0.011	35.29 %
$\epsilon*$ [m^2/s^3]	4.75x10^{-6}	4.805x10^{-6}	-1.16 %
b_0 [m]	26.8	26.78	0.075 %
t_0 [s]	22.7	22.49	0.93 %
Δz_{max} [m]	120	143.29	-19.41 %

Table 2.1: Comparison of predicted and measured values for an aircraft with $M_a = 47000$ kg, $s_a = 34.1$ m, flying at $TAS = 224$ m/s at an altitude of 320 hft.

The largest difference comes from the computed Brunt-Väisälä frequency, which shows an error of 35.29 %. This can be shown to be responsible for the –19.41 % error in the maximum displacement value; if the Brunt-Väisälä frequency is set to $N_{BV} = 0.017$, the value obtained is $\Delta z_{max} = 120.5992$ m, with an error of only –0.05 %. Nevertheless, a difference of 20 or even 30 meters between the measured and computed values was expected and is still acceptable.

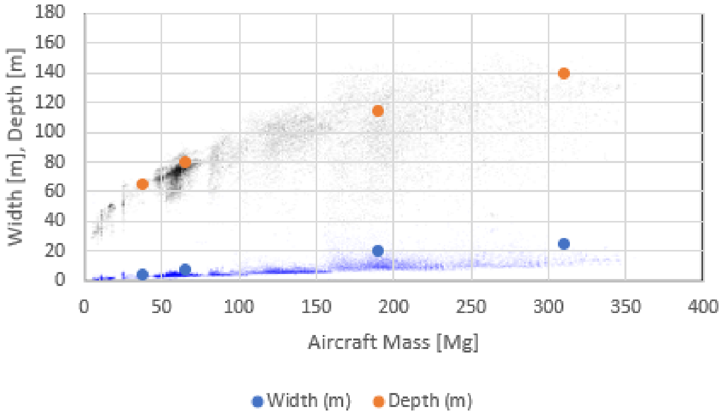

Figure 2.4: Depth and width at point 1 computed for BAe 146 ($s_a = 34.1$ m, $M_a = 38.1$ Mg) and example large, medium and small aircrafts with parameters obtained from reference [4], juxtaposed over plot where each point represents an aircraft flying over the North Atlantic during 6-9 June 2006.

Figure 2.4 represents the predicted values for the initial contrail dimensions at point 1 for different aircraft. The smallest example aircraft has the same dimensions as the BAe 146, the aircraft used for the simulations in this work, and the remaining aircraft are example aircraft of the types B747, A330 and B737, with aircraft mass, wing span, flight speed and fuel flow taken from reference [4]. The predicted values show an overall good agreement with the observed trend, with the largest deviation from the mean being for the initial width of the example large aircraft, with it nevertheless remaining within the expected values.

2.2.2 Contrail Ice Properties

To simulate the contrail ice properties at the different stages of its life, two plume bulk ice-quantities are used: the mass mixing ratio of ice in the contrail, I, and the total number concentration of contrail ice particles per contrail length, N_i.

The contrails are taken as being in thermal equilibrium with the ambient air in the phase after contrail formation, which allows I to be computed from pure thermodynamics, without the need for an additional budget equation for heat. Acknowledging thermal equilibrium carries with it two assumptions.

The first assumption is that the plume vapour inside an effective cross-section area, A, of the contrail plume is at ice saturation at all times; this is supported for contrails after the vortex formation phase both by large eddy simulations and by measurements.

The second assumption is that the temperature increase caused first by the combustion heat and then by sublimation in the plume is small after only a few seconds of contrail age.

To check the validity of this assumption combustion induced heat is considered first. The temperature increase caused by the released combustion heat can be computed using equation 2.21. Using typical values for the net heat of combustion and propulsion efficiency, and using equation 2.20 to calculate the dilution factor, the plot in figure 2.5a is obtained. It can be seen that the temperature increase due to the combustion drops quickly in the first few seconds, reaching 0.3 K in around half a minute and dropping below 0.1 K in around 100 s.

$$(\mathit{\Delta} T)_{comb} = \frac{(1-\eta)Q}{c_p N_{dil}(t)} \tag{2.21}$$

$$IWC = 1 \times 10^{-6} exp(6.97 + 0.103T[^{\circ}C]) \tag{2.22}$$

Considering now the sublimation heat, the typical Ice Water Content (IWC) of a contrail cirrus can be estimated using equation 2.22, which was fitted in reference [4] to measurements published in reference [47], and is presented here in figure 2.5b. For cold air, with a temperature below 240 K, corresponding roughly to an altitude of 7500 m in the ISA, if all the water in a typical contrail cirrus were to get sublimated, it would still lead to a temperature variation of less than 0.1 K.

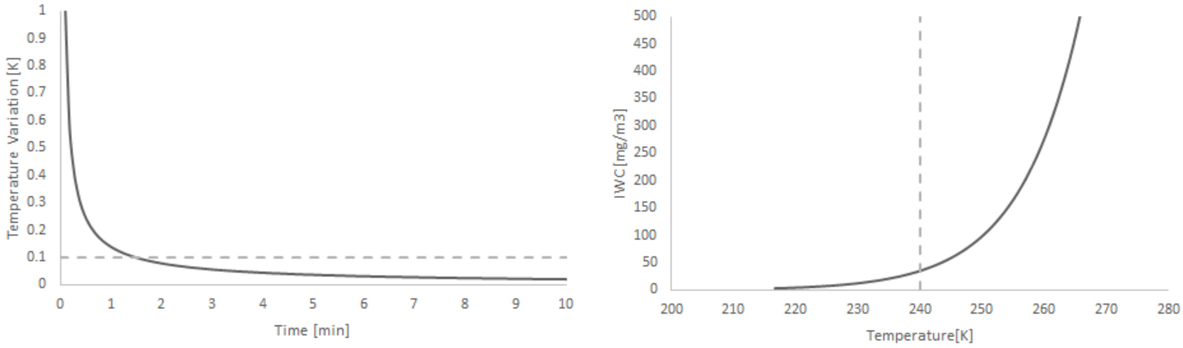

(a) Combustion induced temperature with a reference line marking 0.1 K.

(b) Contrail cirrus water content with a reference line marking 240 K.

Figure 2.5: Plots of combustion induced temperature increase in relation to time and the typical contrail cirrus IWC in relation to ambient temperature.

The mass mixing ratio of ice in the contrail at the time of its formation, I_0, can be obtained from equation 2.23. The first term in the equation is the water mass emitted by the engines per flight distance, while the other two are the ambient humidity, q_0, and the saturation humidity, $q_{sat}(P_0, T_0)$, at point 0. These last two terms measure the amount of water above ice saturation available in the environment which will be deposited on ice particles at ice saturation, becoming part of the contrail.

$$I_0 = \frac{EI_{H_2O} m_F}{\frac{\pi}{4}\rho D_1 B_1} + q_0 - q_{sat}(P_0, T_0) \tag{2.23}$$

During the initial sinking with the wake vortex from point 0 to point 1, part of the initial ice mass of the contrail will sublimate due to adiabatic heating. This variation in ice mass can be calculated as in equation 2.25a, where subscript 0 and 1 represent point 0 and point 1 respectively, and the adiabatic temperature variation, $(\varDelta T)_{ad}$ is calculated as in equation 2.25b.

$$I_1 = I_0 - \varDelta I_{ad} \tag{2.24}$$

$$\varDelta I_{ad} = \frac{P_{ice}(T_0 + \varDelta T_{ad})}{P_1} - \frac{P_{ice}(T_0)}{P_0} \tag{2.25a}$$

$$\varDelta T_{ad} = T_0 \frac{R_{air}}{c_p} \frac{P_1 - P_0}{P_0} \tag{2.25b}$$

It is to be noted that if at any point the ice mass of the contrail reaches zero, $I \leq 0$, this symbolizes the end of the contrail life cycle.

Contrail ice particles are a result of liquid droplets forming by nucleation on emitted and ambient aerosols[4] and freezing shortly after. The initial number of ice particles, $N_{i,0}$, is set here as the number of soot particles which were emitted during combustion, equation 2.26. While in principle volatile aerosols can also become nucleus for the ice particles, their contribution is relatively small for typical soot emissions and moderately low temperatures; for the case of sulfur content, analysis of experiments with fuels with different sulfur content values have shown that an increase from 6 µg/g to 2800 µg/g in fuel sulfur content[5] led to an increase in ice particles by a factor of merely 1.3 [4].

$$N_i = \frac{EI_N m_F}{TAS} \tag{2.26}$$

Only a fraction of the ice crystals in this initial phase survive the vortex phase. The potential initial supersaturation gets reduced before the vortex phase ends by the quick deposition of humidity on ice particles, and the adiabatic heating causes local sub-saturation around the ice particles; this results in ice particle sublimation and the disappearance of some particles. The sinking of the vortex into dry air can also lead to turbulent detrainment, causing particle losses which are dependent on the aircraft type, speed and mass, its soot and heat emissions, ambient humidity, temperature, stratification turbulence, shear winds and particle sizes.

In the model, this is represented by a survival factor, f_{surv}, which is equated to the survival factor of ice mass. In principle, since ice mass and ice number evolve different, the survival factors should be different. Further studies into the evolution of ice particles during the vortex phase could provide a more accurate survival factor, but at present this approximation will be used.

$$f_{surv} = \frac{I_1}{I_0} \tag{2.27a}$$

$$N_{i,1} = f_{surv} N_{i,0} \tag{2.27b}$$

2.3 Contrail Cirrus

The climatic impact of contrail cirrus is assessed by its RF during its entire lifecycle, which is dependent on the contrail optical depth and width. Since this is the case, we seek to not only determine how long the contrail lasts, but also the characteristics which allow us to determine its potential climatic impact.

---

[4] These are not taken into account in the model, a simplification which is backed up by the data presented in figure 1.5.

[5] Aviation fuel has a typical fuel sulfur content of around 600 µg/g, well below the maximum fuel sulfur content tested [48].

2.3.1 Trajectory

The first thing the model calculates for each time step is the contrail location; every other parameter has a strong dependence on it.

The location of the contrail is set in three-dimensional space to account for the variation with longitude and latitude of the environmental parameters it requires in its calculations. For the horizontal trajectory the position is given according to its longitude, x, and latitude, y, while for the vertical trajectory the position is given according to the ambient pressure, P.

To calculate the trajectory, which will be referred to as a vector $\mathbf{X} = (x, y, P)$, the model uses the standard second-order two-step Runge-Kutta scheme. This is represented in equations 2.28a and 2.28b, where $\tilde{\mathbf{X}}(t + \varDelta t)$ is the predictor step for time $(t + \varDelta t)$, and $\mathbf{X}(t + \varDelta t)$ is the value after the time step.

$$\tilde{\mathbf{X}}(t + \varDelta t) = \mathbf{X}(t) + \varDelta t \frac{\partial \mathbf{X}(t)}{\partial t} \tag{2.28a}$$

$$\mathbf{X}(t + \varDelta t) = \mathbf{X}(t) + \frac{\varDelta t}{2} \left(\frac{\partial \mathbf{X}(t)}{\partial t} + \frac{\partial \tilde{\mathbf{X}}(t + \varDelta t)}{\partial t} \right) \tag{2.28b}$$

The time derivatives for each position are given by equations 2.29a, 2.29b and 2.29c. For the latitude and longitude time derivatives, U represents the eastward wind in m/s and V represents the northward wind in m/s. For the pressure time derivative it is assumed that the contrail follows the mid point of the bulk of ice particles under sedimentation, being displaced downward according to the particle terminal fall velocity, V_T, computed in m/s. In equation 2.29c, ω represents the vertical pressure change rate in Pa/s, g the gravitational acceleration in m/s^2 and ρ_{air} the air density.

$$\frac{\partial x}{\partial t} = U \tag{2.29a}$$

$$\frac{\partial y}{\partial t} = V \tag{2.29b}$$

$$\frac{\partial P}{\partial t} = \omega + \rho_{air} g V_T \tag{2.29c}$$

The longitude and latitude are computed according to the travelled distance in meters from time t to time $t + \varDelta t$, that is, they are not computed in degrees in equations 2.28a and 2.28b, but instead in meters. The segments travelled are then converted to degrees using equations 2.30a and 2.30b, where R_{earth} is the Earth's radius at the equator.

$$y(t + \varDelta t)[°] = y(t)[°] + \frac{\varDelta y}{R_{earth}} \frac{180}{\pi} \tag{2.30a}$$

$$x(t + \varDelta t)[°] = x(t)[°] + \frac{\frac{\varDelta x}{R_{earth}} \frac{180}{\pi}}{cos\left(\frac{\varDelta y}{R_{earth}} \frac{180}{\pi}\right)} \tag{2.30b}$$

2.3.2 Contrail Dimensions and Optical Depth

As stated previously, the optical depth of a contrail is of great importance to determine its potential environmental impact. The contrail optical depth, τ, will vary during its lifetime and is dependant on the contrail's dimensions - that is, its depth, width, and effective area - for each time-step.

In this model, the contrail's concentration field is approximated as a Gaussian function with a given width, B, depth, D, and inclination. Aged contrails often have a shape not too different from this Gaussian plume shape, but the initial jet exhaust, wake vortex and young contrail's shape is often quite different.

In the calculations for point 1 the contrail is assumed to be symmetrical, as seen in figure 2.3, but with time its cross-section grows and inclines due to vertical shear[6], S, and horizontal, D_H, vertical, D_V, and shear, D_S, diffusitivies.

The plume dimensions and inclination are obtained using the analytic relations derived by Konopka [49]. In this model the concentration, c, of a species per air mass in the plane perpendicular to the contrail axis is approximated as function of the position vector $\mathbf{x}$ as seen in equation 2.31a, where C_0 is the mass of the species per plume length and C_0/A is the volume specific concentration in the center of the plume. These equations are in relation to local orthogonal coordinates (x_P, y_P, z_P) relative to the plume axis, where x_P is the flight direction, y_P is the cross-direction and z_P is the vertical direction.

$$c(\mathbf{x}) = \frac{C_0}{A} exp(-\frac{1}{2}\mathbf{x}^T \sigma^{-1}\mathbf{x}) \tag{2.31a}$$

$$\mathbf{x} = (y_P, z_P)^T \tag{2.31b}$$

The effective cross-sectional area of the contrail can be obtained from an integral over y and z, as seen in equation 2.32, where $\sigma(\mathbf{x}, t)$ is the covariance matrix of the concentration field $\mathbf{x}$ in the plane for unit mass content ($C_0 = 1$) - as seen in equation 2.33.

$$A = \int\int exp(-\frac{1}{2}\mathbf{x}^T \sigma^{-1}\mathbf{x}) d\mathbf{x} = 2\pi(det(\sigma))^{\frac{1}{2}} \tag{2.32}$$

$$\sigma = \int\int (\mathbf{x} \otimes \mathbf{x}) c(\mathbf{x}) d\mathbf{x} \tag{2.33}$$

The components of the covariance matrix describe a real symmetric and positive definite matrix, with a determinant as given in equation 2.34b.

$$\sigma = \begin{pmatrix} \sigma_{yy} & \sigma_{yz} \\ \sigma_{yz} & \sigma_{zz} \end{pmatrix} \tag{2.34a}$$

$$det(\sigma) = \sigma_{yy}\sigma_{zz} - \sigma_{yz}^2 \tag{2.34b}$$

These components are calculated for each time step as a function of shear, and the horizontal, vertical and shear diffusitivies, which, as stated previously, control the cross-sectional growth and inclination.

$$\begin{split} \sigma_{yy}(t + \varDelta t) = \left(\frac{2}{3}S^2 D_V \varDelta t^3 + \left(S^2 \sigma_{zz}(t) + 2D_S S\right)\varDelta t^2 + \right. \\ \left. +2\left(D_H + S\sigma_{yz}(t)\right)\varDelta t + \sigma_{yy}(t)\right)\left(\frac{L(t)}{L(t+\varDelta t)}\right)^2 \end{split} \tag{2.35a}$$

$$\sigma_{zz}(t + \varDelta t) = 2D_V \varDelta t + \sigma_{zz}(t) \tag{2.35b}$$

$$\sigma_{yz}(t + \varDelta t) = \left(S D_V \varDelta t^2 + (2D_S + S\sigma_{zz}(t))\varDelta t + \sigma_{yz}(t)\right)\frac{L(t)}{L(t+\varDelta t)} \tag{2.35c}$$

These equations take into account the changes in segment length, L, from time-step to time-step. The segment length can vary from waypoint to waypoint due to the advection of the contrail: horizontally diverging wind fields can result in significant differences between the segment length between time steps. Additionally, they can reduce the cross-section area since, due to continuity, horizontal divergence is connected with convergence in vertical planes. The segment length variation from time t to time $t + \varDelta t$ is computed as in equation 2.36.

$$\varDelta L = \sqrt{\varDelta x[m]^2 + \varDelta y[m]^2 + \varDelta z[m]^2} \tag{2.36}$$

---

[6] Shear is the vertical gradient of the horizontal wind velocity normal to the contrail axis, $\frac{\partial V_n}{\partial z}$

For the sake of thoroughness, the analytical solution for the effective cross-sectional area of the contrail, A, is shown in equation 2.37. This equation is not used in the model, being the effective cross-sectional area instead computed from the covariance matrix determinant as seen in equation 2.32.

$$\begin{aligned} A(t+\Delta t) = 2\pi \Bigg[& \frac{1}{3}S^2 D_V^2 \Delta t^4 + \frac{2}{3}S^2 D_V \sigma_{zz}(t)\Delta t^3 + \\ & +(2SD_V\sigma_{zz}(t) - 2SD_S\sigma_{zz}(t) + 4D_H D_V - 4D_S^2)\Delta t^2 + \\ & +(2D_V\sigma_{zz}(t) + 2D_H\sigma_{zz}(t) - 4D_S\sigma_{yz}(t))\Delta t + \\ & +\sigma_{yy}(t)\sigma_{zz}(t) - \sigma_{yz}^2(t) \Bigg]^{\frac{1}{2}} \end{aligned} \tag{2.37}$$

The width and the depth of the contrail for each time-step is then calculated from the covariance matrix components as shown in equations 2.38a and 2.38b.

$$B = \sqrt{8\sigma_{yy}} \tag{2.38a}$$

$$D = \sqrt{8\sigma_{zz}} \tag{2.38b}$$

The optical depth is finally obtained as a function of the contrail depth, its cross-sectional area and, the extinction, β, which can be computed from equation 2.40. When the optical depth reaches a small enough value, $\tau < 10^{-4}$, the simulation ends.

$$B\tau = \beta \int\int exp\left(-\frac{1}{2}\mathbf{x}^T\sigma^{-1}\mathbf{x}\right) dzdy = \beta A \tag{2.39}$$

$$\beta = \frac{3Q_{ext}\rho_{air}I}{4\rho_{ice}r_{eff}} \tag{2.40}$$

The extinction is a function of the radiation extinction efficiency, Q_{ext}, which can be computed as seen in equation 2.41a, the effective particle radius, r_{eff}, which is a computed as seen in equation 2.42a, the mass ratio of ice in the contrail, and the densities of the air and ice.

$$Q_{ext} = 2 - \frac{\frac{4}{\rho_\lambda}(sen(\rho_\lambda) - (1 - cos(\rho_\lambda)))}{\rho_\lambda} \tag{2.41a}$$

$$\rho_\gamma = 4\pi r_{eff}\frac{k-1}{\gamma} \tag{2.41b}$$

The radiation extinction efficiency is computed using approximate Mie-theory, where ρ_λ, the normalized size parameter, is obtained from equation 2.41b. In this equation $k = 1.31$ is the real refractive index of ice and $\lambda = 550$ nm is the wavelength of visible light.

The effective particle radius is the ratio of the particle volume, V_p, and the particle projected area, A_p. It can also be obtained from a set ratio C_r between the volume mean radius and the effective radius; this ratio has a value of 0.9 ± 0.3 which depends on the particle shape and the size distribution of the ice particles, both of which are variable.

$$r_{eff} = \frac{3V_p}{4A_p} = \frac{r_P}{C_r} \tag{2.42a}$$

$$r_P = \left(\frac{\rho_{air}I}{n\rho_{ice}\frac{4\pi}{3}}\right)^{\frac{1}{3}} \tag{2.42b}$$

The particle volume mean radius is computed according to equation 2.42b. It is a function of the air and ice density, the ice mass ratio in the contrail, and of the ice particle number concentration per volume, $n = \frac{N_i}{A}$.

2.3.3 Ice Mass and Particle Number

As previously stated, this model takes the ice mass ratio in a contrail reaching zero as the end of the contrail lifetime. Since this is the case, this value must be computed for each time step to determine when it should be stopped.

During the lifetime of the contrail, the water mass in the plume will mix with the ambient air humidity, changing its ice content. To simulate this the model takes into account the mass budgets of the contrail air mass, M_{air}, and the contrail water mass, M_{H_2O}, the latter of which is composed both of water in the ice and vapor phase at ice saturation. The humidity inside the plume is considered to be at ice saturation, $q_P = q_{sat}$, as in section 2.2.

$$M_{air} = \rho_{air} A L \tag{2.43a}$$

$$M_{H_2O} = M_{air}(I + q_{sat}) \tag{2.43b}$$

The change in the water mass content from one time-step to the next is, as stated before, a result of the mixing of the contrail water mass with the humid ambient air; this process is expressed in equation 2.44, where q_E is the ambient humidity.

$$M_{H_2O}(t + \mathit{\Delta} t) = M_{H_2O}(t) + (M_{air}(t + \mathit{\Delta} t) - M_{air}(t))q_E = M_{H_2O}(t) + \mathit{\Delta} M_{air} q_E \tag{2.44}$$

The mass mixing ratio of ice in the contrail for each time step is computed from equation 2.45, which is obtained from equations 2.43a and 2.44. In these equations, q_E is taken as the mean value between the times t and $(t + \mathit{\Delta} t)$.

$$I(t + \mathit{\Delta} t) = \frac{M_{air}(t)(I(t) + q_{sat}(t)) + \mathit{\Delta} M_{air} q_E}{M_{air}(t + \mathit{\Delta} t)} - q_{sat}(t + \mathit{\Delta} t) \tag{2.45}$$

The ice particle number concentration per volume, that is $n = \frac{N_i}{A}$, is an important parameter for the computation of the contrail optical depth. A particle loss model is implemented to account for changes in the particle number; it is represented in equation 2.46.

$$\left(\frac{dN_i}{dt}\right)_{loss} = \left(\frac{dN_i}{dt}\right)_{turb} + \left(\frac{dN_i}{dt}\right)_{agg} \tag{2.46}$$

Two sources for particle loss are considered. The first is the plume-internal turbulence, that is, the sublimation of smaller particles during the turbulent mixing of the contrails with dry ambient air. The second is the sedimentation-induced aggregation, that is, the process in which large falling ice particles collide and aggregate with smaller ice particles, decreasing in this way the particle number.

The turbulence losses, as shown in equation 2.47a, are a function of the vertical and horizontal diffusivities and the contrail's depth, width and effective depth, $D_{eff} = \frac{A}{B}$. The aggregation losses, as shown in equation 2.47b, are a function of the mean volume particle radius, the particle terminal fall velocity, and the ice particle number concentration per volume. E_T and E_A are adjustable parameters which in this work are set to 1.

$$\left(\frac{dN_i}{dt}\right)_{turb} = -E_T \left(\frac{D_H}{max(B, D)^2} + \frac{D_V}{D_{eff}^2}\right) N_i \tag{2.47a}$$

$$\left(\frac{dN_i}{dt}\right)_{agg} = -E_A 8 \pi {r_p}^2 V_T n N_i \tag{2.47b}$$

The ice crystal terminal fall velocity can be computed using equation 2.48, where μ_{air} is the air dynamic viscosity, D_{ice} is the maximum dimension of an ice crystal and Re is the Reynolds number.

$$V_T = Re\frac{\mu_{air}}{D_{ice}\rho_{air}} \tag{2.48}$$

The Reynolds number can be obtained using its relationship with the Best number, X, as seen in equation 2.49a. The power law coefficients for this equation are computed as shown in equations 2.49b and 2.49c, where $a_0 = 1.7 \times 10^{-3}$ and $b_0 = 0.8$. Using $\delta_0 = 5.83$ and $K_0 = 0.6$ to describe the surface roughness, the other power law coefficients are computed as shown in equations 2.49d and 2.49e.

$$Re = a_1 X^{b_1} \tag{2.49a}$$

$$a_1 = \frac{K_2\left(\sqrt{1+K_1X^{\frac{1}{2}}}-1\right)^2 - a_0X^{b_0}}{X^{b_1}} \tag{2.49b}$$

$$b_1 = \frac{K_1X^{\frac{1}{2}}}{K_2\left(\sqrt{1+K_1X^{\frac{1}{2}}}-1\right)\sqrt{1+K_1X^{\frac{1}{2}}}} - \frac{a_0b_0X^{b_0}}{K_2\left(\sqrt{1+K_1X^{\frac{1}{2}}}-1\right)^2} \tag{2.49c}$$

$$K_1 = \frac{4}{\delta_0^2K_0^{\frac{1}{2}}} \tag{2.49d}$$

$$K_2 = \frac{\delta_0}{4} \tag{2.49e}$$

The Best number can be obtained from equation 2.50a, where $\frac{m_{ice}}{A_{ice}}$ is the ice mass to area ratio and can be computed according to the relationship 2.50b [50].

$$X = \frac{2g\rho_{air}}{\mu_{air}^2}D_{ice}\frac{m_{ice}}{A_{ice}} \tag{2.50a}$$

$$\frac{m_{ice}}{A_{ice}} = 0.0228D_{ice}^{0.59} \tag{2.50b}$$

The ice crystal maximum dimension, D_{ice}, used in these equations was obtained from measurements made in ice clouds; these measurements were made available for pristine columns, plates, and component bullets of bullet rosettes. The maximum dimension of a crystal varies with temperature and crystal shape. For this model, bullet rosettes were chosen; their maximum dimension variation with temperature is shown in figure 2.6 [51].

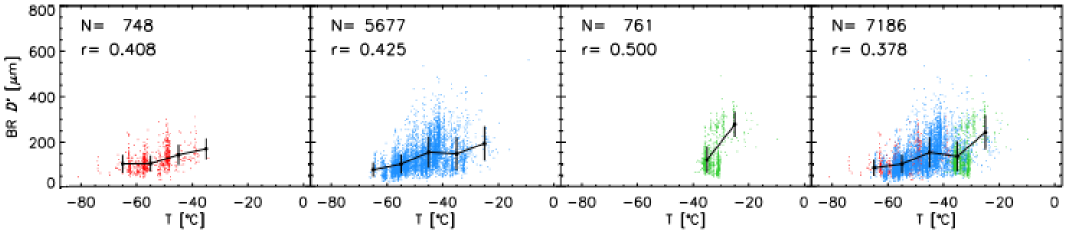

Figure 2.6: Variation with temperature of the measured mean maximum dimension for each bullet component in a bullet rosette [51].

Returning to the equation for the particle losses, equation 2.46, it can be seen that it is of the same type as equation 2.51a, which when integrated has a solution of the type of equation 2.52.

$$N_i' = -\alpha_1N_i^2 - \alpha_2N_i \tag{2.51a}$$

$$N_i(0) = N_{i,0} \tag{2.51b}$$

$$N_i(t) = \frac{N_{i,0}\alpha_2 \exp -\alpha_2 t}{\alpha_2 + \alpha_1 N_{i,0}\left(1 - \exp -\alpha_2 t\right)} \tag{2.52}$$

A solution for the integration of equation 2.46 can therefore be obtained by following equation 2.52. $N_{i,0}$ is set as $N_i(t)$, the start of the time-step, and α_1 and α_2 are computed from equations 2.54a and 2.54b. The solution must also be multiplied by a segment length corrector factor to account for the segment variation between time steps. With this, the ice particle number equation for each time step, equation 2.53, is obtained.

$$N_i(t + \varDelta t) = \frac{N_i(t)\alpha_2 \exp -\alpha_2 \varDelta t}{\alpha_2 + \alpha_1 N_i(t)\left(1 - \exp -\alpha_2 \varDelta t\right)} \frac{L(t)}{L(t + \varDelta t)} \tag{2.53}$$

$$\alpha_1 = -\frac{\varDelta t}{N_i^2}\left(\frac{dN_i}{dt}\right)_{agg} \tag{2.54a}$$

$$\alpha_2 = -\frac{\varDelta t}{N_i}\left(\frac{dN_i}{dt}\right)_{turb} \tag{2.54b}$$

Chapter 3

Soot Model

Three soot models were studied to ascertain the viability of implementing them. The model implemented was the Rizk and Mongia Model for a 0-D engine [52], but all three models are expanded upon in this section for the sake of thoroughness and to contextualize the final model choice.

3.0.1 Leung *et al.* Model

The simplied four-step semi-empirical soot model by Leung *et al.* [53] uses acetylene as the sole soot precursor and oxygen as the oxidation agent. The soot formation steps implemented in this model, along with their associated, are summarized in table 3.1, where $C(s)$ is used to represent the soot molar concentration and N the soot particle number.

Step	Chemical Reaction	Rate Equation	Rate Constant
Nucleation	$C_2H_2 \rightarrow 2C(s) + H_2$	$k_1(T)[C_2H_2]$	$k_1(T) = 10^4 e^{-21100/T}$
Surface Growth	$C_2H_2 + C(s) \rightarrow 3C(s) + H_2$	$k_2(T)\sqrt{A_s}[C_2H_2]$	$k_2(T) = 6 \times 10^3 e^{-12100/T}$
Oxidation	$C(s) + 1/2\, O_2 \rightarrow CO$	$k_3(T)A_s[O_2]$	$k_3(T) = 10^4 T^{1/2} e^{-19680/T}$
Coagulation	$nC(s) \rightarrow C_n(s)$	$2C_a d_p^{1/2}\left(\frac{6k_BT}{\rho_s}\right)^{1/2} N^2$	-

Table 3.1: Reaction Rates for the Leung *et al.* model [53].

In the coagulation rate equation, Ca is the agglomeration rate constant, which in Leung *et al.* [53] takes the value of 9. The soot density, ρ_s, is assumed to be 2000 kg/m^3 and the Boltzmann constant, k_B, is 1.3806 x 10^{-23} m^{2}kg/(s^{2}K).

The surface growth and oxidation reaction rates are a function of the total soot surface area, A_s, while the coagulation rate is a function of the soot particle diameter, d_p. These are calculated, respectively, with equations 3.1a and 3.1b, which assume the soot particles to be spherical.

$$A_s = \pi d_p^2 N \tag{3.1a}$$

$$d_p = \left(\frac{6M_C[C(s)]}{\rho_s N}\right)^{2/3} \tag{3.1b}$$

The model calculates both the soot mass, c_S, and the soot particle number, N, using different steps. The reactions used to predict each value can be seen in equations 3.2a and 3.2b, where $\dot{R}_i$ represents the reaction rates for step i. $Na = 6.022 \times 10^{23}$ mol^{-1} is Avogadro's number, and C_{min} is the number of carbon atoms in an incipient soot particle. Assuming a diameter of 1.28 nm for these, it results in a value of around $C_{min} = 100$ carbon atoms [54].

$$\frac{d}{dt}(c_S) = M_C \left(\dot{R}_{nucleation} + \dot{R}_{surfacegrowth} - \dot{R}_{oxidation} \right) \tag{3.2a}$$

$$\frac{d}{dt}(N) = \frac{2Na}{Cmin} \dot{R}_{nucleation} - \dot{R}_{coagulation} \tag{3.2b}$$

The Leung *et al.* model [53] had many applications since it was first published, both in its entirety or with alterations to certain steps. The most common alterations made to this model focused on the oxidation step.

It was found that when the oxidation was modelled in relation solely to oxygen, it tended to underestimate the decrease in mass. The oxidation step is thus usually altered to have the OH radical as an oxidant, to have both O_2 and OH as oxidants, or even to have these two and the O radical as oxidants [55][56][57].

The Neoh *et al.*'s OH radical oxidation model [58], represented in equation 3.3, was considered as an alternative to this step, but ultimately decided against before final tests. For the purposes of this work, the accuracy provided by the original model was considered to be enough, and it does not require accurate predictions for OH radical concentrations which makes it easier to implement.

$$\dot{R}_{OHoxidation} = 0.39[OH]\sqrt{\frac{8RT}{\pi M_{OH}}} \tag{3.3}$$

Simplified chemical reactive systems are commonly used in combustion simulations where chemical kinetics play an important part. When it comes to soot formation simulations, the most commonly used set-up is a Well-Stirred Reactor (WSR) followed by a Plug-Flow Reactor (PFR); a schematic of these systems, along with the main variables and fluxes associated with them, is shown in figure 3.1 [59][60].

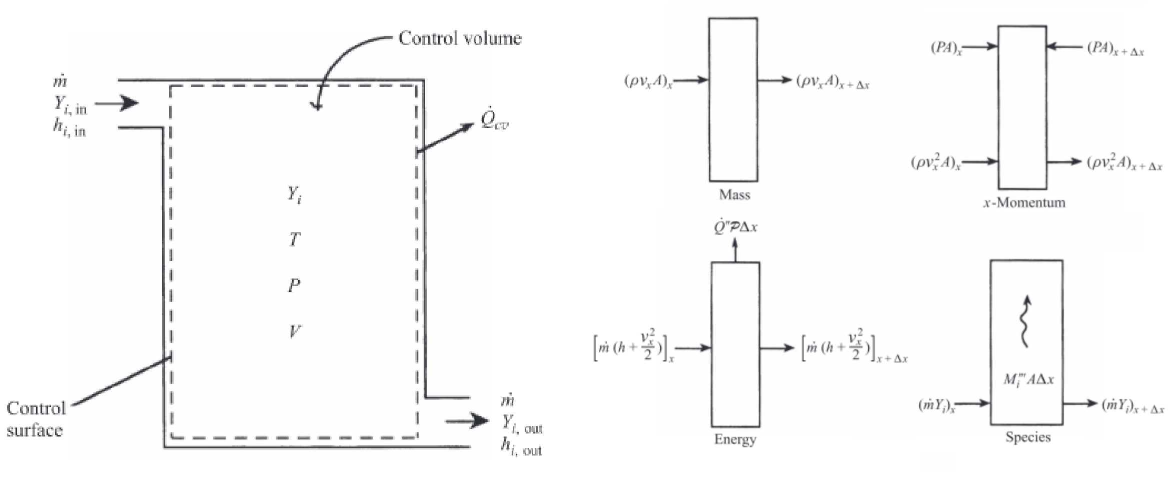
Control volume
$\dot{m}$
$Y_{i,\text{in}}$
$h_{i,\text{in}}$
$\dot{Q}_{cv}$
Y_i
T
P
V
Control surface
$\dot{m}$
$Y_{i,\text{out}}$
$h_{i,\text{out}}$
$(\rho v_x A)_x$
$(\rho v_x A)_{x+\Delta x}$
Mass
$(PA)_x$
$(PA)_{x+\Delta x}$
$(\rho v_x^2 A)_x$
$(\rho v_x^2 A)_{x+\Delta x}$
x-Momentum
$\dot{Q}''\mathcal{P}\Delta x$
$\left[\dot{m}\left(h+\frac{v_x^2}{2}\right)\right]_x$
$\left[\dot{m}\left(h+\frac{v_x^2}{2}\right)\right]_{x+\Delta x}$
Energy
$\dot{M}_i'''A\Delta x$
$(\dot{m}Y_i)_x$
$(\dot{m}Y_i)_{x+\Delta x}$
Species

(a) Well-stirred reactor.

(b) Plug-flow reactor.

Figure 3.1: Schematic of the simplified chemical reacting systems used in conjunction with the Leung *et al.* model [53][60].

The WSR is an ideal reactor in which perfect mixing is achieved inside the control volume. It was used to model the primary and secondary zones for this model.

Equation 3.4a represents the mass conservation for each species found inside the reactor. It equates the mass variation inside the control volume to the difference between the mass flow entering and exiting the control volume added to a generation term, $\dot{m}_i'''$.

The mass generation term, a term that is missing from the overall mass continuity equation, arises due to the chemical reactions transforming one species into another inside the control volume, causing the formation of some species and the destruction of others. It can be obtained from the reaction rates previously calculated through equation 3.4b, where $\dot{\omega}$ is the net production rate of the species and M_i is the molar mass of the species.

$$\frac{dm_{i,cv}}{dt} = \dot{m}_i'''V_c + \dot{m}_{i,in} - \dot{m}_{i,out} \tag{3.4a}$$

$$\dot{m}_i''' = \dot{\omega}_i M_i \tag{3.4b}$$

Taking the mass conservation equation and assuming steady-state operation, equation 3.5 is obtained, where m_i represents the mass fraction of the species entering or exiting the control volume, and $\dot{m}$ represents the total mass flow.

$$\dot{\omega}_i M_i V_c + \dot{m}(m_{i,in} - m_{i,out}) = 0 \tag{3.5}$$

The steady-state and steady-flow conservation of energy equation for the system, with changes in kinetic and potential energies neglected, is expressed in equation 3.6 in terms of the individual species.

$$\dot{Q} = \dot{m}\left(\sum_{i=1}^{N} m_{i,out}h_i(T_{out}) - \sum_{i=1}^{N} m_{i,in}h_i(T_{in})\right) \tag{3.6}$$

In the primary zone of a combustor, the temperature is assumed to be constant, while in the secondary zone the net heat is assumed to be null and the temperature is calculated from equation 3.6.

The PFR much like the WSR, is an ideal reactor that assumes steady-state and steady-flow. In this reactor there is no mixing in the axial direction and the properties are uniform in the direction perpendicular to the flow, making it an one-dimensional flow. It is further assumed that the flow is frictionless and that it displays ideal-gas behaviour.

The conservation equations for mass, x-momentum, energy and species, that is, equations 3.7a, 3.7b, 3.7c, and 3.7d, were obtained from reference [60]. In these equations v_x represents the axial velocity, and p_r represents the reactor perimeter.

$$\frac{d(\rho v_x A)}{dx} = 0 \tag{3.7a}$$

$$\frac{dP}{dx} + \rho v_x \frac{dv_x}{dx} = 0 \tag{3.7b}$$

$$\frac{d(h + v_x^2/2)}{dx} + \frac{\dot{Q}''p_r}{\dot{m}} = 0 \tag{3.7c}$$

$$\frac{dm_i}{dx} - \frac{\dot{\omega}_i M_i}{\rho v_x} = 0 \tag{3.7d}$$

The enthalpy equation, equation 4.1, can thus be exploited to obtain equation 3.8a.

$$\frac{dh}{dx} = c_p \frac{dT}{dx} + \sum_{i=1}^{N} \frac{dm_i}{dx} \tag{3.8a}$$

$$\frac{1}{P}\frac{dP}{dx} = \frac{1}{\rho}\frac{d\rho}{dx} + \frac{1}{T}\frac{dT}{dx} - \frac{1}{M_{mix}}\frac{dM_{mix}}{dx} \tag{3.8b}$$

The differentiated ideal-gas equation of state, equation 3.8b, is used to complete the mathematical description of the PFR. M_{mix} represents the molar mass of the mixture, with its derivative being expressed in equation 3.9b.

$$M_{mix} = \frac{1}{\sum_{i=1}^{N} \frac{m_i}{M_i}} \tag{3.9a}$$

$$\frac{dM_{mix}}{dx} = -M_{mix}^2 \sum_{i=1}^{N} \frac{1}{M_{mix}} \frac{dm_i}{dx} \tag{3.9b}$$

Isolating the variables in equations 3.7a and 3.7c and reducing the number of equations by substitution, the set of equations used to describe the PFR is obtained:

$$\frac{d\rho}{dx} = \frac{\left(1 - \frac{R_u}{c_p M_{mix}}\right) \rho^2 v_x^2 \left(\frac{1}{A}\frac{dA}{dx}\right) + \frac{\rho R_u}{v_x c_p M_{mix}} \sum_{i=1}^{N} M_i \dot{\omega}_i \left(h_i - \frac{M_{mix}}{M_i} c_p T\right)}{P\left(1 + \frac{v_x^2}{c_p T}\right) - \rho v_x^2} \tag{3.10a}$$

$$\frac{dT}{dx} = \frac{v_x^2}{\rho c_p}\frac{d\rho}{dx} + \frac{v_x^2}{c_p}\left(\frac{1}{A}\frac{dA}{dx}\right) - \frac{1}{v_x \rho c_p}\sum_{i=1}^{N} h_i \dot{\omega}_i M_i \tag{3.10b}$$

$$\frac{dm_i}{dx} = \frac{\dot{\omega}_i M_i}{\rho v_x} \tag{3.10c}$$

These equations were implemented using an explicit Runge-Kutta fourth-order method (RK4) method, but this requires very small steps to give accurate solutions for the conservation equations. An implicit RK4 would yield higher accuracy at a reasonable computational cost, and as such would have been implemented if this model was chosen [61].

The description of the model requires the reactions from fuel to soot precursor to be completed. There reactions are dependant on the fuel type, and while the Leung *et al.* model [53] included reaction steps for the combustion of C_1, C_2 and C_3 hydrocarbons, these are not sufficient for the range of fuels used in this work.

Many kinetics models have been established for different hydrocarbons and fuel surrogates[1], yet these still do not cover the possible variety of neither current existing fuels nor can they keep up with the new fuels emerging in the market. However, this does not mean that different fuels can not be modelled; the use of fuel surrogates[2] allows for the modelling of a wide variety of fuels with preexisting models for more extensively researched fuels.

This was considered to be the approach that might yield the most accurate results, but surrogate models were not found for the fuels this work intended to analyse. The formulation of a surrogate model requires both extensive knowledge on the fuel to be researched and chemical modelling expertise; the endeavor was deemed to be well outside of the scope of this work.

An alternative method was looked into - the use of a single step reaction that still distinguished between fuels. In references [54] and [63], the formation of acetylene was modeled as in reaction 3.11a, with a dependency on the fuel carbon number, m.

$$C_m H_n \xrightarrow{\dot{R}_{C_2H_2}} \frac{m}{2} C_2H_2 \tag{3.11a}$$

$$\dot{R}_{C_2H_2} = \frac{m}{2} k_{C_2H_2} [C_2H_2] \tag{3.11b}$$

The rate constant $k_{C_2H_2}$ takes different values in these works, but keeps the same activation temperature. Equation 3.12a represents the rates constant in reference [54], while equation 3.12b represents the rate constant in reference [63].

---

[1] Reference [62] provides an extensive database for diesel fuels and jet-fuels for use with the CHEMKIN environment, which is generally indicative of what is currently available for public use.

[2] A fuel surrogate is the mixture of two or more simple fuels, resulting in properties similar to those of the fuel they wish to emulate. The simple fuels picked are dependent on which properties the research is focused on, so that different surrogate mixtures can be used to describe the same fuel depending on the desired application [36].

$$k_{C_2H_2} = 10^{10} exp(-2.5 \times 10^4/T) \tag{3.12a}$$

$$k_{C_2H_2} = 2 \times 10^{8} exp(-2.5 \times 10^4/T) \tag{3.12b}$$

While there is not a mention of the exact data the rate constants were fit to in either reference, reference [63] states that the factor m is introduced explicitly to account for the difference in soot emissions brought on by wide variation in fuel carbon number, with mentioned values ranging from $m = 8$ to $m = 16$. Still, both models were explicitly made for diesel engines and carried out their studies solely for the tetradecane fuel ($m = 14$).

Additionally, research into the influence of fuel properties on soot had previously identified the hydrogen content of a fuel, and not the carbon number, as the key fuel property controlling its formation [2]. This was also typically reflected in empirical models used to simulate soot formation. Still, simulations were run with both rates and a third reaction fitted to data from reference [64] for n-decane ($m = 10$); the third reaction is shown in equation 3.13.

$$k_{C_2H_2} = 1.5 \times 10^{9} exp(-2.5 \times 10^4/T) \tag{3.13}$$

The model data was compared to experimental data from the Lycoming ALF 502 engine through the conversion of the soot mass to smoke number. For these tests, the Jet A-1 fuel ($m = 11$) from Appendix A was used. The only rate constant showing an acceptable relation between predicted and measured data was the reation fitted to n-decane, with the others either over or under-predicting the value by at least one order of magnitude.

When it came to differentiating between the fuels all rate constants failed. Reference [3] showed a measured decrease in soot particle number when using a HEFA C. blend in the range of 20 % to 50 %. Yet values predicted with this model showed an increase in emissions of up to 20 %.

This model was thus put to rest, being included only for the sake of completion and for possible later research into the topic. A future approach to this topic would require both deeper chemistry insight and a broader range of data.

3.0.2 Rizk and Mongia and GSP Models

The Rizk and Mongia model [52] is an empirical model used for the calculation of soot mass emissions which takes into account the soot formation and the soot oxidation. It is expressed according to equation 3.14. In this model the formation is associated with the primary zone and the oxidation is associated with the secondary zone, but the model itself is 0-D and calculated in a single step.

$$EI_{soot} = 0.0145 \frac{f_{pz} P_{03}^2}{f \dot{m}_3 T_{pz}} (18 - H\%)^{1.5} \left(1 - 0.00515 \frac{exp(0.001 T_{sz})}{f_{sz}}\right) \tag{3.14}$$

The Rizk and Mongia formulation [52] has served as a basis for several authors to construct their own variations of the model. The Gas turbine Simulation Program (GSP) model is an example of this; it takes the Rizk and Mongia relation for soot formation [52], and implements it with the Nagle-Strickland model for oxidation.

$$EI_{soot,formation} = 0.0145 \frac{f_{pz} P_{03}^2}{f \dot{m}_3 T_{pz}} (18 - H\%)^{1.5} \tag{3.15}$$

The Nagle-Strickland model [65] calculates the specific surface oxidation rate, ω_{oxi}, as a function of the temperature and oxygen partial pressure of the fuel-air mixture in the combustion chamber.

$$\omega_{oxi} = 12x\frac{k_A P_{O_2}}{1 + k_Z P_{O_2}} + k_B P_{O_2}(1 - x) \tag{3.16}$$

The terms used in the Nagle-Strickland model [65], equation 3.16, can be obtained from the following equations:

$$x = \frac{1}{1 + \frac{k_T}{P_{O_2} k_B}} \tag{3.17a}$$

$$k_A = 20e^{-15096.5/T} \tag{3.17b}$$

$$k_B = 4.46 \times 10^{-3} e^{-7648.89/T} \tag{3.17c}$$

$$k_T = 1.51 \times 10^{5} e^{-48812/T} \tag{3.17d}$$

$$k_Z = 21.3e^{2063.19/T} \tag{3.17e}$$

Both the Rizk and Mongia model [52] and the GSP model calculate only soot mass emissions. For the conversion to soot particles, spherical particles are assumed and a mean particle radius is attributed to these particles.

$$EI_N = \frac{EI_{soot}}{\rho_s \frac{4}{3}\pi r_p^3} \tag{3.18}$$

Current understanding of soot formation dynamics establishes that particle number variation is not proportional to particle mass variation, and that the mean soot particle radius varies with both engine power and the fuel used.

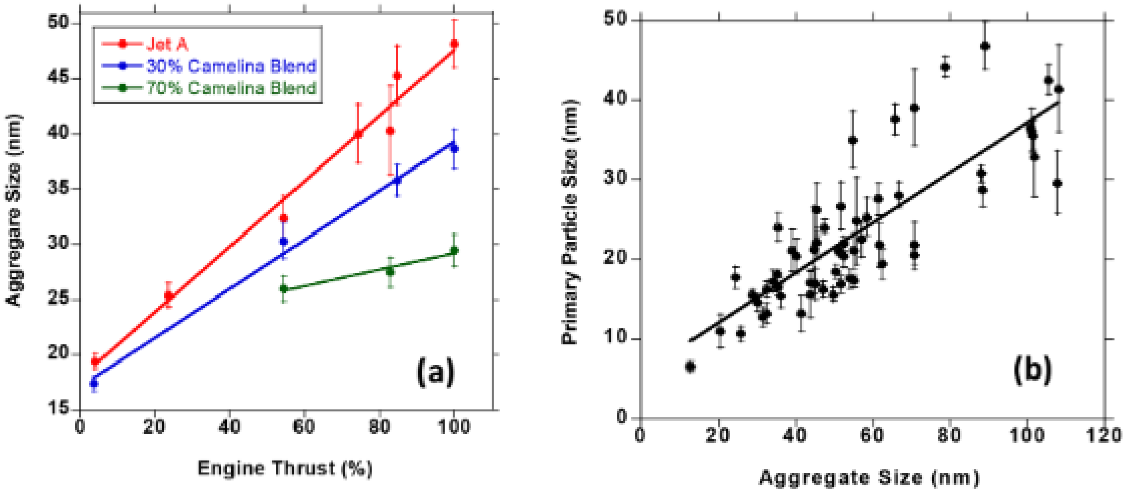

(a) Variation of soot aggregate size with engine thrust.

(b) Correlation between primary particle and aggregate particle size.

Figure 3.2: Analysis of soot samples from the exhaust of a J-85 turbojet burning Jet A fuel, a 30 % Camelina blend and a 70 % Camelina blend [66].

SAF blends with lower aromatics than typical Jet A-1 fuel have been shown to produce primary soot particles with a smaller mean radius. Figure 3.2a shows the variation in size for the soot particle aggregates in the exhaust of a J-85 turbojet burning Jet A fuel and different Camelina-based biofuel blends; there is a clear decrease in aggregate size for the blends, which becomes more pronounced with higher engine power. Figure 3.2b, from the same study, shows the correlation between the primary particle size and the aggregate size; this is not fuel dependent, since the correlation was not affected in the blends, but in conjunction with figure 3.2a shows an overall decrease in primary particle size when the Camelina blend was used.

Not enough data is available to establish a correlation between a fuel's composition and the aggregate and primary particle sizes ensuing from its combustion, so a mean radius is established for all fuels based on typical Jet A emissions. This could potentially lead to an underestimation of SAF soot particle emissions.

The GSP model requires the conversion to particle number to be done after formation and before oxidation. The specific surface oxidation rate is then applied to reduce the radius, and the final soot mass is calculated from the number of particles at formation and the oxidated mean particle radius. In this way, the particle number also directly influences the smoke number, which does not happen in the Rizk and Mongia model [52] where the conversion is done after both the formation and the oxidation of the soot.

The soot mass concentration was converted to smoke number, SN, using the International Civil Aviation Organization (ICAO) correlation, equation 3.19 [67].

$$c_s[mg/m^3] = 0.0694SN^{1.23357} \tag{3.19}$$

Figures 3.3a and 3.3b show the correlation between the smoke number measured for the Lycoming ALF 502 [68] and the smoke number predicted with the Rizk and Mongia [52] and the GSP model for similar conditions. Overall, the GSP model shows a better smoke number correlation, while the Rizk and Mongia model [52] overpredicts the smoke number. Nevertheless, both show acceptable correlations.

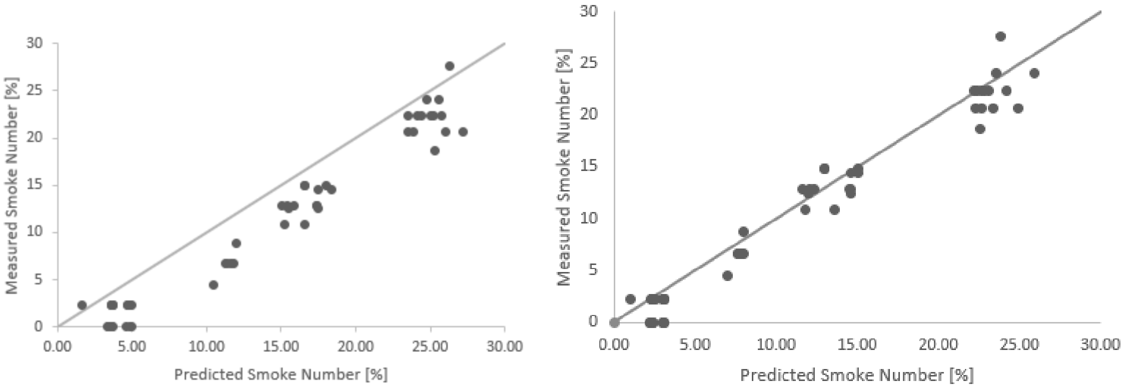

(a) Rizk and Mongia Model [52].

(b) GSP model [69].

Figure 3.3: Comparison between predicted and measured soot numbers based on data for the Lycoming ALF 502 engine.

Table 3.2 compares the Relative Differences (RDs) in particle emissions obtained with the Rizk and Mongia [52] and GSP [69] models with those measured in flight-tests; the comparison is done between a 50:50 blend of HEFA C. and a low-sulfur Jet A fuel, and a medium-sulfur Jet A fuel. The aircraft had four wing-mounted engines, with the exhaust plumes of the two inboard engines being measured; the data from both engines is presented, marked as Engine 1 and Engine 2.

The data is presented in relation to the thrust settings of the engine. It can be seen that measured data showed smaller RDs for high thrust settings, and higher RDs for low thrust settings. Both models seem insensitive to this variation, with the Rizk and Mongia model [52] showing only a small variation, and the GSP model [69] showing virtually no change.

It is important to note that the models do account for variations in the fuel flow, and that the particle emissions vary for the different thrust settings; it is the RDs between blend emissions and Jet A-1 emissions that show little variation.

This lack of sensitivity could be attributed to the use of a mean radius which does not vary with thrust settings. As seen in figure 3.2, the radius increases with engine thrust for all fuels, but the increase for Jet A is much steeper. For the same soot mass, this increased radius would wield a smaller particle number at higher power settings. This difference in particle size should thus attenuate the soot mass difference and yield smaller RDs in soot particle number emissions.

Setting	Engine	Measured	Rizk and Mongia Model	GSP Model
High	1	-23.67 %	-36.51 %	-35.04 %
	2	-21.60 %		
Medium	1	-34.81 %	-36.66 %	-35.04 %
	2	-44.49 %		
Low	1	-43.95 %	-36.85 %	-35.04 %
	2	-55.14 %		

Table 3.2: Measured RDs in particle emissions from flight-tests [3] between a 50:50 HEFA C. blend and a medium-sulfur Jet A fuel, and RDs predicted with the Rizk and Mongia Model [52] and the GSP Model [69] for the same fuels.

The Jet A fuel and the SAF blend used in the flight tests had their properties measured, and their values tabulated along with the associated uncertainty in these measurements. Simulations were run to see how these uncertainties affected the final results. Only the hydrogen percentage uncertainty of the fuels yielded a considerable variation in the results.

Table 3.3 shows the RDs for the predicted soot particle number emissions when varying the hydrogen percentage of the HEFA C. blend in its uncertainty range, ± 0.2 %.

The GSP model [69] shows a rather large variation in RDs for the high thrust setting. This is not shown for other settings, and it can not be validated from existing data. Taking this into consideration, despite the better agreement in measured soot number for the GSP model [69], the Rizk and Mongia model [52] was chosen to be used in conjunction with the contrail model in this work.

Setting	Hydrogen Percentage	Rizk and Mongia Model	GSP Model
High	14.9 %	-35.74 %	-21.12 %
	14.7 %	-36.51 %	-35.04 %
	14.5 %	-37.19 %	-46.43 %
Medium	14.9 %	-35.8 8%	-34.24 %
	14.7 %	-36.66 %	-35.04 %
	14.5 %	-37.33 %	-35.72 %
Low	14.9 %	-36.07 %	-34.24 %
	14.7 %	-36.85 %	-35.04 %
	14.5 %	-37.52 %	-35.73 %

Table 3.3: Predicted relative differences in particle number emissions for different HEFA C. Hydrogen percentages.

Chapter 4

Aircraft and Environment

4.1 Gas Model and Thermodynamic Relations

Throughout this work several different laws and thermodynamic relations are used repeatedly. This section seeks to compile them so as to avoid unneeded repetition and confusion.

For an ideal gas, the enthalpy variation is independent of pressure, varying only with temperature. This relation, refered to in this work simply as enthalpy equation, is expressed in equation 4.1, with h being the specific enthalpy, c_p the isobaric specific heat and $\Delta T = T_f - T_i$ the temperature variation.

$$\Delta h = \int_{T_i}^{T_f} c_p(T) dT \tag{4.1}$$

The entropy variation for a perfect gas can be expressed in its differential form as in equation 4.2a. If integrated, it results in equation 4.2b, where $\Delta P = P_f - P_i$ is the pressure variation.

$$ds = \frac{dh}{T} - R\frac{dP}{P} \tag{4.2a}$$

$$\Delta s = \int_{T_i}^{T_f} \frac{c_p(T)}{T} dT - Rln\frac{P_f}{P_i} \tag{4.2b}$$

For the purposes of this work, ϕ_s, defined in equation 4.3, will be referred to as entropy function.

$$\phi_s(T_f, T_i) = \frac{1}{R} \int_{T_i}^{T_f} \frac{c_p(T)}{T} dT \tag{4.3}$$

For an an isentropic process, where $\Delta s = 0$, equation 4.2b becomes equation 4.4.

$$ln\frac{P_f}{P_i} = \int_{T_i}^{T_f} \frac{c_p(T)}{T} dT \tag{4.4}$$

The above equations are valid for both total and static properties. Total and static enthalpies or temperatures can be related using equation 4.5.

$$h_0 = h + \frac{v^2}{2} \tag{4.5}$$

Since this work aims to model and compare the combustion of different fuels, there is a need to accurately compute the specific heat coefficient at constant volume, c_p, in a way that both accounts for temperature changes and for variations in fuel chemistry. For this purpose, equation 4.6 is used. The coefficients in this equation can be computed as detailed in Appendix B.

$$c_p(T) = A + BT + CT^2 + DT^3 + ET^4 \tag{4.6}$$

4.1.1 Evaporation Model

In this work, the combustion efficiency is defined for each fuel in relation to the reference fuel, Jet-A1. One of the parameters that allows for the distinction between fuels is the evaporation constant, λ_v, which is computed as shown in this section.

In a quasi-steady state, with the temperature of the fluid assumed to be constant with time, the variation of the diameter of a droplet can be expressed using the "D^2-Law", expressed in equation 4.7.

$$D(t)^2 = D_0(t)^2 - \lambda_v t \tag{4.7}$$

The evaporation constant is what controls the rate of the variation with time of the droplet diameter, and it is a fuel dependent parameter. It can be computed as in equation 4.8, making it a function of the transfer number, Q_n, the fuel liquid density, ρ_F, the gas specific heat, $c_{P,g}$, and the gas thermal condutivity, k_g.

$$\lambda_v = \frac{8ln(1+Q_n)}{\rho_F(T)\left[\frac{c_p}{k}\right]_g} \tag{4.8}$$

The fuel liquid density can be calculated as a function of temperature as seen in equation 4.9a, where the expansion coefficient C_{ex} is interpolated from available data [70]. The critical temperature, T_c, and the parameters using to calculate the normal boiling point temperature, T_{bn}, are obtained from table A for tabulated fuels, or computed as in Appendix D for blends.

$$\rho_F(T) = \rho_{60^oF}\left(1 - 1.8C_{ex}(T_{bn} - 288.6) - 0.09\left(\frac{T_{bn} - 288.6}{T_c - 288.6}\right)^2\right) \tag{4.9a}$$

$$T_{bn} = \frac{T_{b_{10\%}} + 2T_{b_{50\%}} + T_{b_{90\%}}}{4} \tag{4.9b}$$

Equation 4.10a expresses the assumption that in steady-state the mass transfer number, Q_M, which is used when evaporation rates are controlled by mass diffusion processes, and the heat transfer number, Q_T, which is used when they are controlled by heat transfer rates, are equal to each other.

$$Q_n = Q_M = Q_T \tag{4.10a}$$

$$Q_M = \frac{m_{F,d}}{1 - m_{F,d}} \tag{4.10b}$$

$$Q_T = \frac{c_{p,g}(T_\infty - T_d)}{L_v} \tag{4.10c}$$

In the equation for heat transfer number, equation 4.10c, T_∞ is the ambient temperature, T_d is the droplet surface temperature and L is the latent heat of fuel vaporization [30].

$$L_v[kJ/kg] = L_{v,bn}\left(\frac{T_c - T_d}{T_c - T_{bn}}\right)^{0.38} \tag{4.11a}$$

$$L_{v,bn}[kJ/kg] = (360 - 0.39T_{bn})\frac{\rho_{H_2O}(60^oF)}{\rho_F(T_{bn})} \tag{4.11b}$$

In equation 4.10b, $m_{F,d}$ is the mass fraction of fuel vapour near the droplet's surface, which is defined as in equation 4.12.

$$m_{F,d} = \left(1 + \left(\frac{P_\infty}{P_{F,d}} - 1\right)\frac{M_{air}}{M_F}\right) \tag{4.12}$$

The pressure of saturated fuel vapour near the surface droplets, $P_{F,d}$, can be calculated from the Clausius Clapeyron equation, equation 4.13a. The coefficients for this relation depend on a reference temperature defined as $P_{ref} = 101325$ Pa [70].

$$P_{F,d}[hPa] = exp\left(a_f - \frac{b_f}{T_d - 43}\right) \tag{4.13a}$$

$$a_f = log\left(P_{ref}[hPa]\right) + \frac{b_f}{T_{bn} - 43} \tag{4.13b}$$

$$b_f = \frac{(T_{bn} - 43)(T_c - 43)}{T_c - T_b} log\left(\frac{P_c}{P_{ref}}\right) \tag{4.13c}$$

The ambient pressure P_∞ is set as the critical pressure of the fuel or as the combustion chamber inlet pressure according to the combustion conditions shown in equation 4.14, which are defined in section 4.2.

$$P_\infty = \begin{cases} P_c & \text{if } T_{pz} \geq 2T_c \vee P_c \leq P_{03} \\ P_{03} & \text{otherwise} \end{cases} \tag{4.14}$$

4.2 Aircraft and Engine

The purpose of this work is to study the impact of SAF on contrail and contrail cirrus, which requires an engine capable of distinguishing between fuels in its combustion. To this effect, the 0-D engine model from reference [1] was implemented.

This model has been extensively documented and validated previously, and for this implementation only suffered minor alterations with the objective of reducing its computation time. While in its implementation in reference [1] the engine model was designed to run once per program run, in this work it runs once per route point; this vastly increased its run time, and brought to light some critical computational bottlenecks. Since resolving this issues did not alter the results or the modelling of the engine, this section will be brief and not go into the intricacies of the model at length.

The engine modelled is a two-spool turbofan of the same type as the Lycoming ALF 502 engine. In reference [1], design, off-design and a transient models were created and validated for this engine, but in this work only the design and off-design models will be used.

The model makes extensive use of component maps, which were obtained from GasTurb program and can be found in reference [1].

Throughout the model description, numbers are used to represent different stations in the engine. These numbers correspond to the points marked in figure 4.1.

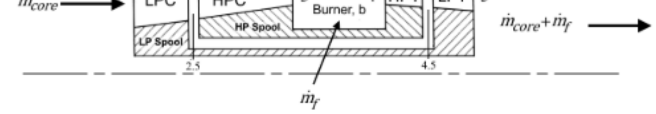

Figure 4.1: Schematics of a two-spool turbofan with station numbers [1].

4.2.1 Design Point Model

The design point of the engine was established for a Mach of 0.8 and an altitude of 10688m.

The diffuser is considered to be adiabatic, with a pressure loss that is obtained from a component map using the Mach number and corrected low pressure spool speed, which for the design point is $N_L = 1$.

The Low Pressure Compressor (LPC), High Pressure Compressor (HPC) and fan are defined by their respective total pressure ratios and polytropic efficiencies, which can be found in table 4.1.

	LPC	Fan	HPC
Pressure ratio $\left(\frac{P_{0f}}{P_{0i}}\right)$	2	1.7	6
Polytropic Efficiency (η^*)	0.88	0.86	0.88

Table 4.1: Pressure ratios and polytropic efficiencies of the LPC, fan and HPC.

The total pressures at the outlet of these components are obtained from their respective pressure ratios. The total temperatures at the outlet are obtained from equation 4.15, where η^*_{comp} is the polytropic efficiency of each compressor.

$$ln\frac{P_f}{P_i} = \eta^*_{comp}\phi_s \tag{4.15}$$

Off-design calculations require the efficiencies of each of these components. The efficiency for a compressor, η_{comp}, is defined as in equation 4.16, where $\varDelta h_s = h_{0f,s} - h_{0i}$ is the enthalpy variation for an isentropic process.

$$\eta_{comp} = \frac{h_{0f,s} - h_{0i}}{h_{0f} - h_{0i}} \tag{4.16}$$

For the design point, a Bypass Ratio (BPR) of 5.7 was established. The mass flow going into the core of the engine and the mass flow passing through the fan are calculated from equations 4.17a and 4.17b, with $\dot{m}$ being the mass flow at the engine inlet.

$$\dot{m}_{core} = \frac{\dot{m}}{1 + BPR} \tag{4.17a}$$

$$\dot{m}_{fan} = \frac{BPR \times \dot{m}}{1 + BPR} \tag{4.17b}$$

The combustion chamber at the design point is defined by its outlet stagnation temperature, $T_{04} = 1550K$, and the combustion efficiency for the Jet-A1 fuel, $\eta_{comb,ref} = 0.98$.

Since this study seeks to differentiate between fuels, this efficiency can not be used generally. Instead, the efficiency for each fuel is computed in relation to $\eta_{comb,ref}$ as seen in equation 4.18, where λ_v is the evaporation constant, σ_F is the fuel liquid surface tension, and μ_F is the fuel dynamic viscosity.

$$\eta_{comb} = 1 - (1 - \eta_{comb,ref})\frac{\lambda_{v,ref}}{\lambda_v}\sqrt{\frac{\sigma_F}{\sigma_{F,ref}}}\sqrt{\frac{\mu_F}{\mu_{F,ref}}} \tag{4.18}$$

The liquid tension for the chosen fuel and the reference fuel are computed for a reference temperature $T_{ref} = 298.15$ K according to equation 4.19a, where K_W is the Watson factor.

$$\sigma_F = \frac{0.6737\left(1 - \frac{T_{ref}}{T_c}\right)}{K_W} \tag{4.19a}$$

$$K_W = \frac{(1.8T_b)^{\frac{1}{3}}}{SG} \tag{4.19b}$$

The fuel-air ratio, f, is then computed iteratively from equation 4.20 and equation 4.18. The enthalpy values in equation 4.20 are obtained from the enthalpy function, equation 4.1.

$$\eta_{comb} = \frac{(1+f)h_{04} - h_{03}}{fQ} \tag{4.20}$$

To initiate the loop, the fuel-air ratio and the combustion efficiency are estimated using a simplified equation for the evaporation constant; this is further documented in reference [1].

From this point on, the core mass flow is no longer considered to be dry air, but is instead a mixture of dry air with fuel:

$$\dot{m}_4 = \dot{m}_{core}(1+f) \tag{4.21}$$

The total temperature at the outlet of each turbine is obtained through the work compability relation between the power it produces and the power the compressor requires. This relation is expressed in equation 4.22a, and the work of each turbine and the compressor its shaft connects to is expressed in equations 4.22b and 4.22c. The mechanical efficiency of the high speed shaft and the low speed shaft are considered to be the same, $\eta_m = \eta_{m_H} = \eta_{m_L} = 0.99$.

$$W_{comp} = W_{turb} \tag{4.22a}$$

$$\dot{W}_{comp} = \dot{m}_4 \left(h(T_{0f}) - h(T_{0i})\right) \tag{4.22b}$$

$$\dot{W}_{turb} = \eta_m \dot{m}_4 \left(h(T_{0i}) - h(T_{0f})\right) \tag{4.22c}$$

The outlet pressures of the turbines can be obtained from equation 4.23, where the polytropic efficiency is $\eta^*_{turb} = \eta^*_{HPT} = \eta^*_{LPT} = 0.89$.

$$ln \frac{P_{0f}}{P_{0i}} = \frac{1}{\eta^*_{turb}} \phi_s(T_{0f}, T_{0i}) \tag{4.23}$$

The efficiencies of each turbine are required for the off-design model. They are obtained from equation 4.24, where $\Delta h_s = h_{0i,s} - h_{0f}$ is the enthalpy variation for an isentropic process.

$$\eta_{turb} = \frac{h_{0i} - h_{0f}}{h_{0i} - h_{0f,s}} \tag{4.24}$$

The nozzles are defined by their pressure ratios at the design point. These are the same for the core and bypass nozzles, $\frac{P_{09}}{P_{05}} = \frac{P_{019}}{P_{013}} = 0.98$. The total pressure at the bypass and nozzle outlets are computed from these.

The critical temperatures at the outlets, $T_{9,c}$ and $T_{19,c}$, are calculated from the relationship between the TAS and the Mach number, equation 4.25, and the relationship between total and static enthalpy, equatio 4.5. The critical conditions are the conditions at which the engine outlet is sonic, so these are calculated for $Ma = 1$.

$$v = Ma\sqrt{\gamma RT} \tag{4.25}$$

The static critical pressures, $P_{9,c}$ and $P_{19,c}$, are be obtained from the isentropic relation, equation 4.4.

If the critical pressure at the nozzle outlet is higher than the stagnation pressure at its inlet, that is, $P_{9,c} > P_E$, the core nozzle is choked; in this case, the exit conditions are sonic, which leads to $P_9 = P_{9,c}$ and $T_9 = T_{9,c}$. Otherwise, the conditions are subsonic, leading to $P_9 = P_E$ and an exit static temperature which can be calculated from the isentropic relation, equation 4.4.

As stated in section 2, the propulsion efficiency of the aircraft is an important factor which influences whether contrails are formed or not. To compute it the thrust is necessary.

The thrust can be obtained from the sum of the bypass thrust and the core thrust as shown in equation 4.26a, where the outlet velocity is calculated from the relation between total enthalpy and stagnation enthalpy, equation 4.5.

$$F = F_{fan} + F_{core} \tag{4.26a}$$

$$F = \dot{m}_{fan}(v_{19} - TAS) + A_{19}(P_{19} - P_E) \tag{4.26b}$$

$$F = \dot{m}_{core}((1+f)v_9 - TAS) + A_9(P_9 - P_E) \tag{4.26c}$$

The nozzle outlet cross section areas, a required input for the Off-Design Model, are obtained from equation 4.27.

$$A_f = \frac{\dot{m}RT}{Pv} \tag{4.27}$$

4.2.2 Off-Design Model

The Off-Design model takes as inputs the ambient conditions, the TAS, the low-pressure relative spool speed ($N_L = 0.95$ for cruise conditions), and set of inputs, listed on table 4.2, which runs with a loop are corrected at each iteration. The errors being fed into this loop are included in this section and summarized in a table at the end.

Variable	Description
N_H	High-pressure relative spool speed
T_{04}	Temperature at combustion chamber outlet
BPR	Bypass ratio
β_{LPC}	Auxiliary map coordinate for the LPC
β_{HPC}	Auxiliary map coordinate for the HPC
β_{HPT}	Auxiliary map coordinate for the HPT
β_{LPT}	Auxiliary map coordinate for the LPT

Table 4.2: Iteration variables for the off-design engine model.

The off-design model calculates the conditions at each station through the use of component maps. These component have the corrected spool speed, N_{corr}, of the component as an input. It can be computed from equation 4.28, where T_{0i} is the total pressure at the component inlet for off-design conditions, and $T_{0i,des}$ is the total pressure at the component inlet for the design point. N_x can take the value of N_L or N_H depending on the component.

$$N_{x,corr} = N_x \sqrt{T_{0i,des} T_{0i}} \tag{4.28}$$

With the exception of the diffuser component map, the maps for the different components compute their pressure ratio, efficiency, and corrected mass flow at inlet, $\dot{m}_{corr,map}$. A corrected mass flow, $\dot{m}_{corr}$, can also be computed from equation 4.29. Differences between these are fed back into the loop as errors.

$$\dot{m}_i = \dot{m}_{i_{corr}} \frac{\delta_i}{\sqrt{\theta_i}} \tag{4.29}$$

In equation 4.29, θ_i is the non-dimensional total temperature, obtained from equation 4.30a, and δ_i is the non-dimensional total pressure, δ_i, obtained from equation 4.30b. $T_{ref} = 288.15$ K and $P_{ref} = 101325$ Pa correspond to the temperature and pressure at sea level conditions in the ISA, and $R_{ref} = 287.05$ J/(kgK) corresponds to the dry air gas constant for these conditions.

$$\theta_i = \frac{T_{0i} R_i}{T_{ref} R_{ref}} \tag{4.30a}$$

$$\delta_i = \frac{P_{0i}}{P_{ref}} \tag{4.30b}$$

The conditions for the fan and HPC are obtained from their component maps. For the LPC, the pressure ratio and efficiency are given in relation to those of the fan according to equations 4.31a and 4.31b.

$$\frac{P_{02.5}}{P_{02}} = 1 + \frac{\left(\frac{P_{09}}{P_{02}} - 1\right)\left(\left[\frac{P_{02.5}}{P_{02}}\right]_{des} - 1\right)}{\left[\frac{P_{09}}{P_{02}}\right]_{des} - 1} \tag{4.31a}$$

$$\eta_{LPC} = \eta_{fan} \frac{\eta_{LPC,des}}{\eta_{fan,des}} \tag{4.31b}$$

The total temperatures at the outlets of the fan, the LPC and the HPC are calculated using equation 4.16. The difference between the calculated corrected mass flow and the map corrected mass flow for the HPC inlet is the first error, ”Error 1”.

The off-design efficiency of the combustion chamber is calculated in relation to its design point efficiency as seen in equation 4.32a, where $\varOmega$ is the combustion chamber loading.

$$log(1 - \eta_{comb}) = log(1 - \eta_{comb,des}) + 1.6 log\left(\frac{\varOmega}{\varOmega_{des}}\right) \tag{4.32a}$$

$$\varOmega = \frac{\dot{m}_3}{P_{03}^{1.8} e^{\frac{T_{03}}{300}}} \tag{4.32b}$$

The pressure ratio in the combustion chamber is also computed in relation to its design point counterpart:

$$\frac{P_{04}}{P_{03}} = \left(\frac{P_{04}}{P_{03}}\right)_{des} \left(\frac{\dot{m}_{3_{corr}}}{\dot{m}_{3_{corr,des}}}\right)^2 \tag{4.33}$$

The fuel-air ratio and mass flow at combustion chamber outlet using equations 4.20 and 4.21, respectively.

The conditions for the High Pressure Turbine (HPT) and the Low Pressure Turbine (LPT) are obtained from their components maps, with the total temperatures at their outlets being computed using equation 4.24.

”Error 2” and ”Error 3” are obtained from the discrepancy between the corrected mass flows obtained from the HPT and LPT maps and the corrected mass flows calculated with equation 4.29.

The work compability is also verified in the turbines using Error 4 and Error 5, as shown in equations 4.34a and 4.34b.

$$Error_4 = \dot{W}_{HPT} - \dot{W}_{HPC} \tag{4.34a}$$

$$Error_5 = \dot{W}_{LPT} - \dot{W}_{LPC} - \dot{W}_{fan} \tag{4.34b}$$

The nozzle outlet conditions are computed similarly to the design point, but the pressure losses are calculated as in equations 4.35a and 4.35b.

$$\frac{P_{09}}{P_{05}} = \left(\frac{P_{09}}{P_{05}}\right)_{des}\left(\frac{\dot{m}_{5_{corr}}}{\dot{m}_{5_{corr,des}}}\right)^2 \tag{4.35a}$$

$$\frac{P_{019}}{P_{013}} = \left(\frac{P_{019}}{P_{013}}\right)_{des}\left(\frac{\dot{m}_{13_{corr}}}{\dot{m}_{13_{corr,des}}}\right)^2 \tag{4.35b}$$

At last, we can compute the thrust, outlet velocity and area as in the design point. At this point, the outlet area might give a different result as the one calculated for the design point; since the engine does not have a variable nozzle, this discrepancy is put back into the loop as an error.

All the errors driving the loop are summarized in table 4.3.

	Expression
Error 1	$\dot{m}_{2.5_{corr,map}} - \dot{m}_{2.5}\frac{\sqrt{\theta_{2.5}}}{\delta_{2.5}}$
Error 2	$\dot{m}_{4_{corr,map}} - \dot{m}_{4}\frac{\sqrt{\theta_{4}}}{\delta_{4}}$
Error 3	$\dot{m}_{4.5_{corr,map}} - \dot{m}_{4.5}\frac{\sqrt{\theta_{4.5}}}{\delta_{4.5}}$
Error 4	$\dot{W}_{HPT} - \dot{W}_{HPC}$
Error 5	$\dot{W}_{LPT} - \dot{W}_{LPC} - \dot{W}_{fan}$
Error 6	$A_9 - A_{9,des}$
Error 7	$A_9 - A_{9,des}$

Table 4.3: Feedback errors for the off-design model iteration.

4.2.3 Combustion Chamber Dimensions

The 0-D combustion chamber description from reference [1] was not sufficient for the purposes of this work. Soot calculations for the studied models required information on the combustion chamber's area and length; since this information was not publicly available for the Lycoming ALF 502 or others of this type, the dimensions were estimated [30].

The combustion chamber casing cross-sectional area is estimated using equation 4.36.

$$A_{ref} = \sqrt{\frac{R_{air}}{2}\left(\frac{\dot{m}_3 T_{03}^{0.5}}{P_{03}}\right)^2 \frac{\Delta P_{03-04}}{q_{ref}}\left(\frac{\Delta P_{03-04}}{P_{03}}\right)} \tag{4.36}$$

The Lycoming ALF 502 has an annular combustion chamber. Typical pressure loss values for this type of combustion chamber were used in equation 4.36 and are listed in table 4.4.

Overall pressure loss	$\left(\frac{\Delta P_{03-04}}{P_{03}}\right)$	0.06
Pressure-loss factor	$\frac{\Delta P_{03-04}}{q_{ref}}$	20
Combustion Reference Velocity Term	$\frac{m_3 T_3^{0.5}}{A_{ref} P_{03}}$	0.0046
Ratio of liner cross-sectional area to casing cross-sectional area	$k_{L,opt}$	0.65

Table 4.4: Optimal pressure loss and ratio of line to case cross-sectional area for an annular combustion chamber [30][71].

The lining area is obtained from A_{ref} and the ratio of liner cross-sectional area to case cross-sectional area, k_L. The optimal value for k_L, according to reference [71], can be found in table 4.4, but a value of $k_L = 0.52$ was used so as to have a design point primary zone residence time of 4ms as established in reference [1].

$$A_L = k_L A_{ref} \tag{4.37a}$$

$$D_L = \sqrt{\frac{4}{\pi} A_L} \tag{4.37b}$$

For a circular cross-sectional area, the liner diameter, D_L, can be obtained from equation 4.37b.

The lengths of the primary zone, L_{pz}, secondary zone, L_{sz}, and dilution zone, L_{dz}, are calculated from the relations 4.38a, 4.38b and 4.38c, respectively [30]. The dilution zone length is a function of the pattern factor, which is here taken to be $PF = 25$, in line with typical annular combustion chamber values [71].

$$L_{pz} = \frac{3}{4} D_L \tag{4.38a}$$

$$L_{sz} = \frac{1}{2} D_L \tag{4.38b}$$

$$L_{dz} = D_L \left(3.83 - 11.83PF + 13.4PF^2\right) \tag{4.38c}$$

4.3 Ambient Data

The contrail model presented in chapter 2 had many equations which relied heavily on local environment parameters. For these to provide viable results these parameters must be realistic.

To simulate a realistic atmosphere, the data for several local atmospheric parameters was obtained from the ERA-20CM model ensemble, provided by the European Centre for Medium-Range Weather Forecasts (ECMWF). The ERA-20CM project gathers together an ensemble of ten atmospheric model integrations made for the years 1899-2010; from these, the data selected for this model corresponded to that obtained in 2010 [72].

The values obtained for this model were the northward and eastward winds, V and U, the pressure change rate, ω, the ambient temperature, T, and the ambient relative humidity, U_{amb}. The data was made available as the mean monthly values for different pressure levels, starting at 1000 mbar and ending at 1 mbar. For each parameter, the final values used in the model were an average of the values in all ten assembles and in all twelve months of 2010.

As mentioned in chapter 1, there are certain regions in the globe where the formation of contrails is more likely than others. An advantage of this ensemble is that it provides data for different set latitudes and longitudes encompassing the whole globe. Together with the set pressure levels, this allows the atmosphere to be modeled in 3D space and accounts for the variations in these parameters in different regions of the globe.

For each point of the airplane route, and then for each time step of the contrail lifetime, the local environment parameters are interpolated in 3D space, (x, y, P), from the provided data.

The routes used in the model are defined by the longitude, latitude and flight level at each route point. Different routes were selected from the Real World Flightplan Database (RWFD) database and are included with visual representation in Appendix C [73]. Between each set point in the route, additional points were added to obtain shorter, identically spaced segments.

For route point calculations, the flight level altitude is used to obtain the ambient pressure using the ISA equations, where z is the altitude in meters:

$$P_E = \begin{cases} 101325\left(1 - \frac{0.0065z}{288.15}\right)^{5.25588} & \text{for} z \leq 11000 \\ 22632e^{-0.000157688(z-11000)} & \text{for} z > 11000 \end{cases} \tag{4.39}$$

The ambient temperature could also be obtained using the ISA equations, but a more realistic temperature variation with longitude and latitude was required to compute the local Brunt-Väisälä frequency with sufficient accuracy; the ambient temperature was thus obtained from the ERA-20CM model. The density is calculated using the ideal gas law, equation 4.40.

$$\rho = \frac{P}{R_{air}T} \tag{4.40}$$

The dynamic viscosity of air, used in equations 2.48 and 2.50a, is obtained through Sutherland's law, equation 4.41. In this equation, the reference temperature and reference dynamic viscosity are, respectively, $T_{ref} = 273.15$ K and $\mu_{ref} = 1.716 \times 10^{-5}$ Pa/s, and Sutherland's constant is $Su = 110.4$ K [74].

$$\mu_{air} = \mu_{ref} \frac{T_{air}}{T_{ref}}^{\frac{3}{2}} \frac{T_{ref} + Su}{T_{air} + Su} \tag{4.41}$$

Chapter 5

Results

In this chapter results relating to the particle emissions and contrail properties will be shown for blends and pure SAF.

Several routes were picked around the globe to be analysed for the different fuels; these are listed in table 5.1 and visually presented in table C. The routes over Central to Western Europe, over Eastern Europe and over North America had contrails surviving long past the wake vortex phase, while contrails in other routes[1] survived through roughly wake vortex times which, due to its parametric study, made it so there was little variation. While the first set of routes will be used for analysis of all parameters, the second set will only be included in contrail formation frequency analysis.

Origin Country	Airport ICAO Code	Destination Country	Airport ICAO Code
Germany	EDDP	Spain	LEBL
Norway	ENGM	Czech Republic	LKMT
Colombia	SKBO	Ecuador	SEQM
Saudi Arabia	OEJN	Bahrain	OBBI
Taiwan	RCTP	Japan	RJFF
Canada	CYUL	Canada	CYGW
New Zealand	NZAA	New Zealand	NZCH
South Africa	FAOR	South Africa	FACT

Table 5.1: Routes analysed in this work.

Routes with contrails with longer lifetimes coincided with locations with high persistent contrail coverage; this does not signify that long-lasting contrail would not occur in other analysed areas. The atmosphere is modelled using average yearly values, making this more indicative of the general trends of certain locations.

Figure 5.1 shows a route over Northern and Central Europe, as well as the contrails emitted by burning Jet A-1 and by burning pure GTL. While differences in contrail formation frequency and contrail lifetime are not clearly visible due to the figure resolution, the differences in optical depth are quite distinct. By comparing the contrails formed in the lower flight segment to others, it can be seen that the optical depth decreases faster in some locations than others. Depending on the location, the optical depth decrease for GTL is also more or less pronounced to that of the Jet A-1 contrails. The optical depth is heavily dependant on local ambient conditions, and the same can be said for the other contrail parameters analysed.

Most results will be shown in box plots to account for their high deviation. Figure 5.2 shows what a typical box plot marker looks like; the line in the middle of the box represents the median value, while

---

[1] Other routes included locations over New Zealand, East Asia, South Africa and North Africa.

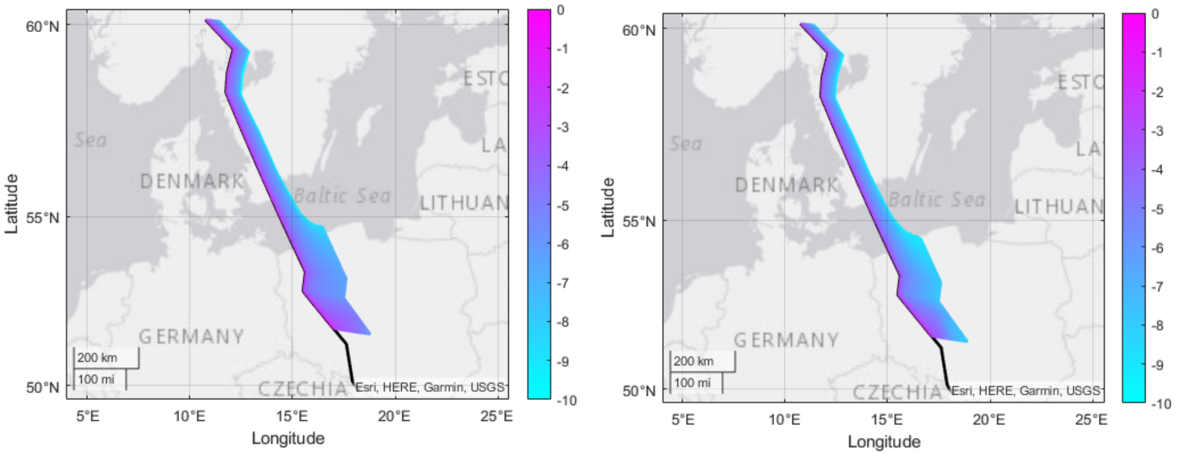
60°N
55°N
50°N
Latitude
5°E
10°E
15°E
20°E
25°E
Longitude
DENMARK
Baltic Sea
GERMANY
CZECHIA
LITHUAN
ESTO
LA
Sea
200 km
100 mi
Esri, HERE, Garmin, USGS
0
-1
-2
-3
-4
-5
-6
-7
-8
-9
-10

(a) Jet A-1 contrails.

(b) Pure GTL contrails.

Figure 5.1: Geographical plot of the contrails emitted for a route over Northern and Central Europe. Contrails are plotted for their entire lifetime. Colours represent the logarithm of the optical depth at the contrail trajectory points.

the whisker ends represent the minimum and maximum values, excluding outliers. 50 % of the results fall in the interquartile range, with 25 % of the results falling below the lower quartile and 75 % below the upper quartile. The whiskers extend to a maximum of 1.5x the value of the quartiles, with any values beyond that being considered outliers and represented as individual markers in the plot. Additionally, a cross marker will be used to represent the mean values of the results.

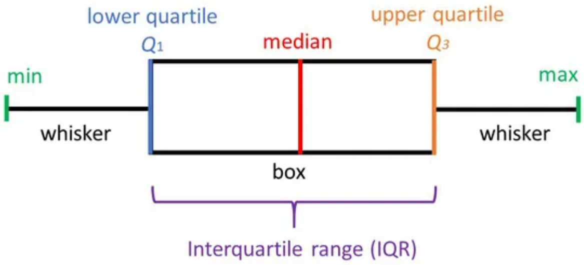
lower quartile
Q1
median
upper quartile
Q3
min
max
whisker
whisker
box
Interquartile range (IQR)

Figure 5.2: Box plot marker [75].

Results are almost always presented as the RD between the chosen fuel and the reference fuel, Jet A-1. Particle results are instead presented as the Mean Relative Difference (MRD) which is calculated as seen in equation 5.1b, where Δx_i is the RD at route point i and n is the total number of points in the route.

$$\Delta x_i = \frac{x_i - x_{ref,i}}{x_{ref,i}} \tag{5.1a}$$

$$MRD = \frac{1}{n}\sum_{i=1}^{n} \Delta x_i \tag{5.1b}$$

The Standard Deviation of Relative Differences (SDRD) is a measure of the dispersion in a set of values, and it can be calculated according to equation 5.2. Since the use of box plots makes the dispersion in values clear, plots of the SDRD were considered redundant and are not included; the SDRD is still mentioned when considered pertinent.

$$SDRD = \left(\sum_{i=1}^{n} \frac{(\Delta x_i - MRD_i)^2}{n-1} \right)^{1/2} \tag{5.2}$$

5.1 Formation Frequency

Figure 5.3 shows the RDs in water vapour emissions and net heat of combustion for the different SAF. These are presented to contextualize the contrail formation frequency results.

The chosen SAF each have a higher net heat of combustion than the reference fuel, Jet A-1, but with RDs smaller than 3 %. The Catalytic Hydrothermolysis Jet fuel (CHJ), the fuel with the closest properties to Jet A-1, presents a difference of only 0.23 %.

The water vapour emission indices of all SAF, except for CHJ, are also higher than those of the reference fuel, with a maximum RD of 12.47 % being found for the GTL fuel. CHJ, the only fuel with lower water vapour emissions than Jet A-1, presents a difference of –0.50 %.

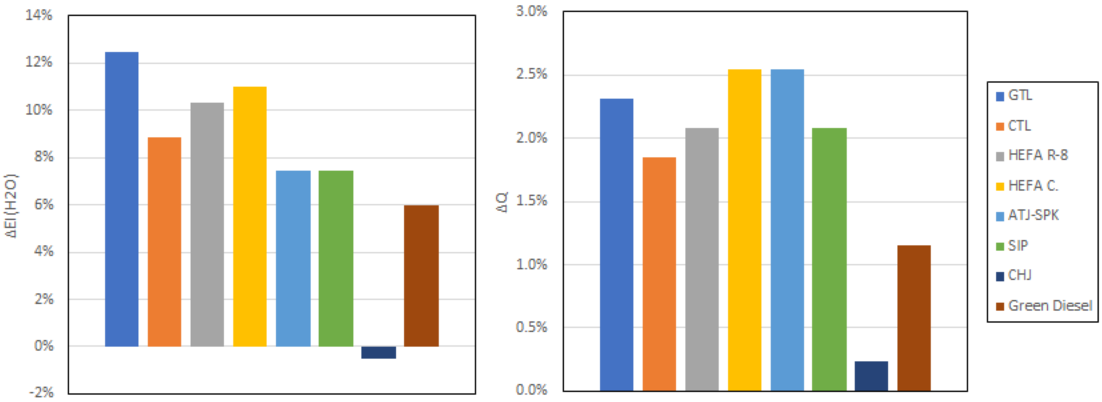

(a) Water vapour emissions.

(b) Neat heat of combustion.

Figure 5.3: RDs in water vapour emissions and neat heat of combustion for pure SAF.

The values for blends, shown in figure 5.4, follow the same trend as those for pure SAF, but with less marked differences. As stated in chapter 1, all blends have a SAF ratio of 50 % except for SIP which is mixed in at 10 %; this is the reason for the much smaller RDs found for the SIP blend when compared to pure SIP.

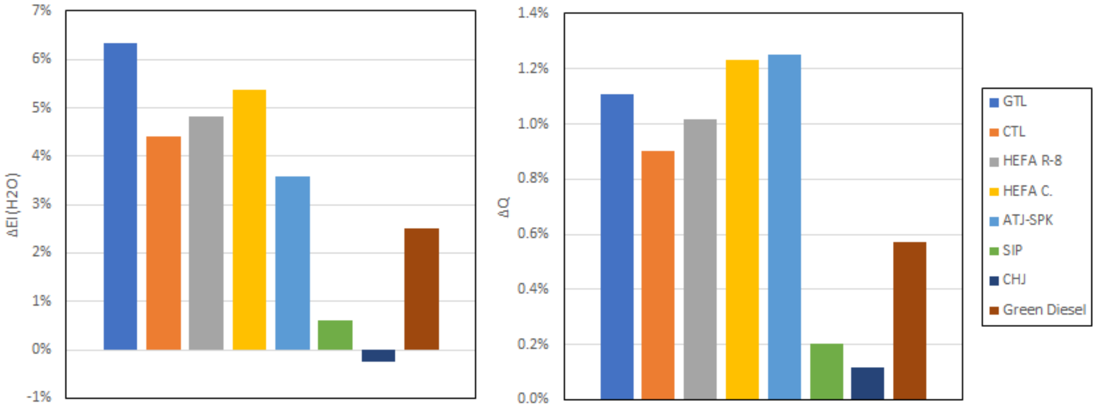

(a) Water vapour emissions.

(b) Neat heat of combustion.

Figure 5.4: RDs in water vapour emissions and neat heat of combustion for SAF blends.

Figure 5.5 shows the RDs in propulsive efficiency for the different SAF and SAF blends. The use GTL, CTL, HEFA C. and CHJ provides a small increase in propulsive efficiency, while burning the other fuels results in a small decrease. These values remain within 3 % of the Jet A-1 propulsion efficiency for pure SAF, and within 1 % for the blends.

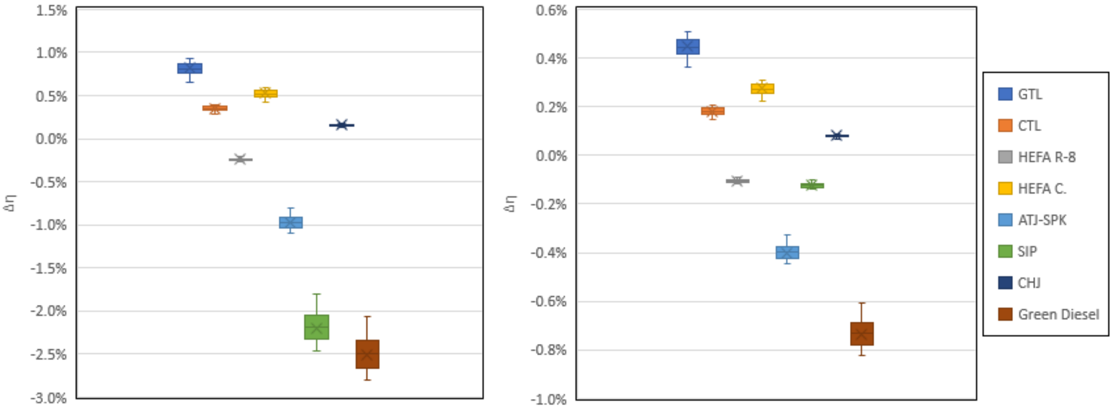

(a) Pure SAF. (b) SAF blends.

Figure 5.5: RDs in propulsive efficiency for SAF and SAF blends.

An increase in contrail formation frequency was expected due to the increase in water vapour emissions typical of SAF combustion, and it was indeed found. The increase in the net heat of combustion, which could hinder this frequency increase, is far outshined by the differences in water vapour emissions. The decrease in propulsive efficiency experienced by some fuels (or increase in propulsive efficiency for the CHJ) does not alter the trend set by the water vapour emissions either.

The increase in contrail formation frequency happened right behind and after Jet A-1 contrail formation areas; that is to say, in segments[2] where contrails formed for all fuels, contrails were formed for most SAF slightly earlier (with contrails forming for CHJ slightly later).

There were no contrails formed for SAF outside of these conditions. In routes where contrails were not formed for Jet A-1, they were also not formed for the other fuels, and there were no isolated segments of contrails formed for SAF only. In other words, this increase in contrail formation frequency resulted in slightly longer contrails, and not in new separate contrails.

This results in an increase in frequency of under 1 % for the different fuels. This is better represented by the differences in the contrail formation threshold temperature.

Figure 5.6 represents the absolute differences in threshold temperature for pure SAF and SAF blends. As stated in chapter 2, contrails form when the ambient temperature is below the calculated threshold temperature for that location. As can be seen from the plots, the contrails for the different SAF will form at temperatures of $\sim$1 K or less from each other. While it is not impossible for isolated segments of SAF contrails to exist, the small difference in temperature explains why the frequency increase resulted only in longer contrails; it is unlikely for aircraft to reach SAF threshold temperatures without crossing to a degree under.

Comparing the values for ATJ-SPK and SIP in figure 5.6a, it can be seen that while water vapour emissions control the trend, the differences in the net heat of combustion of the fuels do hold an observable influence over the formation frequency. Despite the similar water vapour emission indices between these fuels, SIP has a lower net heat of combustion which results in slightly higher threshold temperatures.

---

[2] 'Segment' here refers to consecutive route points through which contrails formed continuously.

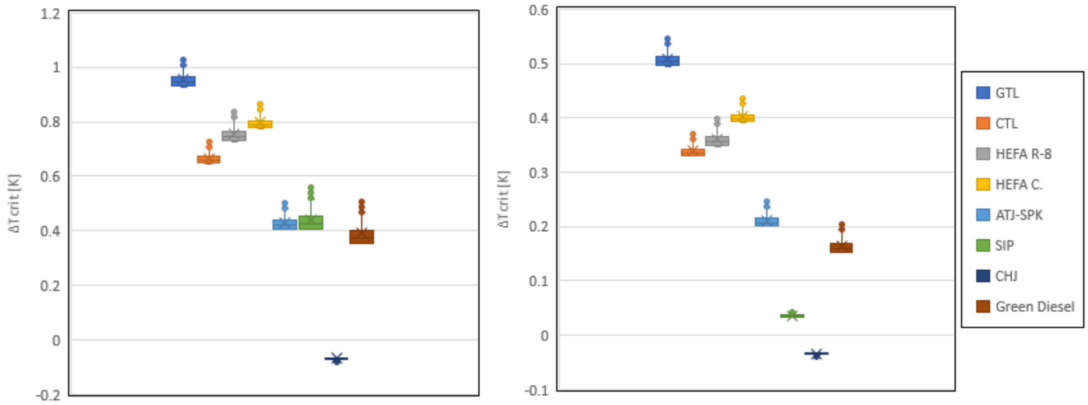

(a) Pure SAF.

(b) SAF blends.

Figure 5.6: Absolute differences in threshold temperature for SAF and SAF blends.

5.2 Lifetime

As discussed in chapter 3, the model does not seem to accurately portray variations in power level. Due to this, the data analysis for particle number emissions was done only for standard cruise conditions without an analysis of the power component. While the TAS varied slightly depending on the route, the low-pressure spool speed was kept at $N_L = 0.95$. This resulted in SDRDs very close to 0 % for all fuels, and Interquartile Range (IQR) values in the range of –0.20 %; the RDs in particle number emissions are thus represented in a column plot and not a box plot.

While the RDs for particle number emissions show little deviation from the mean, this does not signify that particle number emissions themselves are constant throughout the different route points. Standard deviations in particle number emissions differ between fuels, with the smallest value being of 22.0 % for GTL and the highest value being of 22.75 % for Green Diesel.

The RDs for particle number emissions are represented as their MRD in figure 5.7. All SAF, except for CHJ, show a decrease in particle emissions, with CHJ having an increase of 4.65 % when burnt pure, and of 2.12% when burnt in a blend.

The biggest decrease for pure SAF is found for GTL, which has a MRD of –78.07 %, while the lowest corresponds to Green Diesel, with a MRD of –44.95 %. GTL also presents the biggest decrease when burnt in a blend, with a MRD of –49.58 %, while lowest corresponds to SIP at an MRD of –5.79 %, due to the low ratio of SIP in the blend.

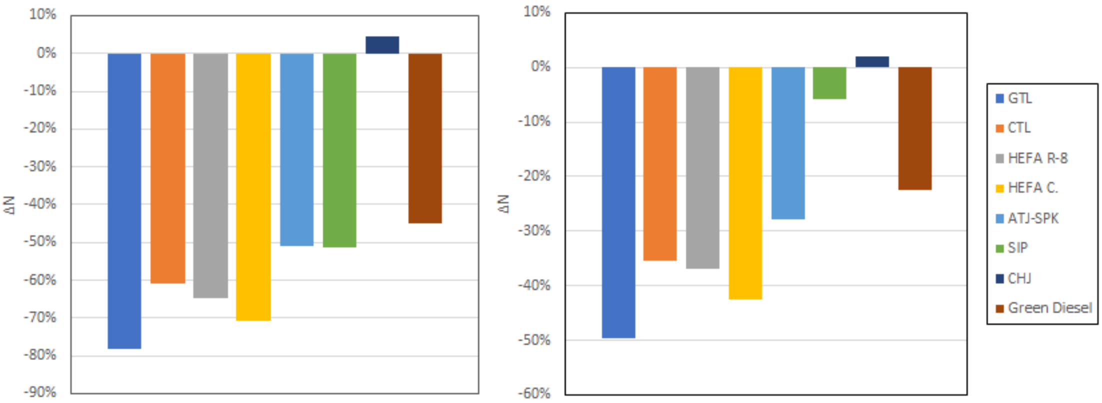

(a) Pure SAF.

(b) Blends.

Figure 5.7: RDs in particle number emissions.

The main fuel-dependent factors influencing contrail properties are the water vapour emissions and the particle number emissions. All fuels show the same trend - an increase in water vapour emissions and decrease in particle number emissions - except for CHJ. To avoid redundancy, when SAF behaviour is described in this chapter it will be referring to all SAF with the exception of CHJ, with the implication that CHJ is displaying the opposite behaviour.

The contrail lifetime analysis is split into three parts due to the large deviation in values found between these: contrails with lifetimes of up to 30 minutes, contrails with lifetimes ranging from 30 minutes to 2 hours, and contrails with lifetimes greater than 2 hours.

The general trend was that the higher the reference contrail lifetime was, the higher the decrease in lifetime for SAF contrails was, with young contrails experiencing instead an increase in lifetime. However, this was not a direct correlation. The lifetime of each contrail is heavily dependent on the surrounding environment during its lifetime, which leads to a large deviation in the RDs for reference contrails with very similar lifetimes.

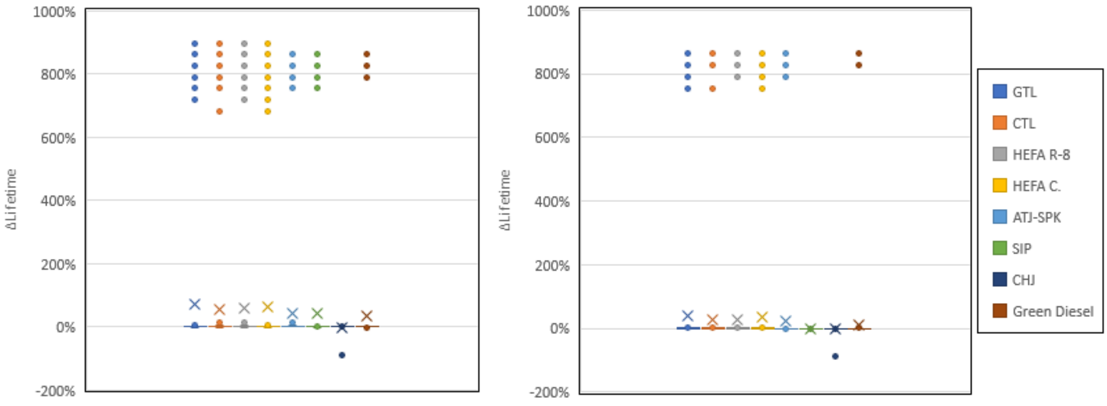

(a) Pure SAF. (b) Blends.

Figure 5.8: RDs in lifetime for reference contrails aged 30 minutes or less.

Figure 5.8 shows the RD in lifetime for the cases where the reference contrail, that is, the contrail formed when Jet A-1 was burnt, had a lifetime of 30 minutes or less. For this time range, contrails almost always ended due to their IWC reaching zero; this was not the case for longer lasting contrails, which typically ended due to reaching very low optical depths despite still having a positive IWC. The key fuel-dependent factor controlling their lifetimes for this time range is thus considered to be the water vapour emissions index.

Most contrails in this time range have RDs in lifetime close to 0 %, but the MRDs are dragged up due to the very high outliers. These outliers were all present in the same short segment, and seem to be the result of SAF contrails reaching higher relative humidity areas shortly after the reference contrail lost its IWC. The plot for the blends presents less outlier points, with the 10 % SIP blend showing no outlier points in the 800 % at all; this is due to the SAF contrails evaporating before the higher relative humidity areas as well.

There is a high deviation in results for this time range even within the same few seconds; the highest RDs were found for reference contrails aged around 46 seconds, but other contrails of around the same age led to RDs of close to 0 %.

At around the 20 minute mark, the lifetime of SAF contrails starts decreasing instead of increasing in relation to that of the reference contrails; this transition zone differs between the different fuels. Small decreases for SAF contrail lifetime were found as early as 14 minutes for GTL and HEFA C., at around 23 minutes for HEFA R-8, SIP and Green Diesel, and at around 27 minutes for CTL and ATJ-SPK. Small increases for SAF contrail lifetime were found as late as 27 minutes for GTL, 20 minutes for CTL, HEFA

R-8, HEFA C. and ATJ-SPK, and 13 minutes for SIP and Green Diesel.

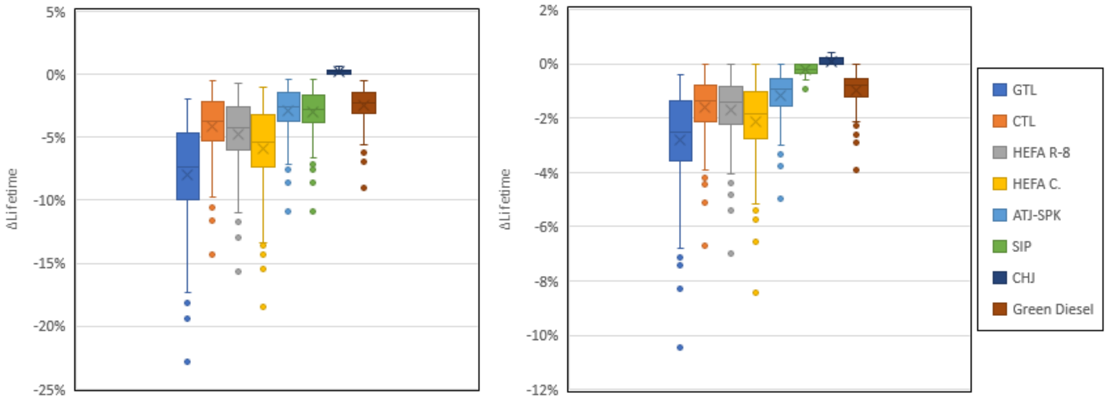

(a) Pure SAF.

(b) Blends.

Figure 5.9: RDs in lifetime for reference contrails with lifetimes ranging from 30 minutes to 2 hours.

Figure 5.9 shows the RDs in lifetime for reference contrails with lifetimes up to 2 hours. From the 27 minute mark, when the last lifetime increase was found, all SAF contrails ended earlier than the reference contrails at the same point. Results in this range still show some dispersion for reference contrails lifetimes that are close to each other, but there is a clear trend of higher reference lifetimes yielding higher RDs. The outliers in this range are all found for 80 minutes or more, but, for this same range, values inside the IQR were still found.

The biggest decreases were found once more for GTL, with a MRD of −8.02 % when burnt pure and of −2.80 % when burnt in a blend. The lowest being was for pure Green Diesel, with a MRD of −2.52 %, and for the SIP blend, with MRD of −0.20 %.

It is important to note that while RDs pale in comparison to those found for the previous time range, absolute differences are not that far apart. The outliers in figure 5.8, with increases of over 800 %, correspond to absolute differences of a bit less than 4 minutes, while mean values for this range correspond to absolute differences of around 1 minute for the SIP blend to 5 minutes for GTL.

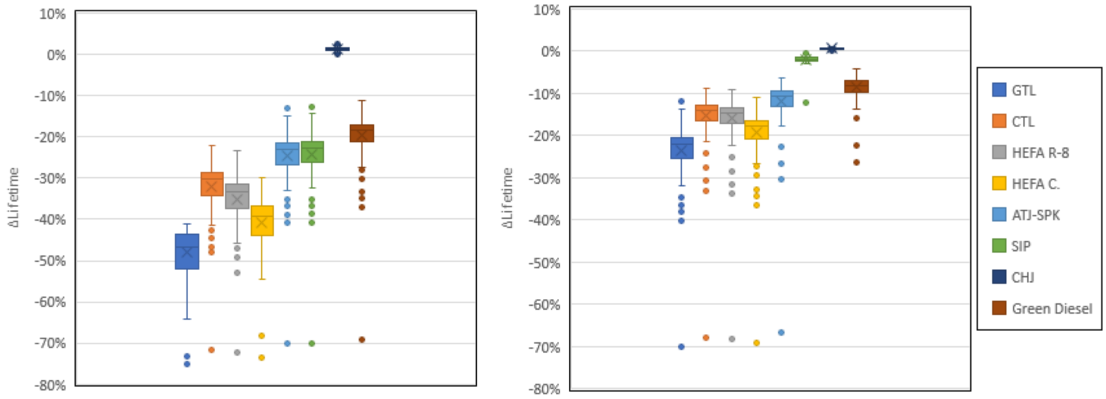

(a) Pure SAF.

(b) Blends.

Figure 5.10: RDs in lifetime for reference contrails with lifetimes of over 2 hours.

Figure 5.10 shows the RDs in lifetimes for reference contrails with lifetimes of over 2 hours, with the oldest contrails having lifetimes of a bit over 11 hours. This range represents the typical contrail cirrus lifetime, and, much like the previous range, shows a trend of sharper decreases for higher reference lifetimes.

Pure GTL showed the biggest decrease, with a MRD of −47.94 %, while Green Diesel showed the smallest, with a MRD of −19.42 %. The GTL blend had a MRD of −23.53 %, while the SIP blend had a MRD of −1.95 %.

The maximum decrease, the outliers at around −70 % for both pure SAF and blends, was found for a reference contrail with a lifetime of around 7 hours, resulting in an absolute difference of a bit over 5 hours for pure GTL. This did not correspond to the highest absolute difference, which was of 6 hours and 20 minutes for pure GTL and occurred for a reference contrail with a lifetime of 10 hours and 40 minutes.

5.3 Optical Depth and Radiative Forcing

The climatic impact of a contrail cirrus is controlled by the product of its width by its optical depth. While the optical depth of a contrail is highest for young contrails, this product increases with contrail age, typically reaching maximum values a few hours into a contrail's lifetime. This makes contrail cirrus, which have much higher lifetimes, responsible for the largest climatic impacts [4].

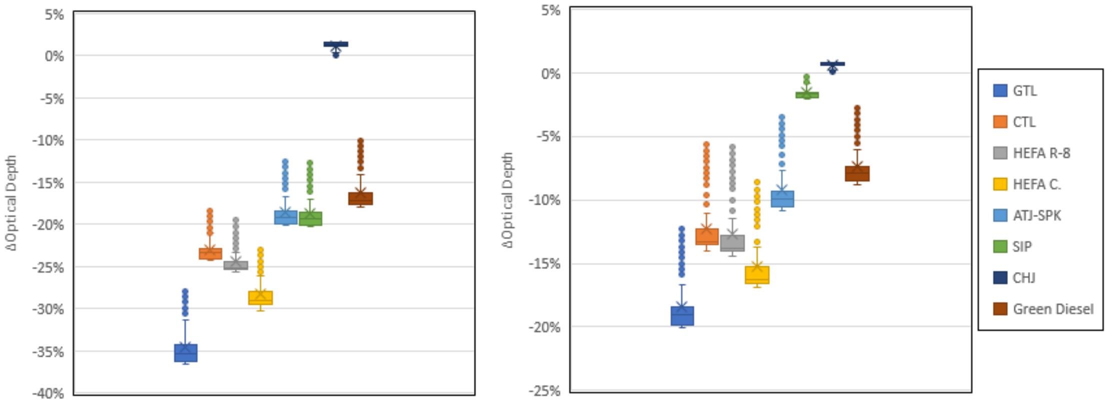

(a) Optical depth for pure SAF.

(b) Optical depth for blends.

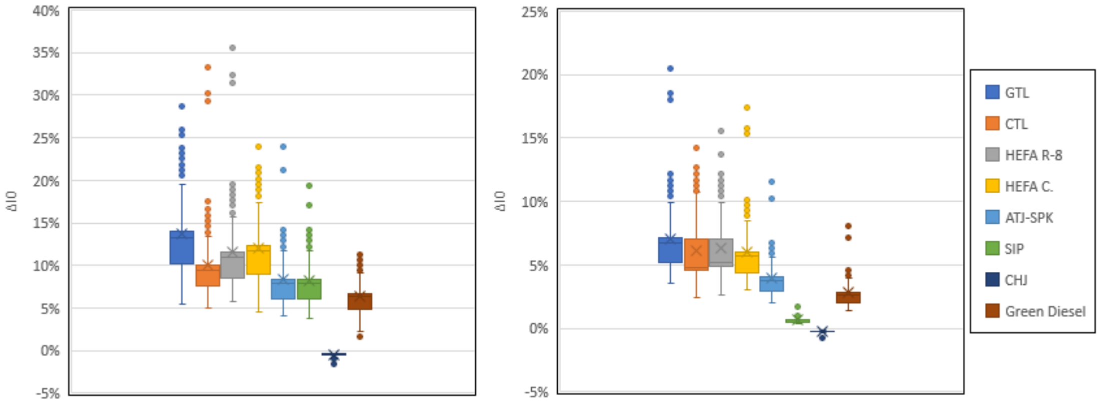

(c) Ice mass ratio for pure SAF.

(d) Ice mass ratio for blends.

Figure 5.11: RDs in peak optical depths and initial ice mass ratios for ambient relative humidities at formation of 43 % or higher.

The optical depths immediately after the wake vortex are analysed first. These are the peak optical depths values for these contrails, found at typical lifetimes of less than a minute. Figure 5.11 shows the bulk of results; these were optical depths for contrails formed in environments with a relative humidity of 43 % or higher.

The optical depths found in this range had typical values of 0.1 - 0.5, and the RDs between fuels seemed to be mostly influenced by the particle emissions. Higher RDs were found for pure SAF, with pure GTL showing a MRD of −34.49 % and the GTL 50:50 blend showing a MRD of −18.45 %. As was the case for lifetimes, SIP gives the smallest RDs when burnt in a blend due to its low ratio, going from a MRD of −18.60 % when burnt pure to a MRD of −1.57 % when burnt in a 10 % blend.

The results showed a relatively small deviation, with IQRs of 2 % or less for the RDs. Still, there was a trend of a reduction in formation ambient relative humidity leading to smaller RDs, typically associated to lower reference contrail optical depths.

The outliers plotted all correspond to contrails formed at relative humidities lower than 50 %. Contrails formed at these relative humidities tended to have higher initial ice mass fractions, typically in the order of 10^{-5}, with smaller RDs between fuels. These can be seen in figures 5.11c and 5.11d. While the MRDs of the fuels tend to follow the trends set by water vapour emissions, a large dispersion can be seen, with outliers that do not always respect it.

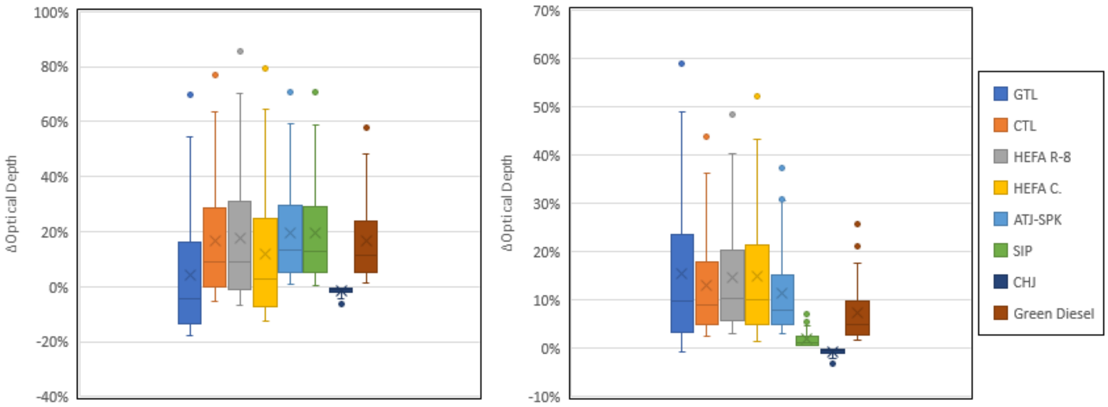

(a) Optical depth for pure SAF.

(b) Optical depth for blends.

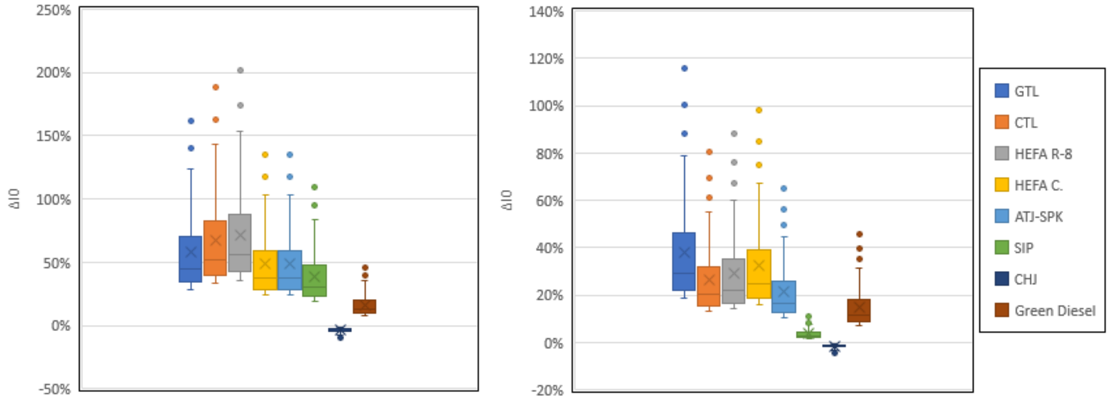

(c) Ice mass ratio for pure SAF.

(d) Ice mass ratio for blends.

Figure 5.12: RDs in peak optical depths and initial ice mass ratios for ambient relative humidities at formation in the range of 41 % to 43 %.

Figure 5.12 shows the RDs for contrails formed at relative humidities of 41 % to 43 %. Contrails formed in these conditions had peak optical depths in the range of 0.02 - 0.1. Optical depths in this range are not visible in satellite observations and should have limited climatic impact.

The different SAF started yielding positive RDs for different relative humidities; GTL at a relative humidity of ∼42 %, HEFA C. at ∼42.5 %, CTL and HEFA R-8 ∼42.7 % and the other fuels[3] at around ∼43 %. In the case of blends, all led to increases starting at a relative humidity of around 43 %.

Initial ice mass ratios for this range were typically of the order of 10^{-6}, and their influence in the optical depth is much clearer here than in the previous range. Peak RDs in optical depth can be seen to directly correspond to peak RDs in ice mass ratios. The highest MRD in optical depth was found for pure HEFA R-8, corresponding to the highest MRD in initial ice mass ratio too.

---

[3] This includes CHJ, which started yielding negative RDs instead of positive RDs.

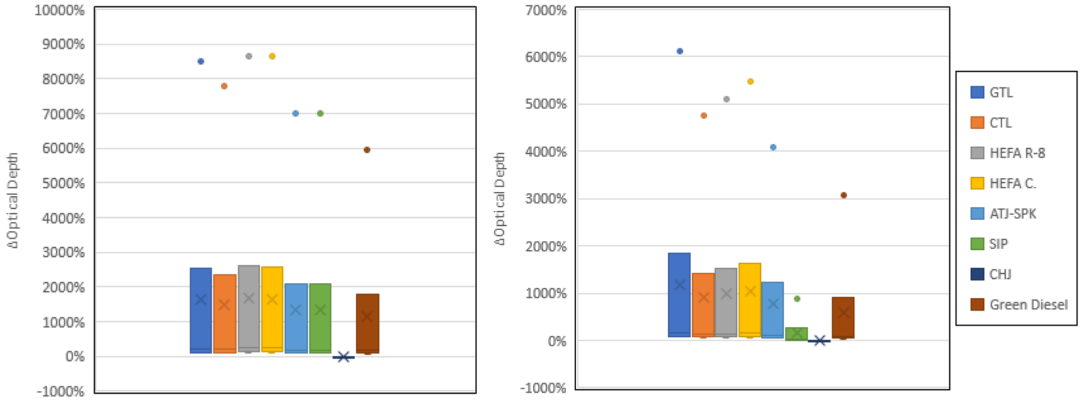

(a) Optical depth for pure SAF.

(b) Optical depth for blends.

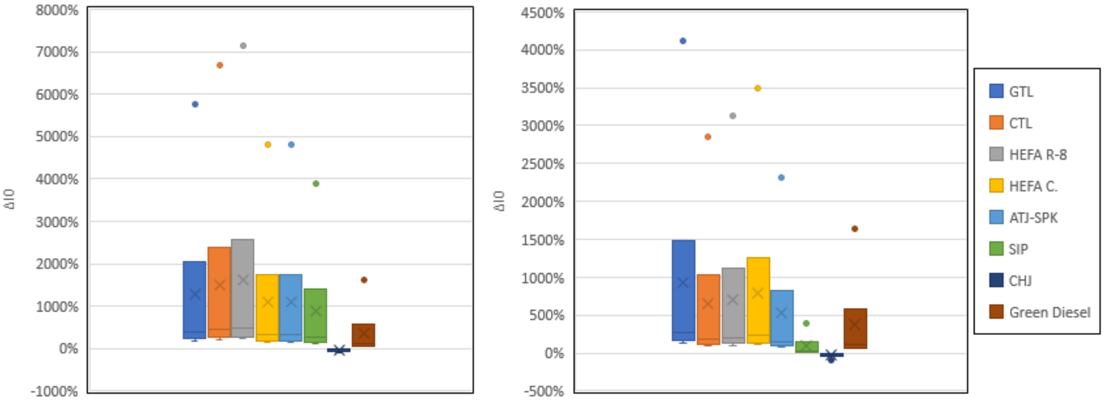

(c) Ice mass ratio for pure SAF.

(d) Ice mass ratio for blends.

Figure 5.13: RDs in peak optical depths and initial ice mass ratios for ambient relative humidities at formation in the range of 40 % to 41 %.

Contrails formed at relative humidities of 40 % or less fully lost their ice content during the wake vortex phase, and so optical depths for them were not calculated. A few contrails were formed or the relative humidity range of 40 % to 41 %. Jet A-1 contrails formed in this range had optical depths of 0.0003 - 0.02, while SAF optical depths reached peak values of ∼0.04.

There were very few reference contrails formed under these conditions, and all had initial ice mass ratios in the order of 10^{-8} - 10^{-7}. It is quite clear that the initial mass ratios control the differences in optical depth in this range.

As stated previously, the RF of contrails is controlled by the product of contrail width by optical depth. This value tends to reach its peak not for young contrails, but for contrail cirrus with a few hours of age.

The influence of the different fuels on this product is analysed for the peak value for each contrail, which for contrails with long lifetimes may mean that values with a few hours of difference are being compared. The values analysed here are thus not only influenced by the optical depth of the contrail, but also by the contrail's lifetime.

Figure 5.14 shows the RDs in the product of the contrail width by optical depth for a relative humidity range of 43 % to 58 % at formation; this is the range containing the bulk of the results. While the IQR for these plots is very small, ∼1 %, there are a high amount of outliers for pure SAF. This is due to the influence of the contrail lifetimes; while most contrails formed in these conditions have similar lifetimes, some contrails settle into more humid locations and end up living far longer.

As previously seen, long lasting contrail-cirrus experience much bigger decreases in lifetime than younger contrails (pure GTL had a MRD of −47.94 % for reference contrails aged 2 hours or more and a MRD of −8.02 % for contrails aged under two hours), which leads to SAF peaks being reached much later in relation to Jet A-1 contrails, enhancing this way the differences.

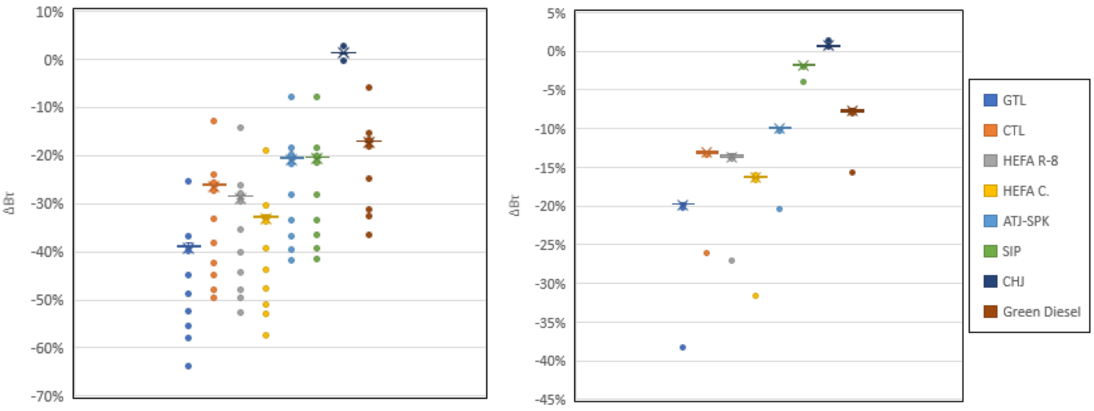

(a) Pure SAF.

(b) Blends.

Figure 5.14: RDs in the product of contrail width by contrail optical depth for ambient relative humidities at formation of 43 % to 58 %.

Contrails formed at an ambient relative humidity of 58 % or more all led to long-lasting contrail cirrus. The RDs for the product of width by optical depth is shown in figure 5.15 separately from the previous range to illustrate their low dispersion.

This range contains contrails with big RDs in peak optical depth value, and absolute differences in lifetime of a few hours. The effect of the contrail age on this product is most clearly felt here. Since the product of contrail width by optical depth is the factor which controls a contrail’s RF, the biggest impact on the climatic influence of contrails when using SAF should be felt for contrail cirrus and not young contrails.

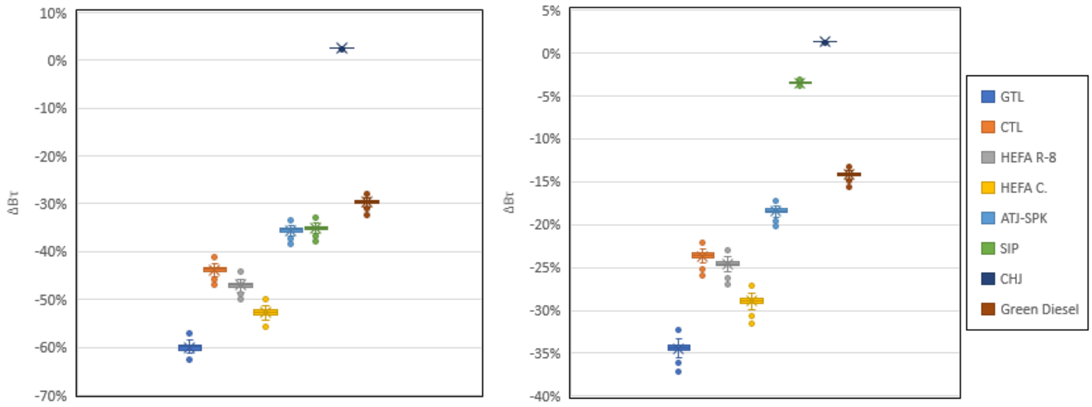

(a) Pure SAF.

(b) Blends.

Figure 5.15: RDs in the product of contrail width by contrail optical depth for ambient relative humidities at formation of 58 % or higher.

Figure 5.16 shows the RDs for the contrails formed at a relative humidity of 40 % to 43 %. Below a relative humidity of 40 %, as stated before, all contrails dispersed during the wake vortex phase and thus no calculations are presented.

Contrails formed in this range had peaks at less than one minute of age. Due to this, the peak optical depth and the optical depth at the peak of the product of contrail width by optical depth were very close to each other. Adding to this, the biggest influence on the width of a contrail at these times is the size of the aircraft, which makes the widths between the different fuels also quite similar. This led to a RD trend which was mostly controlled by the peak optical depths.

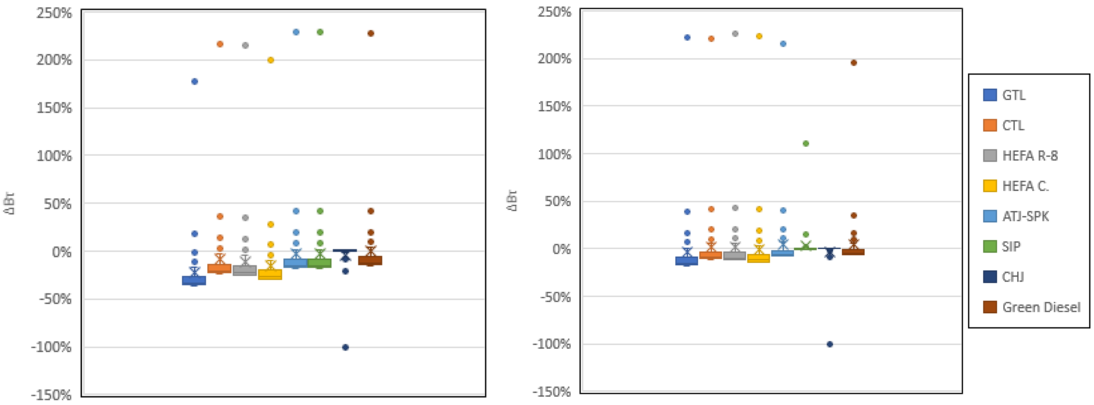

(a) Pure SAF.

(b) Blends.

Figure 5.16: RDs in the product of contrail width by contrail optical depth for ambient relative humidities at formation of 40 % to 43 %

Chapter 6

Conclusions and Future Work

6.1 Conclusions

A contrail-prediction model was implemented with the goal of analysing the effects on contrail properties of burning typical SAF instead of Jet A-1. The contrail model validation showed good agreement, but the auxiliary soot model showed a lacking response to engine power variations, likely as a result of the model not accounting for particle radius variation.

It was found that differences in water vapour emissions between the fuels lead to an increase in contrail formation frequency when very close to reference threshold conditions. Since contrails for SAF form within 1°C of contrails for Jet A-1, this was translated into longer contrails for SAF and not into isolated SAF contrail segments.

Contrail cirrus had decreases in lifetime when using SAF of up 76 %, with peak MRDs found for pure GTL at −47.94 %. RDs for the lifetime showed a large dispersion, attributed to the heavy dependence this parameter has on local ambient conditions. Nevertheless, a trend of steeper decrease being associated with older Jet A-1 contrails could be seen.

Short-lived contrails had even larger dispersions, with RDs of 800 % found within seconds of RDs of 0 %. Overall they showed slight increases in lifetime, but there were ambient-condition dependent outliers which yielded much larger RDs. While older contrails seem to be influenced more heavily by particle emissions, short-lived contrails seem to be influenced mostly by water vapour emissions.

Peak optical depths were found to be smaller for SAF in most cases, with exceptions being found for contrails formed at a relative humidity range of 40 % to 42 %. Jet A-1 contrails formed in these conditions had peak optical depths with orders of 10^{-4} to 10^{-2}, mostly due to the very low ice water content of the contrails.

The climatic impact of the contrails was measured with the product of contrail width by optical depth, which is the factor which is deemed to control their RF. As was expected, the climatic impact of contrail cirrus was found in this work to be much heavier than that of younger contrails.

The product of contrail width by optical depth showed steep decreases for contrail-cirrus formed by SAF, both due to the much smaller lifetimes, and due the big decrease in initial optical depth for these. Younger contrails showed smaller decreases, with contrails formed at a relative humidity of 42 % or lower showing instead an increase in the value of this factor.

Routes in dry locations yielded very short-lived contrails which did not survive past the wake vortex phase. SAF did not influence contrails in this situation, but a more complex large-eddy simulation model could yield different results for this phase. Nevertheless, since the climatic impact of contrails comes largely from them surviving long past the wake vortex phase, the relative importance of any differences found in this phase should be lower.

Routes in more humid locations, such as Europe and North America, yielded contrails with typically longer lifetimes, which were heavily influenced by the use of SAF. The adoption of SAF and SAF blends in these areas could significantly reduce the climatic impact of both persistent contrails and contrail cirrus.

6.2 Future Work

Future work should focus on improvements to the soot emission predictions. Ideally, a database of SAF surrogates should be created for this purpose. These could then be used together with models such as those found in reference [62] for CHEMKIN to predict the formation of acetylene in the Leung *et al.* model [53], or, alternatively, to obtain a more detailed correlation for the formation of acetylene. The latter option would make it easier to add new fuels as they became relevant, and would be less computationally expensive.

Another alternative would be to collect further data on particle size variation with engine power and fuel to aid in the creation of a particle radius model. If the particle radius model in conjunction with the Rizk and Mongia model showed good agreement, it could be more suitable for this implementation, since while the engine model and the contrail model are not excessively heavy individually, they have to be called at each route point which largely increases the overall run time of the simulations. A heavier kinetics-based soot model, which would also need to be called at every route point, could further increase this run time and make the program difficult to use.

Bibliography

[1] R. M. P. Gaspar and J. M. M. Sousa, “Impact of alternative fuels on the operational and environmental performance of a small turbofan engine,” *Energy Conversion and Management*, vol. 130, pp. 81–90, 2016. [Cited on pages 7, 45, 47, 50, and 51]

[2] C. Moses, “U.S. Army Alternative Gas-Turbine Fuels Research: MERADCOM (Mobility Equipment Research and Development Command),” *Southwest Research Institute*, p. 10, 01 1984. [Cited on pages 7 and 39]

[3] R. H. Moore, K. L. Thornhill, B. Weinzierl, D. Sauer, E. D’Ascoli, J. Kim, M. Lichtenstern, M. Scheibe, B. Beaton, A. J. Beyersdorf, J. Barrick, D. Bulzan, C. A. Corr, E. Crosbie, T. Jurkat, R. Martin, D. Riddick, M. Shook, G. Slover, C. Voigt, R. White, E. Winstead, R. Yasky, L. D. Ziemba, A. Brown, H. Schlager, and B. E. Anderson, “Biofuel blending reduces particle emissions from aircraft engines at cruise conditions,” *Nature*, vol. 543, no. 7645, pp. 411–415, 2017. [Cited on pages 7, 10, 11, 13, 39, and 42]

[4] U. Schumann, “A contrail cirrus prediction model,” *Geoscientific Model Development*, vol. 5, no. 3, pp. 543–580, 2012. [Cited on pages 7, 8, 22, 23, 24, 25, 26, 27, and 60]

[5] U. Schumann, “On conditions for contrail formation from aircraft exhausts,” *Meteorologische Zeitschrift*, vol. 5, pp. 4–23, 03 1996. [Cited on pages 7, 9, 12, 19, 20, and 21]

[6] U. Burkhardt and B. Kärcher, “Global radiative forcing from contrail cirrus,” *Nature Climate Change*, vol. 1, no. 1, pp. 54–58, 2011. [Cited on pages 8, 10, and 12]

[7] K. Gierens, P. Spichtinger, and U. Schumann, *Ice Supersaturation*, pp. 135–150. Berlin, Heidelberg: Springer Berlin Heidelberg, 2012. [Cited on pages 8 and 9]

[8] U. Schumann, *Research Topics in Aerospace*. Springer, 2002. [Cited on pages 9, 10, 12, 19, 23, and 24]

[9] L. Bock and U. Burkhardt, “Contrail cirrus radiative forcing for future air traffic,” *Atmospheric Chemistry and Physics*, vol. 19, pp. 8163–8174, 06 2019. [Cited on pages 10, 11, and 12]

[10] F. Yin, G. Volker, C. Frömming, and H. Yamashita, “Impact on flight trajectory characteristics when avoiding the formation of persistent contrails for transatlantic flights,” *Transportation Research Part D Transport and Environment*, vol. 65, 09 2018. [Cited on page 11]

[11] J. T. Wilkerson, M. Z. Jacobson, A. Malwitz, S. Balasubramanian, R. Wayson, G. Fleming, A. D. Naiman, and S. K. Lele, “Analysis of emission data from global commercial aviation: 2004 and 2006,” *Atmospheric Chemistry and Physics*, vol. 10, no. 13, pp. 6391–6408, 2010. [Cited on page 11]

[12] IATA Economics, “Economic Per formance of the Airline Industry Key Points,” *IATA 2020 Economic Report*, pp. 1–6, 2020. [Cited on page 11]

[13] Air Transport Action Group, “Waypoint 2050: An Air Transport Action Group Project,” 2020. [Cited on pages 11 and 16]

[14] A. Bhattacharya, “Competing priorities,” *Chemistry World*, vol. 5, no. 11, p. 2, 2008. [Cited on page 11]

[15] U. Schumann, “Influence of propulsion efficiency on contrail formation,” *Aerospace Science and Technology*, vol. 4, pp. 391–402, 2000. [Cited on pages 11, 12, 19, and 21]

[16] F. Yin, V. Grewe, C. Frömming, and H. Yamashita, “Impact on flight trajectory characteristics when avoiding the formation ofmulti-model mean persistent contrails for transatlantic flights,” *Transportation Research Part D: Transport and Environment*, vol. 65, pp. 466–484, 2018. [Cited on page 12]

[17] O. Deuber, M. Sigrun, S. Robert, P. Michael, and L. Ling, “A physical metric-based framework for evaluating the climate trade-off between CO2 and contrails-The case of lowering aircraft flight trajectories,” *Environmental Science and Policy*, vol. 25, pp. 176–185, 2013. [Cited on page 12]

[18] C. Newinger and U. Burkhardt, “Sensitivity of contrail cirrus radiative forcing to air traffic scheduling,” *Journal of Geophysical Research Atmospheres*, vol. 117, no. 10, pp. 1–12, 2012. [Cited on page 12]

[19] F. Noppel and R. Singh, “Overview on contrail and cirrus cloud avoidance technology,” *Journal of Aircraft*, vol. 44, no. 5, pp. 1721–1726, 2007. [Cited on page 12]

[20] S. Parkash, *Refining processes 2002*, vol. 81. 2002. [Cited on page 13]

[21] T. Rindlisbacher and S. D. Jacob, “Icao environmental report 2016,” pp. 85–88, 2016. [Cited on page 13]

[22] H. Omidvarborna, A. Kumar, and D. S. Kim, “Recent studies on soot modeling for diesel combustion,” *Renewable and Sustainable Energy Reviews*, vol. 48, pp. 635–647, 2015. [Cited on pages 13, 14, and 15]

[23] B. S. Haynes and H. G. Wagner, “Soot formation,” *Progress in Energy and Combustion Science*, vol. 7, no. 4, pp. 229–273, 1981. [Cited on page 13]

[24] H. R. Jonsdottir, M. Delaval, Z. Leni, A. Keller, B. T. Brem, F. Siegerist, D. Schönenberger, L. Durdina, M. Elser, H. Burtscher, A. Liati, and M. Geiser, “Non-volatile particle emissions from aircraft turbine engines at ground-idle induce oxidative stress in bronchial cells,” *Communications Biology*, vol. 2, no. 1, pp. 1–11, 2019. [Cited on page 13]

[25] D. S. Lee, “The current state of scientific understanding of the non-CO_2 effects of aviation on climate,” *Manchester Metropolitan University,*, pp. 1–16, 2018. [Cited on page 13]

[26] B. Kärcher and F. Yu, “Role of aircraft soot emissions in contrail formation,” *Geophysical Research Letters*, vol. 36, no. 1, pp. 1–5, 2009. [Cited on pages 13 and 14]

[27] B. Kärcher, “Formation and radiative forcing of contrail cirrus,” *Nature Communications*, vol. 9, no. 1, pp. 1–17, 2018. [Cited on page 13]

[28] I. M. Kennedy, “Models of soot formation and oxidation,” *Progress in Energy and Combustion Science*, vol. 23, no. 2, pp. 95–132, 1997. [Cited on page 14]

[29] H. A. Michelsen, M. B. Colket, P. E. Bengtsson, A. D’Anna, P. Desgroux, B. S. Haynes, J. H. Miller, G. J. Nathan, H. Pitsch, and H. Wang, “A review of terminology used to describe soot formation and evolution under combustion and pyrolytic conditions,” *ACS Nano*, vol. 14, no. 10, pp. 12470–12490, 2020. [Cited on pages 14 and 15]

[30] A. H. Lefebvre, *Gas Turbine Combustion: Alternative Fuels and Emissions*. CRC Press, 2010. [Cited on pages 15, 17, 44, 50, and 51]

[31] "2021 aviation industry outlook." `https://blog.satair.com/2021-aviation-industry-outlook`. Accessed: 18.05.2021. [Cited on page 16]

[32] "Aviation industry outlook for 2020." `https://blog.satair.com/aviation-industry-outlook-for-2020`. Accessed: 18.05.2021. [Cited on page 16]

[33] "Eurocontrol five-year forecast 2020-2024." `https://www.eurocontrol.int/publication/eurocontrol-five-year-forecast-2020-2024`. Accessed: 18.05.2021. [Cited on page 16]

[34] P. Nagle, "The oil market outlook: a speedy recovery." `https://blogs.worldbank.org/opendata/oil-market-outlook-speedy-recovery`. Accessed: 18.05.2021. [Cited on page 17]

[35] IATA, "Fact Sheet: What is SAF?," pp. 1–3, 2019. [Cited on pages 17 and 18]

[36] A. Oldani, "Surrogate Modeling of Alternative Jet Fuels," 2014. [Cited on pages 17 and 38]

[37] K. Hamilton, "Electric aviation could be closer than you think." `https://www.scientificamerican.com/article/electric-aviation-could-be-closer-than-you-think`. Accessed: 18.05.2021. [Cited on page 17]

[38] C. Henderson, "The hydrogen revolution in the skies." `https://www.bbc.com/future/article/20210401-the-worlds-first-commercial-hydrogen-plane`. Accessed: 18.05.2021. [Cited on page 17]

[39] K. Button, "Curbing contrails." `https://aerospaceamerica.aiaa.org/features/curbing-contrails`. Accessed: 18.05.2021. [Cited on page 17]

[40] W. J. Bräunling, *Flugzeugtriebwerke Grundlagen, Aero-Thermodynamik, ideale und reale Kreisprozesse, Thermische Turbomaschinen, Komponenten, Emissionen und Systeme*. Springer Vieweg, 2015. [Cited on page 19]

[41] M. Ponater, S. Marquart, and R. Sausen, "Contrails in a comprehensive global climate model: Parameterization and radiative forcing results," *Journal of Geophysical Research*, vol. 107, 2002. [Cited on page 22]

[42] U. Schumann, "Formation, properties and climatic effects of contrails," *Comptes Rendus Physique*, vol. 6, no. 4, pp. 549 – 565, 2005. [Cited on page 22]

[43] F. Holzäpfel, "Probabilistic two-phase wake vortex decay and transport model," *Journal of Aircraft*, vol. 40, no. 2, pp. 323–331, 2003. [Cited on page 23]

[44] F. Holzäpfel, "Probabilistic two-phase aircraft wake-vortex model: Further development and assessment," *Journal of Aircraft*, vol. 43, no. 3, pp. 700–708, 2006. [Cited on page 23]

[45] R. Huang, H. Sun, C. Wu, C. Wang, and B. Lu, "Estimating eddy dissipation rate with QAR flight big data," *Applied Sciences (Switzerland)*, vol. 9, no. 23, pp. 1–14, 2019. [Cited on page 23]

[46] U. Schumann, P. Jeßberger, and C. Voigt, "Contrail ice particles in aircraft wakes and their climatic importance," *Geophysical Research Letters*, vol. 40, no. 11, pp. 2867–2872, 2013. [Cited on page 25]

[47] C. Schiller, M. Krämer, A. Afchine, N. Spelten, and N. Sitnikov, "Ice water content of Arctic, midlatitude, and tropical cirrus," *Journal of Geophysical Research Atmospheres*, vol. 113, no. 24, pp. 1–12, 2008. [Cited on page 26]

[48] Z. Kapadia, D. Spracklen, S. Arnold, D. Borman, G. Mann, K. Pringle, S. Monks, C. Reddington, F. Benduhn, A. Rap, C. Scott, E. Butt, and M. Yoshioka, “Impacts of aviation fuel sulfur content on climate and human health,” *Atmos. Chem. Phys. Discuss.*, vol. 15, pp. 18921–18961, 2015. [Cited on page 27]

[49] P. Konopka and J. Schröter, “Analytical Gaussian Solutions for Anisotropic Diffusion in a Linear Shear Flow,” *Journal of Non-Equilibrium Thermodynamics*, vol. 20, no. 1, pp. 78–91, 1995. [Cited on page 29]

[50] I. Sölch and B. Kärcher, “A large-eddy model for cirrus clouds with explicit aerosol and ice microphysics and Lagrangian ice particle tracking,” *Quarterly Journal of the Royal Meteorological Society*, vol. 136, no. 653, pp. 2074–2093, 2010. [Cited on page 32]

[51] J. Um, G. M. McFarquhar, Y. P. Hong, S. S. Lee, C. H. Jung, R. P. Lawson, and Q. Mo, “Dimensions and aspect ratios of natural ice crystals,” *Atmospheric Chemistry and Physics*, vol. 15, no. 7, pp. 3933–3956, 2015. [Cited on page 32]

[52] N. K. Rizk and H. C. Mongia, “Emissions predictions of different gas turbine combustors,” *AIAA 94-0118*, 1994. [Cited on pages 35, 39, 40, 41, and 42]

[53] K. M. Leung, R. P. Lindstedt, and W. P. Jones, “A simplified reaction mechanism for soot formation in nonpremixed flames,” *Combustion and Flame*, vol. 87, no. 3-4, pp. 289–305, 1991. [Cited on pages 35, 36, 38, and 66]

[54] F. Tao, R. D. Reitz, D. E. Foster, and Y. Liu, “Nine-step phenomenological diesel soot model validated over a wide range of engine conditions,” *International Journal of Thermal Sciences*, vol. 48, no. 6, pp. 1223–1234, 2009. [Cited on pages 36 and 38]

[55] F. Tao, V. I. Golovitchev, and J. Chomiak, “A phenomenological model for the prediction of soot formation in diesel spray combustion,” *Combustion and Flame*, vol. 136, no. 3, pp. 270–282, 2004. [Cited on page 36]

[56] F. Liu, H. Guo, G. J. Smallwood, and Ö. L. Gülder, “Numerical modelling of soot formation and oxidation in laminar coflow non-smoking and smoking ethylene diffusion flames,” *Combustion Theory and Modelling*, vol. 7, no. 2, pp. 301–315, 2003. [Cited on page 36]

[57] Y. Zhang, H. Zhou, M. Xie, Q. Fang, and Y. Wei, “Modeling of soot formation in gas burner using reduced chemical kinetics coupled with CFD code,” *Chinese Journal of Chemical Engineering*, vol. 18, no. 6, pp. 967–978, 2010. [Cited on page 36]

[58] K. G. Neoh, J. B. Howard, and A. F. Sarofim, “Effect of oxidation on the physical structure of soot,” *Symposium (International) on Combustion*, vol. 20, no. 1, pp. 951–957, 1985. [Cited on page 36]

[59] S. Manzello, G. Mulholland, M. Donovan, W. Tsang, M. Zachariah, and S. Stouffer, “On the use of a well stirred reactor to study soot inception,” 2005. [Cited on page 36]

[60] S. R. Turns, *An Introduction to Combustion Concepts and Applications*. McGraw-Hill Education, 2011. [Cited on pages 36 and 37]

[61] T. Haug-warberg, “Plug Flow Reactor Part III . Modelling Issues,” 2011. [Cited on page 38]

[62] “Detailed kinetic mechanisms.” `http://creckmodeling.chem.polimi.it/menu-kinetics/menu-kinetics-detailed-mechanisms`. Accessed: 18.04.2021. [Cited on pages 38 and 66]

[63] A. Fusco, A. Knox-Kelecy, and D. Foster, “Application of a Phenomenological Soot Model to Diesel Engine Combustion,” *International Symposium COMODIA 94*, 1994. [Cited on pages 38 and 39]

[64] S. P. Zeppieri, S. D. Klotz, and F. L. Dryer, “Modeling concepts for larger carbon number alkanes: A partially reduced skeletal mechanism for n-decane oxidation and pyrolysis,” *Proceedings of the Combustion Institute*, vol. 28, no. 2, pp. 1587–1595, 2000. [Cited on page 39]

[65] J. Nagle and R. F. Strickland-Constable, “Oxidation of carbon between 1000-2000℃,” 1962. [Cited on pages 39 and 40]

[66] R. R. Kumal, J. Liu, A. Gharpure, R. L. Vander Wal, J. S. Kinsey, B. Giannelli, J. Stevens, C. Leggett, R. Howard, M. Forde, A. Zelenyuk, K. Suski, G. Payne, J. Manin, W. Bachalo, R. Frazee, T. B. Onasch, A. Freedman, D. B. Kittelson, and J. J. Swanson, “Impact of Biofuel Blends on Black Carbon Emissions from a Gas Turbine Engine,” *Energy and Fuels*, vol. 34, no. 4, pp. 4958–4966, 2020. [Cited on page 40]

[67] ICAO, *ICAO, Volume 2, Appendix 7: Environmental Technical Manual, Procedures for the Emissions Certification of Aircraft Engines*, vol. II. 2014. [Cited on page 41]

[68] U. E. P. Agency, *Determination of Effects of Ambient Conditions on Aircraft Emissions*. 1977. [Cited on page 41]

[69] S. C. A. Kluiters, W. P. J. Visser, and E. R. Rademaker, “A new combustor and emission model for the gas turbine simulation program GSP,” 2014. [Cited on pages 41 and 42]

[70] J. S. Chin and A. H. Lefebvre, “Steady State Evaporation Characteristics of Hydrocarbon Fuel Drops.,” *AIAA Paper*, vol. 21, no. 10, pp. 1437–1443, 1982. [Cited on pages 44 and 45]

[71] J. H. Sawyer, “Sawyer’s Gas Turbine Engineering Handbook,” *Business Journals*, 1976. [Cited on pages 50 and 51]

[72] H. Hersbach, C. Peubey, A. Simmons, P. Berrisford, P. Poli, and D. Dee, “ERA-20CM: A twentieth-century atmospheric model ensemble,” *Quarterly Journal of the Royal Meteorological Society*, vol. 141, no. 691, pp. 2350–2375, 2015. [Cited on page 51]

[73] “Real world flightplan database.” `https://www.edi-gla.co.uk/`. Accessed: 31.10.2020. [Cited on page 51]

[74] F. M. White, *Fluid Mechanics*. McGraw- Hill, 2011. [Cited on page 52]

[75] S. McLeod, “What does a box plot tell you?.” `https://www.simplypsychology.org/boxplots.html`. Accessed: 15.05.2021. [Cited on page 54]

Appendix A

Fuel Properties

Properties	Symbol	Jet A-1	GTL	CTL	HEFA R-8	HEFA C.	ATJ-SPK	SIP	CH	Green Diesel
Net Heat of Combustion, MJ/kg	Q	43.2	44.2	44.0	44.1	44.3	44.3	44.1	43.3	43.7
Density at 15ºC, kg/m^3	ρ_{15}	802	737	762	763	751	774	774	804	777
Viscosity at -20ºC, kg/m^3	υ	3.91	2.60	3.60	5.50	3.30	8.40	14.10	3.50	14.77
Surface Tension at 25ºC, mm^2/s	σ	27.4	23.8	25.2	25.8	24.8	26.2	26.7	27.5	27.0
Initial Boiling Point, ºC	$T_{b,i}$	151	146	149	156	151	179	237	150	190
10% Recovered, ºC	$T_{10\%}$	169	162	166	178	161	188	244	165	243
50% Recovered, ºC	$T_{20\%}$	199	169	180	218	182	206	245	200	275
90% Recovered, ºC	$T_{90\%}$	243	184	208	263	237	249	245	249	288
Final Boiling Point, ºC	$T_{b,f}$	262	198	228	274	259	273	258	268	306
Hydrogen Content, % weight	$H\%$	13.87	15.60	15.10	15.30	15.40	14.90	14.90	13.80	14.70
Hydrogen to Carbon Molar Ratio	h/c	1.919	2.203	2.119	2.153	2.169	2.087	2.087	1.908	2.054
Molecular Weight, kg/kmol	M	160.5	146	156	177	160	169.9	195.6	161	217.5
Critical Temperature, ºC	T_c	392.3	346.5	364.5	394.2	367.1	392.2	418.3	393.7	438.8
Critical Pressure, bar	P_c	21.88	20.95	21.27	17.8	19.79	19.09	16.21	21.91	14.42
Smoke Point, mm %	SP	23	40	40	40	50	33	42	24	27

Table A.1: Fuel Properties.

Appendix B

Coefficients for Specific Heat Equation

This section details how to obtain the coefficients used in equation 4.6 to calculate the specific heat, c_p, of a hot gas. It can be used to calculate the specific heat for air, for the fuel and for the combustion mixture of both.

The coefficients used to calculate the specific heat of a gas are obtained from the mass fraction, m_i, and the coefficients from table B.2,A_i to E_i, for each component. This is exemplified in equation B.1 for the coefficient A and is valid for all coefficients.

$$A_{gas} = \sum A_i m_i = A_{N_2} m_{N_2} + A_{O_2} m_{O_2} + A_{CO_2} m_{CO_2} + A_{H_2O} m_{H_2O} + A_{Ar} m_{Ar} \tag{B.1}$$

Typical dry air component mass fractions, shown in table B.1, are used for air and hot combustion gas computations. The neon mass fraction is neglected, with its value being added to that of CO_2.

Gas Component	N_2	O_2	CO_2	H_2O	Ar
Mass Fraction	0.7552	0.23142	0.0005	0	0.01288

Table B.1: Dry air component mass fractions.

The combustion of a generic hydrocarbon-based fuel can be represented through the chemical reaction B.2a, which can also be expressed with respect to the hydrogen to carbon ratio, $h/c = n/m$, as in equation B.2b.

$$C_m H_n + \left(n + \frac{m}{4}\right) O_2 \rightarrow nCO_2 + \frac{m}{2} H_2O \tag{B.2a}$$

$$CH_{h/c} + \left(1 + \frac{h/c}{4}\right) O_2 \rightarrow CO_2 + \frac{h/c}{2} H_2O \tag{B.2b}$$

The mass fractions of O_2, CO_2 and H_2O have contributions not only from the air, but also from the fuel. These contributions can be obtained from reaction B.2b:

$$m_{O_2,F} = -f\left(1 + \frac{h/c}{4}\right) \frac{M_{O_2}}{M_F} \tag{B.3a}$$

$$m_{CO_2,F} = f \frac{M_{CO_2}}{M_F} \tag{B.3b}$$

$$m_{H_2O,F} = f \frac{h/c}{2} \frac{M_{H_2O}}{M_F} \tag{B.3c}$$

The c_p can then be computed from the calculated coefficients:

$$c_{p,g} = A_g + B_g T + C_g T^2 + D_g T^3 + E_g T^4 \tag{B.4}$$

	N_2	O_2	CO_2	H_2O	Ar
Temperature range $300K \leq T \leq 1000K$					
A	1095.683776	966.332377	409.980361	1918.320326	520.33093
B, 10^{-3}	−395.714659	−653.939246	1960.657727	−795.86536	0
C, 10^{-6}	786.620984	2230.371977	−2027.88064	2629.863898	0
D, 10^{-9}	−289.942305	−2156.613686	1198.885557	−2119.776328	0
E, 10^{-12}	−29.612737	703.695224	−307.578806	656.915609	0
Temperature range $1000K \leq T \leq 2500K$					
A	847.247858	934.79316	833.700359	1232.613775	520.33093
B, 10^{-3}	474.182463	203.050627	603.094906	1399.203482	0
C, 10^{-6}	−185.698755	−58.168373	−245.187837	−393.916501	0
D, 10^{-9}	33.585821	11.040338	45.61995	54.417303	0
E, 10^{-12}	−2.282331	−0.869396	−3.163128	−2.860198	0

Table B.2: Coefficients for the calculation of the specific heat of hot gas.

Appendix C

Routes

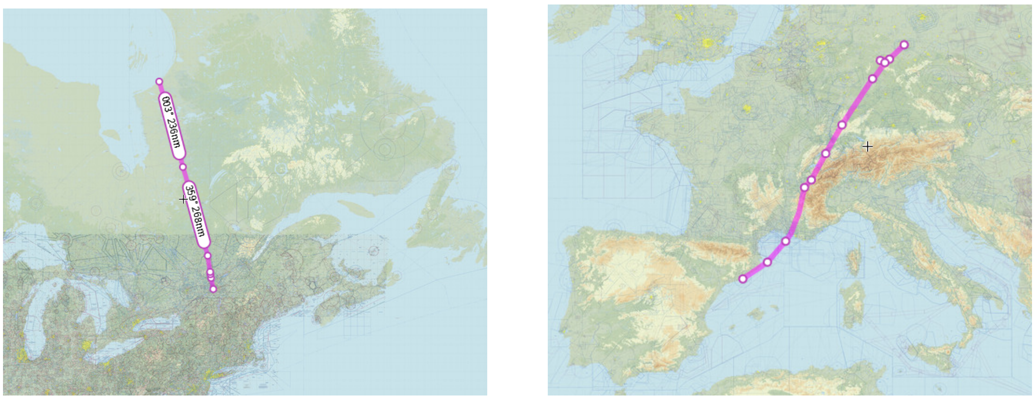
003° 236nm
359° 268nm

(a) CYUL to CYGW.

(b) EDDP to LEBL.

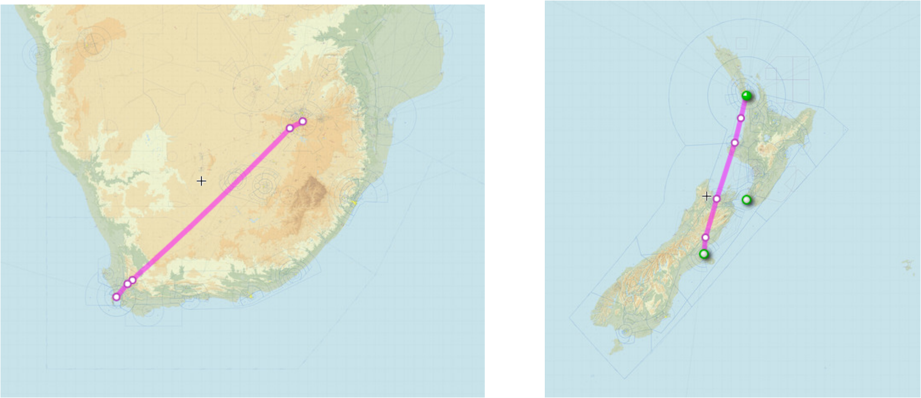

(c) FAOR to FACT.

(d) NZAA to NZCH.

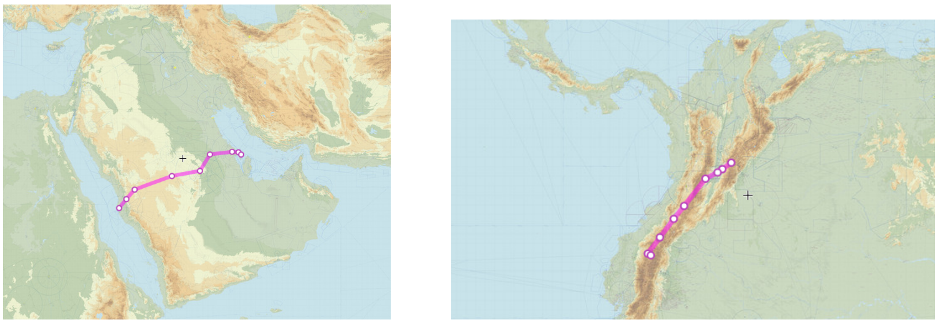

(e) OEJN to OBBI.

(f) SKBO to SEQM.

Figure C.1: Routes used in contrail simulations.

Appendix D

Properties of blends

The mass and mole fraction of the SAF in the blend can be obtained from equations D.1a D.1b, respectively. In these equations, κ is the blend ratio, the subscript i represents the chosen SAF and the subscript ref represents the reference fuel, Jet A-1.

$$m_i = \frac{\kappa \rho_{15,i}}{\kappa \rho_{15,i} + (1-\kappa)\rho_{15,ref}} \tag{D.1a}$$

$$n_i = \frac{m_i}{m_i + \frac{M_i}{M_{ref}}(1-m_i)} \tag{D.1b}$$

The net heat of combustion of the blend is computed from equation D.2.

$$Q_{blend} = m_i Q_i + m_{ref} Q_{ref} \tag{D.2}$$

The density of the blend at 15 °C is calculated from equation D.3.

$$\rho_{15,blend} = \left(\frac{m_i}{\rho_{15,i}} + \frac{m_{ref}}{\rho_{15,ref}}\right)^{-1} \tag{D.3}$$

The kinematic viscosity of the blend for –25 °C is calculated from the relation D.4. For $\upsilon \geq 1.5$ mm^2/s, c_T takes the value of 0, otherwise it follows from the relation $c_T = 0.0085(\upsilon - 1.5)^2$ mm^2/s.

$$loglog(\upsilon_{blend} + 0.7 + c_{T,blend}) = m_i loglog(\upsilon_i + .7 + c_{T,i}) + (1-m_i) loglog(\upsilon_{ref} + 0.7 + c_{T,ref}) \tag{D.4}$$

The surface tension is calculated from equation D.5.

$$\sigma_{blend} = \frac{\sigma_i \sigma_{ref}}{\sigma_i(1-m_i) + \sigma_{ref} m_i} \tag{D.5}$$

The normal boiling point of the blend is calculated using a graphical summation metho, as detailed in reference D.6. This is an empirical method applicable to blends with an initial boiling point higher than 85 °F and a final boiling point lower than 700 °F, and it is used here to calculate the temperatures for 10%, 50% and 90% of fuel volume recovered for the blend. The normal boiling point is then calculated from equation D.6.

$$T_{b,blend} = \frac{T_{10\%} + 2T_{50\%} + T_{90\%}}{4} \tag{D.6}$$

The hydrogen content and the hydrogen to carbon ratio of the blend are calculated from equations

D.7a and D.7b, while the molar mass of the blend is calculated from equation D.7c,

$$(H\%)_{blend} = \frac{100.79h/c}{12.011 + 1.0079h/c} \tag{D.7a}$$

$$(h/c)_{blend} = n_i(h/c)_i + (1 - n_i)(h/c)_{ref} \tag{D.7b}$$

$$M_{blend} = n_i M_i + (1 - n_i)M_{ref} \tag{D.7c}$$

The smoke point of the blend is obtained as in equation D.8:

$$SP_{blend} = n_i SP_i + (1 - n_i)SP_{ref} \tag{D.8}$$

The critical temperature and critical pressure of the blend are obtained from the relations D.9a and D.9b, respectively. $\rho_{60,r}$ represents the ratio of the fuel density at 60 °F and the water density at 60 °F.

$$T_{c,F} = 9.5233 T_{b,i}^{0.81067} \rho_{60,r}^{0.53691} e^{-9.314\times10^{-4} T_{b,i} - 0.544442\rho_{60,r} + 6.4791\times10^{-4}\rho_{60,r} T_{b,i}} \tag{D.9a}$$

$$P_{c,F} = 3.1958 \times 10^5 T_{b,i}^{-0.48440} \rho_{60,r}^{4.0846} e^{-8.505\times10^{-3} T_{b,i} - 4.8014\rho_{60,r} + 5.74\times10^{-3}\rho_{60,r} T_{b,i}} \tag{D.9b}$$